2017

Understanding the "Microwave" in Microwave Chemistry

Bridgett Alicia Ashley

FLORIDA STATE UNIVERSITY

COLLEGE OF ARTS AND SCIENCES

UNDERSTANDING THE “MICROWAVE” IN MICROWAVE CHEMISTRY

By

BRIDGETT ALICIA ASHLEY

A Dissertation submitted to the
Department of Chemistry and Biochemistry
in partial fulfillment of the
requirements for the degree of
Doctor of Philosophy

2017

Bridgett Alicia Ashley defended this dissertation on November 15, 2017.
The members of the supervisory committee were:

Geoffrey F. Strouse
Professor Directing Dissertation

Stephen Hill
University Representative

Albert E. Stiegman
Committee Member

Michael Shatruk
Committee Member

The Graduate School has verified and approved the above-named committee members, and certifies that the dissertation has been approved in accordance with university requirements.

Dedicated to my loving husband, Brad. Without your support, I'd never have been able to do this.

ACKNOWLEDGMENTS

The journey to getting my PhD would have never happened if I was not surrounded my so many awesome and supportive people. The people around me have encouraged me, challenged me, and help me to grow into the person I am today.

First of course, thank you Dr. Strouse for always pushing me to do my best, and then finally pushing me out of the door. You're a great chemist, and have helped me immensely in honing my own knowledge and skill.

I'd also like to thank Dr. Owens. You pushed me to come and finish my degree, and provided support, an ear, and excellent chemistry advice. Oxford commas forever!

I would also like to thank all of my committee members for taking the time to help me along my path, offering excellent advice and insight.

Additionally, I would also like to thank the following people:

- My family, who are the best ever! Without their support for my entire life, I wouldn't be here today.
- My group members for many excellent conversations about science, as well as pop culture and politics.
- The team at Tyndall AFB. Thank you so much for the support, and shoulders to cry on when things got crazy.
- Shelle, Kate, and Kerestin, for your upbeat attitudes, which always made my day better.
- Katherine, for being a great friend
- Bruce for many a great conversation, and advice
- Dr. Joe, for keeping my writing sane.
- Carnevale, for doing 5 billion TEM images for me, and Parth, for taking up the mantle after him.
- Chris, for doing 5 billion UV-Vis for me, I couldn't have done it without you.
- Matt and Tony, for being a great part of the team.

TABLE OF CONTENTS

LIST OF TABLES

LIST OF FIGURES

ABSTRACT

Microwave chemistry has long been a subject of interest in both the organic and inorganic synthesis communities. Microwave heating has the potential to become a powerful force for green synthesis in industry as it uses much less power to accomplish the same goals as traditional convective thermal reactions, but a lack of understanding of how to translate traditional convective reactions into microwave reactions is hampering this progress. In this dissertation an overview of microwave physics and mathematics is given first. Then the role of microwave source and choice of microwave reaction vessel, along with precursor and solvent choice in the design of a microwave chemical reaction is explored. Next, synthesis of nickel and gold nanoparticles — chosen because of their ubiquitous presence in the literature — in a microwave is explored, and the kinetics examined. Additionally, the role of size dependent properties of the nanoparticles, as well as the role of the oxide layer on the nanoparticle, are explored in relationship to how the reaction heats in a standard laboratory microwave. Lastly, the role of power and frequency of the microwave radiation in the synthesis of nickel nanoparticles is examined, and relationships between the kinetics of the synthesis and the applied power and frequency of the microwave are extracted.

CHAPTER 1

INTRODUCTION

1.1 General Introduction

In the mid 1940s Percy Spencer, a radar engineer at Raytheon, noticed the candy bar in his pocket had melted while he was working on an active radar set. Spencer then tried heating popcorn kernels and eggs in metal kettles beneath a magnetron. Raytheon patented the microwave oven in 1945, and by the 1960s affordable microwave ovens were available for home use. Chemists the world over were wondering just how microwave heating could improve their labs and science.

In today's highly populated, resource-limited world, the development of low-cost, energy efficient methods for synthesis of functional materials is an imperative. Microwave heating has been explored as a method of manufacturing materials and chemicals.[6] Given the need for localized, directed heating of materials, research into materials that heat efficiently under microwave irradiation is an area of rapid growth. The energy efficiency of conversion of microwave photons into heat has been theorized to lower energy consumption by 72%, as compared to traditional thermal reactions.[6,7,8,9,10] Early researchers noticed huge advantages, such as superheating of solvents, selective heating of dipolar or magnetic molecules, and the reduction of thermal gradients and wall effects. [11, 12] These "microwave effects" were originally attributed to unknown interactions with the microwave field such as possible selective bond cleaving.[11,12] It has since been clearly shown that microwave frequency-photons do not possess the energy necessary to cleave even the weakest of chemical bonds.[11, 12] The most commonly

accepted explanation of microwave advantages over traditional heating methods is that of "selective heating" (including the idea of selective heating influencing rapid nucleation).[11,13,14,15]

The absorption and reflection of microwave energy by molecules is applicable to designing microwave reactions and reaction vessels. Microwave reactors are increasingly common in chemistry laboratories across the world, allowing for rapid synthesis and prototyping of new procedures and materials. Generally, though, researchers use them in a black-box type manner, i.e. precursors in – product out, without ever considering that knowing more about how electromagnetic radiation interacts with molecules may help them optimize or even revolutionize their synthetic procedures. The focus of this dissertation is improving the understanding of how to design microwave reaction systems, from reaction vessel to choice of solvent and precursors to choice of microwave frequency. To this end, first an overview of microwave physical heating theory, measurement techniques, and microwave generation will be given. Then, the methods of characterization of the materials will be discussed, with emphasis on structural and optical techniques.

1.2 Microwave Interaction Theory

1.2.1 Basic Interactions and Frequency Dependency

To understand the interaction of a microwave photon with a material, the interaction must be described in terms of electromagnetic radiation. The ability of a material to store electrical charge is known as the permittivity, represented by ε'; and the combined losses (dipole, ionic, and Maxwell–Wagner) of a material are known as the loss factor, represented by ε''. Combined, these two values form the complex permittivity of a material—a value that is both frequency and temperature dependent.[3]

$$\varepsilon^* = \varepsilon' - i\varepsilon'' \quad [1.1]$$

The real component ε' is the *scattering term*, describing the ability of the material to store an electric charge. The *imaginary term* (ε'') describes the absorption of the impingent field, which is converted into heat in analogy to a classical absorption experiment in the visible frequency range. The absorption cross section is defined classically as the drop of EMR amplitude to a value of 1/*e*. In effect, the microwave is absorbed by the material with the largest ε″ and scattered by the material with the largest ε′ term in the system, and can be thought of as being similar to a Beer–Lambert law problem in absorption spectroscopy. Thus the ability of the system to interact with the microwave field is selective and will scale as the ratio

$$\tan\delta = \frac{\varepsilon''}{\varepsilon'} \quad [1.2]$$

Microwave heating can be classically described as follows: as an alternating EM field passes through a material, any polarizable molecules or particles can couple with the EM field. As the EM field shifts, the molecules experience lag time in realigning and the resulting molecular friction generates heat. Polarizable molecules can be either dipolar or ionic.[16] Additionally, if the material is a conductor or semiconductor, it can experience ohmic heating and charge separation. If the material is heterogeneous, heating can occur due the Maxwell–Wagner effect as well. This is caused by the buildup of charge at the interface between a conducting and a nonconducting material. [16] There are other losses—such as atomic and electronic—that are important at frequencies higher than are typically considered "microwave" (300 MHz to 300 GHz), and as such, are not significant players in the area we wish to explore.

Each material has unique electromagnetic absorption and scattering cross sections, and a solution or mixture can experience selective heating, in the case of a large difference in tan δ of the constituent parts. Selective heating is defined as the disproportionate heating of a molecule or

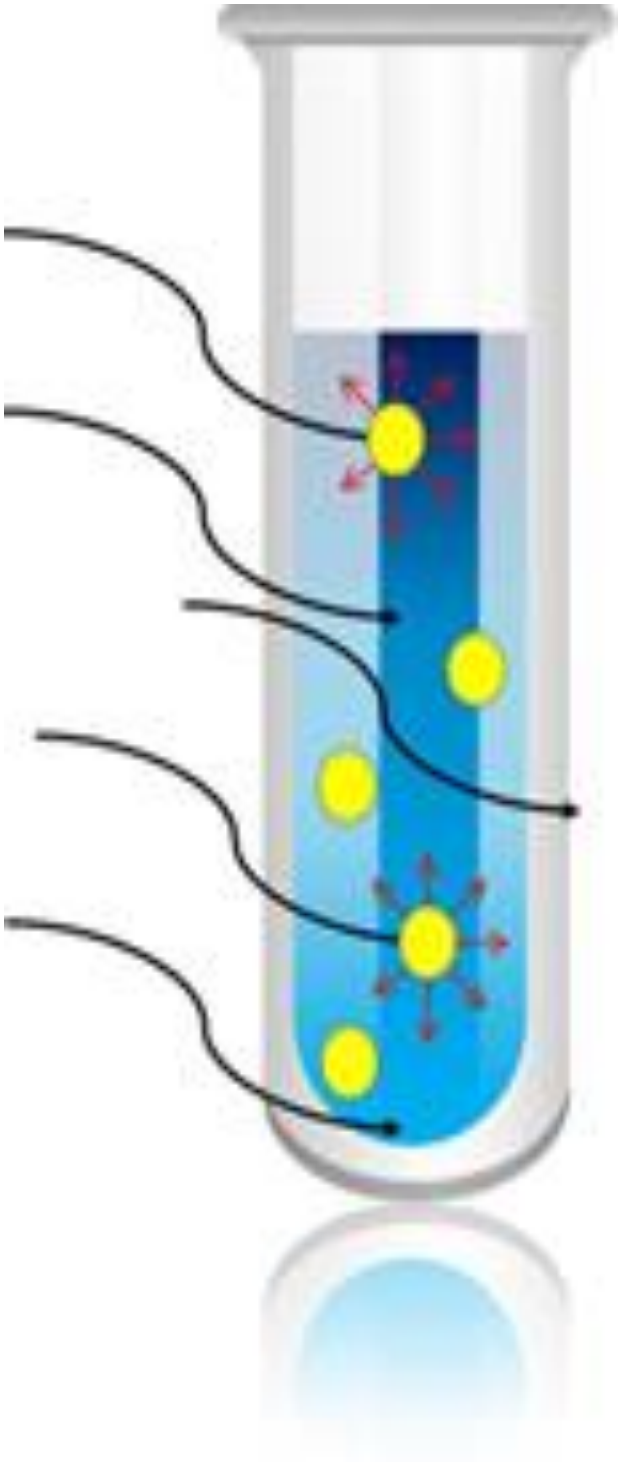

Figure 1.1: Illustration of photons being absorbed by the higher tan δ yellow molecules over the lower tan δ blue solvent, then releasing that energy as heat.

inclusion over another due to the molecule (or inclusion) having a greater tan δ. As molecules can only absorb the whole photon, not a part of a photon, there is a greater statistical probability that a molecule of higher tan δ will absorb a given photon. This can, theoretically, lead to localized areas of much higher temperature than the experimentally obtained bulk temperature. This effect is evidenced by increased reaction rates obtained at bulk temperatures lower than those required for similar reaction rates obtained using conventional heating (Figure 1.1).[11, 17] In the case of magnetic heating, μ' is the real permeability of the material. The sources of loss (μ'') in the magnet are domain walls and magnetic resonance.[16]

$$\mu^* = \mu' - i\mu" \qquad [1.3]$$

1.2.2 Size Dependency

As nanoparticles grow, their dielectric function and magnetic properties change rapidly, until the nanoparticle is big enough to be considered "bulk." This size depends on the material properties of the nanoparticle, such as Bohr radius, the amount of defects in the crystal structure, and the saturation magnetization, to name a few. To calculate the size dependency of the dielectric function for a semiconductor, we can use the energy gap change due to quantum confinement using Eqn 1.4

$$\varepsilon(D) = 1 + \left(\frac{\varepsilon_{\text{bulk}} - 1}{1 + \left({}^{\Delta E}/_{E_g} \right)^2} \right) \qquad [1.4]$$

Where $\varepsilon_{\text{bulk}}$ is the dielectric function of the bulk material, ΔE is the change in energy gap due to quantum confinement, and E_g is the bulk energy gap.[18]

The change in energy gap is calculated by modeling the nanoparticle as a particle in a box, using the reduced mass of the exciton (m_r) as seen in Eqn 1.5 (The Brus equation).[19]

$$\Delta E = E_g + \frac{h^2}{8r^2} m_r \qquad [1.5]$$

In the Brus equation, h is Plank's constant, and r is the radius of the nanoparticle.

Work done by Gor'kov and Eliashberg, and followed by Marquardt and Nimtz on the size-dependent dynamic electric susceptibility (χ_e) of metallic nanoparticles in a microwave field shows that a quasi-DC quantum model can be used (the size difference between the photons and the nanoparticles is 6–8 orders of magnitude, and microwave frequencies are much lower than the plasmon frequency). The resulting size dependent dielectric function equation becomes: [20, 21]

$$\varepsilon * \; = 1 + \frac{m k_F (2r)^2}{20\pi^2 a_B} + \; \frac{139}{1200\,\pi^2 a_B}\left(2 + i\frac{\omega m k_F (2r)^3}{6\hbar}\right) \qquad [1.6]$$

Where m is the effective electron mass, k_F is the magnitude of the Fermi wave vector, a_B is the Bohr radius, and $\hbar$ is the reduced Plank's constant. As the nanoparticle grows, it goes from a semi-conductor to more increasingly metallic characteristics. Note that this equation predicts that tan δ will go up proportionally to the diameter of the nanoparticle, and only the loss (ε") will have a frequency dependence.

Work on size-dependent magnetic properties is more recent, and more complicated. The frequency-dependent magnetic permeability equations developed by Landau, Lifshitz and Gilbert are:

$$\mu * = \; 1 + \frac{(4\pi M_S)^2}{2K - \left(\frac{\omega}{2\pi\gamma}\right)^2 + i\alpha(4\pi M_S)\left(\frac{\omega}{2\pi\gamma}\right)} \qquad [1.7]$$

Where γ is the gyromagnetic ratio, α is the dampening factor, K is the crystalline anisotropy and M_s is the saturation magnetization.[22]

Both K and M_s are size and shape dependent, with the size dependency of K as[23]

$$K = K_v + \frac{6}{2r} K_s \qquad [1.8]$$

where K_v is the crystalline anisotropy, and K_s is the surface anisotropy.

The size dependency of M_s is[24]

$$M_{\text{s nano}} \approx M_{\text{s bulk}} \left(1 - \frac{d}{r}\left(1 + \frac{S_{\text{vib}}}{3R}\right)\right) \quad [1.9]$$

where $M_{\text{s bulk}}$ is the bulk magnetic saturation moment, d is the atomic diameter, S_{vib} is the vibrational melting entropy, and R is the ideal gas constant.

1.2.3 Temperature Dependency

The Debye equation for dielectrics gives equations for the real and imaginary part of the complex dielectric function at a known frequency:

$$\varepsilon' = \varepsilon_\infty + (\varepsilon_{\text{s}} - \varepsilon_\infty)\frac{e^{-z}}{e^{z}+e^{-z}} \quad [1.10]$$

And

$$\varepsilon'' = (\varepsilon_{\text{s}} - \varepsilon_\infty)\frac{1}{e^{z}+e^{-z}} \quad [1.11]$$

Where ε_{s} is the static dielectric function, ε_∞ is the dielectric function at infinite frequency (in general, the index of refraction squared is a good approximation), z is ln ($\omega\tau$), ω is the frequency in radians, and τ is the relaxation time. ε_{s}, ε_∞, and τ are all temperature dependent variables. [16]

For a polar liquid or a disordered polar solid (i.e., the temperature is above the critical order–disorder transition) an applied electric field aligns the molecules, reducing entropy, and thus reducing ε_{s}.[25] It then follows that ε_{s} - ε_∞ is inversely proportional to temperature (ε_∞ has negligible a change with T for most liquids)

$$\varepsilon_{\text{s}} - \varepsilon_\infty \propto \frac{1}{T} \quad [1.12]$$

And

$$\tau \propto \frac{\nu(T)}{T} \propto e^{1/T} \quad [1.13]$$

assuming an Arrhenius model for the temperature dependent viscosity – $v(T)$ – of a fluid. Plugging 1.12 and 1.13 into 1.10 and 1.11, then taking into account that one generally measures a room temperature dielectric function as a starting point; it then follows that for a polar liquid

$$\varepsilon'_T \cong \varepsilon'_0 \left(1 + \left(\frac{1}{\Delta T}\right) \frac{e^{-1/\Delta T}}{e^{1/\Delta T + e^{-1/\Delta T}}}\right) \quad [1.14]$$

And

$$\varepsilon''_T \cong \varepsilon''_0 \left(1 + \left(\frac{1}{\Delta T}\right) \frac{1}{e^{1/\Delta T + e^{-1/\Delta T}}}\right) \quad [1.15]$$

Where ε'_0 and ε''_0 are the real and imaginary dielectric function at a known temperature and ΔT is the change in temperature from that known temperature (i.e. if ε'_0 is known at 20 °C, then the calculation for ε'_T at 30 °C uses a ΔT of 10).

For an ordered polar solid (below the critical temperature), an applied electric field reduces order and thus increases entropy and dielectric function loss. Pure metals have critical temperatures equal to the melting point,[26] while alloys have critical temperatures below the melting point. The reaction temperatures in this manuscript are well below the melting point of nano Ni. In the case of a solid, the "relaxation time" is dependent on the probability of the atom being found in an equilibrium state and

$$\varepsilon_s - \varepsilon_\infty \propto e^{-1/T} \quad [1.16]$$

and

$$\tau \propto A(T) e^{1/T} \propto e^{1/T} \quad [1.17]$$

Where $A(T)$ is an internal excitation factor that varies slowly with temperature. Again, ε_∞ has a negligible change with T. It follows that for solids

$$\varepsilon'_T \cong \varepsilon'_0 \left(1 + \frac{e^{-2/\Delta T}}{e^{1/\Delta T + e^{-1/\Delta T}}}\right) \quad [1.18]$$

And

$$\varepsilon''_T \cong \varepsilon''_0 \left(1 + \frac{e^{-1/\Delta T}}{e^{1/\Delta T + e^{-1/\Delta T}}}\right) \quad [1.19]$$

All the above equations assume that the change in volume due to thermal expansion is negligible.

Magnetism is also temperature dependent, but whereas the dielectric function losses of solids increase with temperature, the permeability decreases.

$$M_{sT} = M_{s0}\left(1 - AT^{3/2}\right) \quad [1.20]$$

Is the famous Bloch's 3/2's law where M_{s0} is the magnetic saturation at 0 K, and A is a material dependent constant. The vibrational entropy is also temperature dependent[27], based on:

$$S_{vibT} = S_{vib} + C_p \ln\left(\frac{T}{293K}\right) \quad [1.21]$$

Additionally, the temperature dependent coercivity has a 3/2 law similar to that of the magnetic saturation[28]:

$$H_T = H\left(1 - \frac{T}{T_B}\right)^{3/2} \quad [1.22]$$

Where T_B is the blocking temperature. Obviously, above the blocking temperature, equation 1.22 falls apart, and one should set $\mu^* = 1 + 0i$.

Dielectric, ionic and Maxwell–Wagner heating are broadband, i.e., the absorption of photons occurs over a wide range of frequencies.[16] Magnetic heating, on the other hand, generally has one frequency at which maximum absorption occurs, though absorption at other frequencies still occurs. At the nano-scale, this peak frequency is dependent on the material as well as the shape and size of the particle.[29, 30] This can be theoretically derived using Kittel's equation, where K is the anisotropic constant, and γ is the gyromagnetic ratio.

$$2\pi f = \gamma \frac{4|K|}{3\mu_0 M_s} \quad [1.23]$$

The anisotropic constant of nanoparticles is much higher than that of bulk metals, due to the much higher surface anisotropy.

1.3 Bringing It All Together: Microwave Power Absorption and Heating

1.3.1 Bulk Heating

As the microwave radiation is absorbed, it is converted into heat. By equating the absorbed power to the calorimetric equation, one can calculate the temperature rise of the material being irradiated[16].

$$M\ C_p \frac{\Delta T}{t} = \frac{1}{2}\omega\varepsilon_0\varepsilon''_{\text{eff}} \int_V \left(\vec{E}^* \cdot \vec{E}\right) dV \qquad [1.24]$$

Where M is the mass, C_p is the specific heat capacity, ΔT is the change in temperature, t is time, ω is frequency, ε_0 is the permittivity of free space, $\varepsilon''_{\text{eff}}$ is the lossy permittivity of the material, V is volume, $\vec{E}^*$ is the complex conjugate of the electric field, and $\vec{E}$ is the electric field. In addition, Eqn 1.24 can be modified to include absorption and heating of magnetic materials, by taking into account the complex magnetic permeability of a material, Eqn 1.3.

As the microwave radiation penetrates into a material, its absorption can be described by a decaying exponential. The penetration depth, D_p, is defined as the thickness required to reduce the power to 1/e (or by 63%) of its original value. For nonconducting, nonmagnetic materials, D_p can be calculated using[16]:

$$D_p = \frac{\lambda_0}{2\pi(2\epsilon')^{1/2}} \left[(1+\tan\delta)^{1/2} - 1\right]^{-1/2} \qquad [1.25]$$

The skin depth, δ_s, is analogous to D_p but for amplitude rather than power, and is generally used only in reference to metals. As expected, it takes five D_p or δ_s to shield against >99% of a microwave field. δ_s can be calculated by:

$$\delta_s = \left(\frac{2}{\omega\mu_0\sigma}\right)^{1/2} \qquad [1.26]$$

where μ_0 is the permeability of free space[16].

In a microwave reaction, the heating rate will depend on the ability of the solution to absorb the microwave energy. This can be described as the probability of absorption which scales with the penetration depth of the microwave energy (D_p), and the thickness of the material being irradiated (x).

$$P_{\text{abs}} \propto e^{-x/D_p} \quad [1.27]$$

It can be seen, then, that it takes five times the penetration depth (or skin depth) to shield against >99% of a microwave field[16].

1.3.2 Microwave Reactions for Nanoparticle Synthesis

Typical nanoparticle synthesis begins with organometallic compounds or metallic salts, that are either reduced or thermally decomposed. Rapid, even nucleation is important for uniform nanoparticles, and microwave synthesis provides this. Additionally, quick growth of the nanoparticles is important to avoid Ostwald ripening, which would disrupt the uniformity of the nanoparticles.

In a microwave reaction, the high–energy flux input can potentially drive a reaction over its kinetic energy barrier to proceed to completion. In particular, less–reactive precursors can be used in a microwave reaction compared to a similar thermal reaction, since the microwave energy can drive the reaction.[31,32] Recent work by de la Hoz has indicated that, in addition to tan δ, the activation energy is an important factor in determining whether a reaction will have a noticeable improvement when performed in a microwave reactor.[13] Such effects are particularly important in forming nanometals within a microwave cavity.

Transition metal nanoparticles are known to grow in a two-part synthesis, starting with nucleation and moving to autocatalytic growth.[33,34]

$$A \xrightarrow{\text{yields}} B$$

$$A + B \xrightarrow{\text{yields}} 2B$$

Where each of these two steps has its own reaction rate. *A* to *B* nucleation with rate k_1 and *A*+*B* autocatalysis with rate k_2 in the Arrhenius equation.

$$k = Ae^{-E_a/k_b T} \quad [1.28]$$

The synthesis of nickel nanoparticles involves the thermal decomposition of an organometallic compound. In the proposed research, Ni $(acac)_2$ will be the organometallic compound. In this reaction, oleylamine acts as a reducing agent, as shown in Scheme 1.1.[35] Measurements of the dielectric function of oleylamine (tan δ= 0.03 at 2.45 GHz, STP) and Ni $(acac)_2$ (tan δ =0.006 at 2.45 GHz, STP) indicate that for this reaction the solvent will, initially, absorb more radiation than the Ni precursors. Eventually, though, the growing Ni nanoparticles will have a much higher tan δ than the solvent, and will become the primary source of heating.

1.4 Measuring Microwave Interactions via Dielectric Function Spectroscopy

1.4.1 Cavity Perturbation

As one can see, being able to measure ε', ε'', μ', and μ'' is fundamental to understanding how a chemical system will respond to microwave radiation. The perturbative method will be used qualitatively in this thesis. A full description of how to use it quantitatively is given, but the limitations of the technique demand its use qualitatively, given the experimental parameters. Figure 1.2 shows a simple block diagram of this approach. A standing wave is set up inside a piece of shorted waveguide, designed to resonate at a single frequency, which is measured empirically by a vector network analyzer (VNA). In the waveguide, a standing wave can have areas of pure electric field, and other areas of pure magnetic field. By inserting a material under investigation into an area of pure electric field, one can observe on the VNA how the resonance frequency of the cavity shifts in response to the permittivity of the material. A shift of the peak

Scheme 1.1: Proposed pathway for reduction of nickel by oleylamine.

position is related to the real permittivity of the material, while a broadening of the resonance peak is an indication of the lossyness of the material.[36] A resonant cavity or, as it is sometimes called, a *cavity resonator*, is a short waveguide whose ends are capped with plates. This allows an electromagnetic wave of the proper frequency given the dimensions of the resonator to resonate inside of the cavity, hence the name. The reason an electromagnetic wave can resonate inside a hollow conductor is related to the behavior of an LC circuit.[37]

Resonant cavities are often used in research, but they do have real world applications, i.e. radar. The research use of resonant cavities focuses on understanding the electromagnetic properties of materials, especially with radiation in microwave frequencies. As we have a standing wave inside the cavity, any material inserted in the cavity (solid, liquid, or gas) will affect the wave with respect to the material's complex dielectric function properties. A resonant cavity has a very large quality factor and is therefore very sensitive to even the smallest perturbations of the electromagnetic radiation inside itself.

Slater's perturbation theory, simply put, says that any dielectric material inserted into a resonant cavity will shift the resonant frequency of the cavity in a manner proportional to the volume and the dielectric function of the material. Resonant cavities designed for microwave frequencies work best for this application because they are small enough to be managed on a desktop, but large enough that the dielectric samples can be manipulated. By measuring the frequency shift for various known volumes of a sample, one can find the dielectric function of the sample for the original resonant frequency. If one does this for multiple frequencies, one can determine a trend in the complex dielectric function.[36]

Any material inserted into the cavity will perturb the electromagnetic field. Two small holes are cut in the top plate of the cavity, one in the center and one on the edge. As can be seen

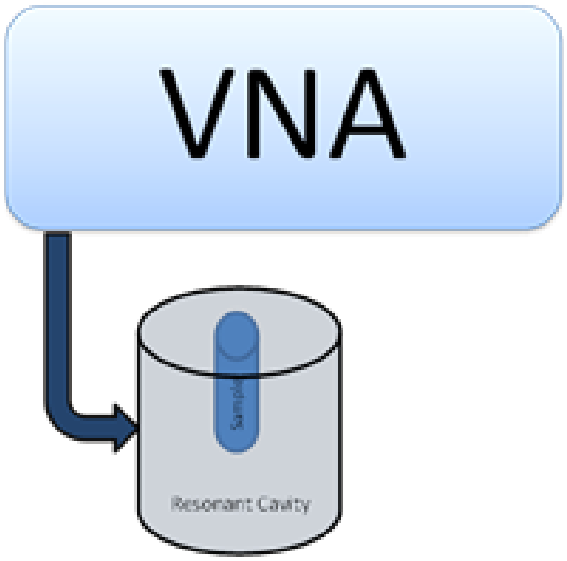

Figure 1.2: A block diagram of a resonant cavity set up. The sample is inserted into the center of the resonant cavity and the perturbation of the EM field is measured.

from Figure 1.3, a material sample inserted in the center hole will perturb the electric field, and a sample inserted on the hole on the edge will perturb the magnetic field. How the material affects the frequency of the resonance tells us if the material is a conductor or a dielectric. The holes drilled in the top plate affect the electric and magnetic field patterns slightly, but only near the boundary surfaces. Fortunately, for accurate measurements, one simply avoids going too near any of the surfaces, because the oscillating electric and magnetic fields are difficult to describe near the interface.[38]

This effect was first noted by J.C. Slater during his tenure at MIT and Bell Laboratories in the early to mid 1940s. Slater's perturbation theory is straightforward, but far from simple. Slater noted that the complex dielectric function can be measured by measuring the Q factor of the empty cavity and the change in the resonant frequency of the cavity when the sample has been inserted.[36]

For a cylindrical rod inserted parallel to the electric field, Slater found that

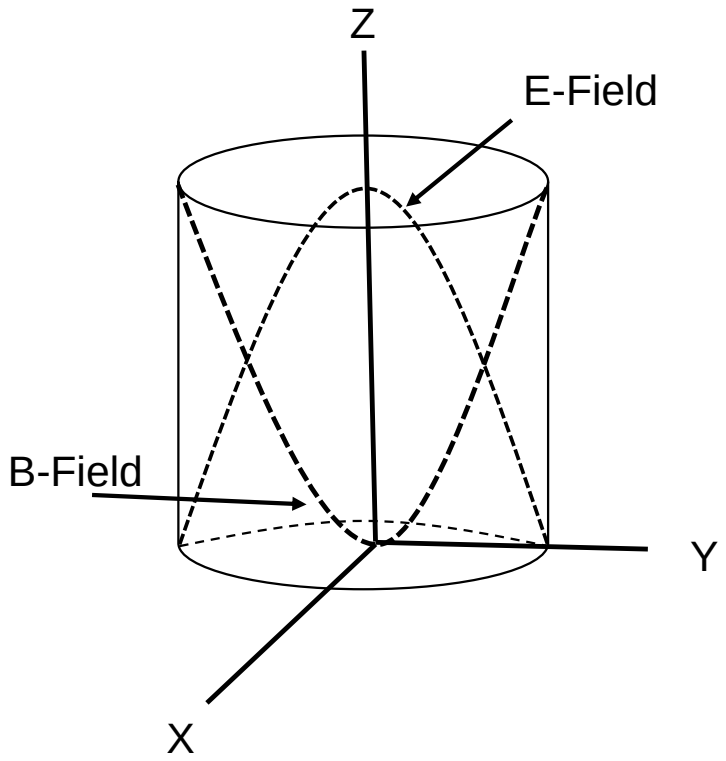

Figure 1.3: Separation of the electric and magnetic fields in a cylindrical resonant cavity set in TE_{010} mode.

$$\frac{\Delta f}{f} - i\Delta\frac{\varepsilon''}{\varepsilon'} = -\frac{\int_v(\varepsilon'-1-\varepsilon'')E^2 dv}{2\int_V E^2 dV} \qquad [1.29]$$

Where Δf is the resonant frequency shift caused by the perturbation of the cylindrical rod volume v, ε' and ε" are the real and imaginary parts of the complex dielectric function respectively, V is the cavity volume, and E is the electric field in the cavity. It is assumed that the change in the electric field itself is negligible compared to the electric field in the unloaded cavity (i.e, this must be a sample with a low ε' and ε"). Also note that v must be much smaller than V (one tenth or less). The higher the quality factor, the more accurate the measurement of the dielectric function. [36, 39]

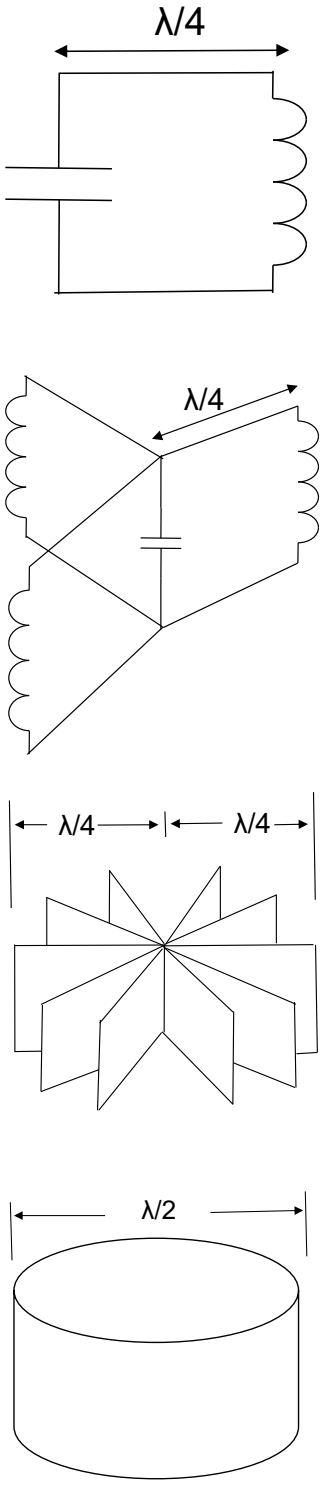

Figure 1.4: Quarter-wave sections looped in parallel, increasing until a cylindrical resonant cavity is produced

This perturbation is caused by the fact that a resonant cavity acts like the inductor and capacitor combination of an LC circuit. We will now go into more detail on how this is so. First, consider a typical LC circuit, such as you would see in any electronics class (Figure 1.4).
It is known that for an LC circuit to handle higher frequencies, one can add a half-turn loop in parallel with the inductor–capacitor combination. This does not affect the resonant frequency of the circuit, as the parallel inductance increases the frequency and the parallel capacitance decreases the frequency; therefore the resonant frequency remains stable. By adding more and more loops, one can increase the circuit's ability to handle higher frequencies. Eventually, enough loops are added, and a cylindrical resonant cavity is formed. By adding a waveguide to act as the wire and supplying the microwaves from a source such as a VNA, one has a "microwave circuit."[40]

The quality factor is calculated using the resonant frequency of the cavity and the full width at half-power of the shifted frequency; the narrower the shifted frequency, the higher the *Q* value. A silver coated resonant cavity can have a *Q* value in the 1000's, where a simple LC circuit will only have a *Q* value in the 10's.[38]

$$Q = \frac{\varepsilon'}{\varepsilon''} = \frac{1}{\tan\delta} \qquad [1.30]$$

where the ratio of the energy stored to the energy lost can be found by t half maxima width of the frequency shift.[38]

1.4.2 Transmission Line Methods

1.4.2.1 Nicolson – Ross – Weir

The main methods that will be used for the experiments described in this dissertation—given the versatility of being able to use liquids, fine powders, or solids along with broad frequency range capabilities and high loss samples—are transmission lines.

Transmission line methods involve placing the material to be investigated inside a portion of an enclosed transmission line to measure both the ε^* and μ^*. The line is usually a section of rectangular waveguide or coaxial airline, and is attached to a VNA, which produces one mW of microwave radiation over a broad frequency range. ε^* and μ^* can then be computed from the attenuation and phase measurements of the reflected signal and transmitted signal (known as the S-parameters, S_{11}, S_{21}, S_{22}, and S_{12}) via a data reduction method determined from experimental parameters.[41] Figure 1.5 shows a simple block diagram of this. Transmission line methods, which are standard in the literature, will be used to measure and evaluate the electromagnetic absorption of the composite samples.[42,43] The Nicolson–Ross–Weir (NRW) algorithm, which uses the Fresnel–Airy formulas to separate the magnetic losses from the electric losses, can be used for known materials known to be ferromagnetic.[44] The attenuation and phase measurements of the signal reflected (S_{11}) by and transmitted (S_{21}) through the sample. These parameters are then used to yield an equation that decouples ε^* from μ^*. These equations are elegant, but have discontinuities for low-loss samples at integer multiples of ½ λ. A workaround is to measure a sample less than ½ the shortest wavelength of the system, but this is not always practical, and very small samples have high uncertainties in these measurements. Another workaround is to measure multiple samples of different lengths and combine the results, but this requires one to have multiple samples available, which is not always possible for materials that are rare or hard to produce.

1.4.2.2 NIST "Eps from Transmission" and Baker-Jarvis

For non-magnetic materials ($\mu^* = 1 + 0i$), the Baker–Jarvis algorithm is generally used. The Baker–Jarvis algorithm is a modification of the NRW algorithm, and requires an initial estimate at the lowest frequency being investigated, as it uses Newton–Raphson numerical

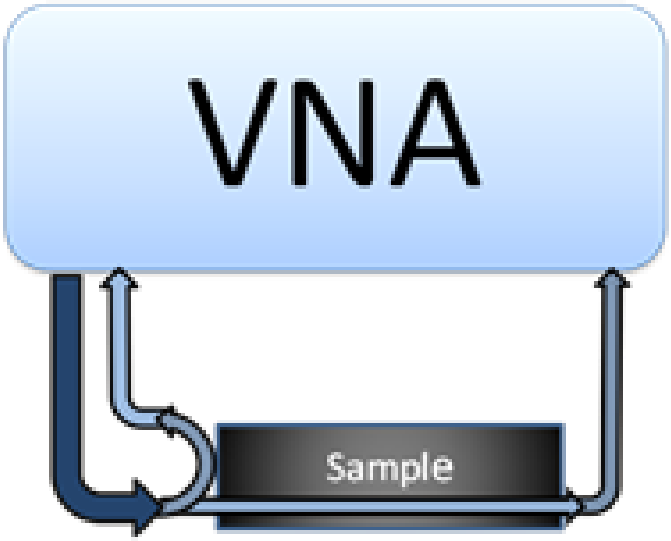

Figure 1.5: A block diagram of a transmission line set up, showing radiation reflected, transmitted, and absorbed by the sample.

iteration to reach an answer within researcher stated tolerances. The NRW algorithm is used to find this initial estimate.[41] This method does not suffer from the dicontinuities of the NRW method, and is useful for both high- and low-loss materials. So even though one must start with using the NRW algorithm, it is more efficient to use Baker–Jarvis than to do multiple samples as may be necessary with the NRW method. Baker–Jarvis also only requires S_{11} or S_{21}, but is more robust if both are used. Of course, in today's modern VNAs, measuring both is not an issue.

1.5 Microwave Generation

1.5.1 Magnetrons

The most common source of microwave generation, in both the lab and the home, is the cavity magnetron. The magnetron is a self-oscillating, high-powered vacuum tube requiring no external elements other than a power supply. A well-defined threshold anode voltage must be applied before oscillation will build up; this voltage is a function of the dimensions of the

resonant cavity and the applied magnetic field. Electrons pass by the openings to these cavities and cause radio waves to oscillate within, similar to the way a guitar resonates sound from its sound box via the oscillation of its strings. The frequency of the microwaves produced, the *resonant frequency*, is determined by the cavities' physical dimensions. Unlike other vacuum tubes such as a klystron or a traveling-wave tube (TWT or TWTA), the magnetron cannot function as an amplifier to increase the intensity of an applied microwave signal; the magnetron serves solely as an oscillator, generating a microwave signal from direct current electricity supplied to the vacuum tube.[45]

The most common magnetron in use today is the cavity magnetron. In a cavity magnetron, the oscillation is created by the physical shaping of the anode, rather than external circuits or fields. The modern magnetron is a fairly efficient device; in a microwave oven, for instance, a 1.1-kW input will generally create about 700 W of microwave power, an efficiency of around 65%. The magnetron remains in widespread use in roles that require high power, but where precise control over frequency and phase is unimportant.[45]

Physically, a magnetron consists of a large cylinder of metal with a hole drilled through the center of the circular face. A wire acting as the cathode is run down the center of this hole, and the metal block itself forms the anode. Around this hole, known as the *interaction space*, are a number of similar holes drilled parallel to the interaction space, which is only a very short distance away. A small slot is cut between the interaction space and each of these additional holes, which comprise the *resonators*. The parallel sides of the slots act as a capacitor and the anode block acts as an inductor. Thus, each cavity forms its own resonant circuit, the frequency of which is determined by the energy of the electrons and the physical dimensions of the cavity.[3]

In a magnetron, the magnetic field is set to a value well below critical, so the electrons follow arcing paths towards the anode. When the electrons strike the anode, they cause it to become negatively charged in that region. As this process is random, some areas will become more or less charged than the areas around them. The anode is constructed of a highly conductive material, almost always copper, so these differences in voltage cause currents to appear to equilibrate the areas. Since the current has to flow around the outside of the cavity, this process takes time. During that time additional electrons will avoid the hot spots and be deposited further along the anode, as the additional current flowing around it arrives. This causes an oscillating current to form as the current tries to equalize one spot, then another. The oscillating currents flowing around the cavities, and their effect on the electron flow within the tube, causes large amounts of microwave frequency energy to be generated in the cavities. The cavities are open on one end, so the entire mechanism forms a single microwave oscillator.[3]

As the oscillation takes some time to develop, and is inherently random at the start, subsequent startups will have different output parameters. Phase is almost never preserved, which makes the magnetron difficult to use in phased-array systems. Frequency also drifts from pulse to pulse, a more difficult problem for a wider array of radar systems. The sizes of the cavities determine the resonant frequency, and the frequency of the emitted microwaves. However, the frequency is not precisely controllable; the operating frequency varies with changes in load impedance, with changes in the supply current, and with the temperature of the tube. This is not a problem in uses such as heating, or in some forms of radar where the receiver can be synchronized with an imprecise magnetron frequency. Where precise frequencies are needed, other devices such as a traveling wave tube are used.[45]

1.5.2 Traveling Wave Tube Amplifiers (TWTA)

A traveling wave tube (TWT) is a specialized vacuum tube that is used in electronics to amplify radio frequency (RF) signals in the microwave range. The TWT belongs to a category of "linear beam" tubes, such as the klystron, in which the radio wave is amplified by absorbing power from a beam of electrons as it passes down the tube.[40]

A major advantage of the TWT over magnetrons is its ability to amplify a wide range of frequencies. The bandwidth of the helix TWT can be as high as two octaves, while the cavity versions have bandwidths of 10 to 20% around the center frequency. Operating frequencies range from 300 MHz to 50 GHz. The power gain of the tube is on the order of 40 to 70 dB, and output power ranges from a few watts to megawatts.[40]

A TWT is constructed of an elongated vacuum tube with an electron gun (a heated cathode that emits electrons) at one end. A voltage applied across the cathode and the anode accelerates the electrons towards the far end of the tube, and an external magnetic field around the tube focuses the electrons into a beam. At the other end of the tube the electrons strike a collector, which returns them to the circuit. Coiled around the inside of the tube, just outside the beam path, is a helix of wire, typically made of oxygen-free copper. The RF signal to be amplified is fed into the helix at a point near the emitter end of the tube. The signal is normally fed into the helix via a waveguide or electromagnetic coil placed at one end, forming a directional coupler.[46]

By controlling the accelerating voltage, one can set the speed of the electrons flowing down the tube to a speed matching that of the RF signal running down the helix. The signal in the wire induces a magnetic field in the center of the helix, where the electrons are flowing. Depending on the phase of the signal, the electrons will be either sped up or slowed down as they

pass the windings. This causes the electron beam to "bunch up," known technically as *velocity modulation*. The resulting pattern of electron density in the beam is an analog of the original RF signal.[46]

Because the beam is passing the helix as it travels, and because that signal varies, it causes induction in the helix, amplifying the original signal. By the time it reaches the end of the tube, this process has had time to deposit considerable energy back into the helix. A second directional coupler, positioned near the collector, receives an amplified version of the input signal from the far end of the RF circuit. Attenuators placed along the RF circuit prevent the reflected wave from traveling back to the cathode.[46]

A TWT integrated with a regulated power supply and protection circuits is referred to as a traveling-wave-tube amplifier (TWTA). Broadband TWTAs generally use a helix TWT, and achieve less than 2.5 kW output power. TWTAs using a coupled cavity TWT can achieve up to 15 kW output power, but at the expense of bandwidth.[46]

1.6 Analytical Instrumentation

1.6.1 XRD

Crystals are regular arrays of atoms, and these atoms scatter X-ray-frequency electromagnetic radiation, primarily through the atoms' electron cloud. This phenomenon is known as *elastic scattering*, and the electron is known as the *scatterer*. A regular array of scatterers produces a regular array of spherical waves. Although these waves cancel one another out in most directions through destructive interference, they add constructively in a few specific directions, determined by Bragg's law:[47]

$$n\lambda = 2d \sin\theta \qquad [1.31]$$

Here d is the spacing between diffracting planes, θ is the incident angle, n is any integer, and λ is the wavelength of the beam. These specific directions appear as spots on the diffraction pattern called *reflections*. Thus, X-ray diffraction results from an electromagnetic wave (the X-ray) impinging on a regular array of scatterers (the repeating arrangement of atoms within the crystal). X-rays are used to produce the diffraction pattern because their wavelength λ is typically the same order of magnitude (1–100 Å) as the spacing d between planes in the crystal. To produce significant diffraction, the spacing between the scatterers and the wavelength of the impinging wave should be similar in size.[48]

1.6.2 SEM

A scanning electron microscope (SEM) is a type of microscope that produces images of a sample by scanning it with a focused beam of electrons. The electrons interact with atoms in the sample, producing various signals that contain information about the sample's internal structure and chemical composition. The electron beam is generally scanned in a raster scan pattern, and the beam's position is combined with the detected signal to produce an image. In the most common or standard detection mode, i.e. secondary electron imaging or SEI, the secondary electrons are emitted from very close to the specimen surface. Consequently, SEM can produce very high-resolution images of a sample surface, revealing details less than 1 nm in size. Specimens can be observed in high vacuum, in low vacuum, in wet conditions (in environmental SEM), and at a wide range of cryogenic or elevated temperatures.[48]

The most common SEM mode is detection of secondary electrons emitted by atoms excited by the electron beam. The number of secondary electrons that can be detected depends, among other things, on specimen topography. By scanning the sample and collecting the secondary electrons that are emitted, an image displaying the topography of the surface is

created. Due to the very narrow electron beam, SEM micrographs have a large depth of field yielding a characteristic three-dimensional appearance useful for understanding the surface structure of a sample.[48]

1.6.3 UV–Vis–NIR

Ultraviolet–visible–near–infrared spectrophotometry (UV-Vis-NIR or UV/Vis/NIR) refers to absorption spectroscopy or reflectance spectroscopy in the ultraviolet–visible spectral region. This means it uses light in the visible and adjacent (near-UV and near-infrared [NIR]) ranges. The absorption or reflectance in the visible range determines the perceived color of the chemicals involved. In this region of the electromagnetic spectrum, atoms and molecules undergo electronic transitions. UV/Vis spectroscopy is routinely used in analytical chemistry for the quantitative determination of different analytes such as transition metal ions, highly conjugated organic compounds, and biological macromolecules.[48] Spectroscopic analysis is commonly carried out in solutions but solids and gases may also be studied.

Solutions of transition metal ions can be colored (i.e., absorb visible light) because *d* electrons within the metal atoms can be excited from one electronic state to another. The color of metal ion solutions is strongly affected by the presence of other species, such as certain anions or ligands. For instance, the color of a dilute solution of copper sulfate is a very light blue; adding ammonia intensifies the color and changes the wavelength of maximum absorption (λ_{max}). Solvent polarity and pH can affect the absorption spectrum of a compound or particle.[48,49]

The Beer–Lambert law states that the absorbance of a solution is directly proportional to the concentration of the absorbing species in the solution and the path length. Thus, for a fixed path length, UV/Vis spectroscopy can be used to determine the concentration of the absorber in a solution. It is necessary to know how quickly the absorbance changes with concentration. This

can be taken from references (tables of molar extinction coefficients), or more accurately, determined from a calibration curve.

$$A = \log_{10}\left(\frac{I_0}{I}\right) = \epsilon c L \qquad [1.32]$$

where A is the measured absorbance (in Absorbance Units (AU)), I_0 is the intensity of the incident light at a given wavelength, is the transmitted intensity, L the path length through the sample, and c the concentration of the absorbing species. For each species and wavelength, ϵ is a constant known as the *molar absorptivity* or *extinction coefficient*. This constant is a fundamental molecular property in a given solvent at a particular temperature and pressure, and has units of 1/(M*cm).[49] The Beer–Lambert Law is useful for characterizing many compounds but does not hold as a universal relationship for the concentration and absorption of all substances. A second-order polynomial relationship between absorption and concentration is sometimes encountered for very large, complex molecules such as organic dyes (Xylenol Orange or Neutral Red, for example).[50]

UV/Vis spectroscopy can be applied to determine the kinetics or rate constant of a chemical reaction. The reaction, occurring in solution, must present color or brightness shifts from reactants to products for UV/Vis to be used for this application. The rate constant of a particular reaction can be determined by measuring the UV/Vis absorbance spectrum at specific time intervals. From these measurements, the concentration of the two species can be calculated. An equilibrium constant can also be calculated with UV/Vis spectroscopy. After determining optimal wavelengths for all species involved in equilibria, a reaction can be run to equilibrium, and the concentration of species determined from spectroscopy at various known wavelengths.[49] For nanoparticles, which have an extinction coefficient that increases proportional to r^2, the size dependent extinction coefficient can be found using Mie scattering.[51]

$$\sigma_{\text{ext}} = \frac{9V\epsilon_{\text{m}}^{3/2}}{c} * \frac{\omega\epsilon_2}{[\epsilon_1+2\epsilon_2]^2+(\epsilon_2)^2} \quad [1.33]$$

where V is the volume of the nanoparticle, ε_{m} is the dielectric function of the medium, assumed to be invariant with frequency, c is the speed of light, ω is the frequency being absorbed, and ε_1 and ε_2 are the frequency-dependent real and imaginary parts of the dielectric function of the nanoparticle respectively. The extinction cross-section can then be used to find the size- dependent absorption of the particles in an equation analogous Beer's Law[52]

$$A = \sigma_{\text{ext}} bN \quad [1.34]$$

Where b is the path length of the cell, and N is the number of nanoparticles per unit volume.

CHAPTER 2

SPECIFIC EFFECTS IN MICROWAVE CHEMISTRY EXPLORED THROUGH REACTOR VESSEL DESIGN, THEORY, AND SPECTROSCOPY

These data were previously published in "Specific Effects in Chemistry Explored through Reactor Vessel Design, Theory, and Spectroscopy." *Physical Chemistry Chemical Physics*. **2015**, *17*, pp 27317–27327. **DOI:** 10.1039/C5CP03961D

2.1 Introduction

Much of the excitement of microwave chemistry revolves around the concept that uniform, rapid heating (volumetric heating) is achieved within the reaction vessel when it is irradiated, thus leading to highly efficient product formation by overcoming kinetic and thermodynamic barriers through the addition of external energy. The high efficiency of microwave heating has led to the use of microwave reactors to improve the carbon footprint in chemistry or, in effect, the greenness of preparing desired molecules — a grand challenge in synthetic chemistry. The energy efficiency of conversion of microwave photons to heat has been theorized to lower energy consumption by 72%. [7,8,9,10] In response, a rapid growth of publications utilizing microwave chemistry has appeared in the literature; including in nanoscience following our report on microwave initiated nucleation of reactants leading to uniform nanocrystal growth with extremely shortened reaction times.[6,15,53] Why such drastic microwave enhancement is observed in the reaction rate is intensely debated and, in the case of nanomaterials, the role of microwave photon absorption by the precursors has been suggested.[54,55,56,57,58] In microwave-enhanced nanomaterial reactions, the question of controlled growth likely reflects selective

dielectric function absorption driving nucleation by conversion to thermal energy *via* Debye procesess,[59,60] as opposed to nonthermal effects.[61,62]

To date, microwave synthesis studies have clearly demonstrated that microwave energy is too low to break a chemical bond and, spectroscopically, only excites molecular rotations.[17] Enhanced heating can occur due to selective interactions of microwaves with a susceptor (any highly microwave absorbing material added to the reaction system to enhance heating rates – such as ionic liquids, silicon carbide, or carbon inserts – but that is not a catalyst nor is consumed in the reaction), solvent, polar molecule, magnetic molecule, or the influence of reduced thermal gradients and wall effects.[63,11,12,13,64] The involvement of microwave absorption and its influence on microwave heating result in an inability to directly compare results on identical reactions conducted by different research groups, due to small changes in the reaction system. [14,65,60, 66] For instance, the use of vastly different reaction conditions (pressure, temperature, time), strongly absorbing microwave solvents, different microwave cavity designs, different microwave energies, and/or reactor vessels made of different materials (quartz, glass, SiC) have complicated the discussion of microwave enhancement of rates of reaction. Stiegman attempted to clarify the question by reaction design,[67,68,69] while de la Hoz approached the question by modeling microwave interaction.[13,14] Leadbeater measured the ability of molecules to thermalize in a solvent bath following microwave photon absorption, concluding microwave absorption leads to rapid thermal diffusion rather than directly enhancing a reaction path.[70] Kappe approached the discussion by attempting to eliminate reactant microwave absorption by reaction vessel design using a SiC reaction vessel, and concluded that microwave heating and rapid thermal heating produce the same results in organic reactions.[2, 71] To fully understand the impact of microwave electromagnetic radiation (EMR) on the rates of the reaction, the EMR interaction with the

vessel, the microwave cavity, and microwave absorption (imaginary dielectric function contribution) versus reflectivity (real dielectric function contribution) must be considered as a total system.

In this chapter, we explore the interaction of the microwave field with the reaction system by theoretical modeling and application of dielectric function spectroscopy in order to design a reactor vessel that eliminates microwave penetration into the reactants. The design of the microwave vessel coupled to the experimental results will help research to better elucidate microwave absorption from non-thermal microwave interactions across the synthetic field. The results demonstrate significant microwave penetration through the walls of commercial SiC composite microwave vessels can be eliminated by noble metal plating of the SiC reactor vessel interior. Modeling of the electric field, measuring the complex permittivity, and correlating heating rates of microwave absorbing molecules were accomplished and confirmed by dielectric function spectroscopy and reactant heating experiments. The theoretical and experimental data support the microwave engineering predictions that the interaction of the microwave with the total reaction system is proportional to the ratio of the imaginary to real dielectric function values for the components within the reaction system. The experimental evidence for microwave transparency of standard microwave reactor vessels compared to the SiC-noble metal vessel designed in the chapter is shown by comparing the resonant frequency shift for solvents and small molecule microwave susceptors in a non-microwave absorbing solvent. As anticipated from earlier findings,[8] the addition of a microwave absorbing molecule (Tri-octylphosphine telluride, TOP-Te) into a non-microwave absorbing solvent (toluene) results in a linear increase in heating rate at fixed microwave power as the concentration of the microwave absorbing molecule is increased. The microwave absorption by TOP-Te is confirmed by the measurements

of the dielectric function spectroscopy shift with increasing concentration. The increased reaction temperature should not be confused with microwave selective bond activation, as the absorption of microwave radiation leads to thermal heating of the surrounding solvent bath by phonon coupling.[72,73] Researchers have often missed this nuance, which has lead led to questionable conclusions with respect to the contribution of the microwave field to the reaction,[11,14] leading to conclusions that while partially correct, do not properly describe the reaction system.

In today's highly populated, resource-limited world, the development of low-cost energy efficient synthetic methods is imperative. The results of the study provide an improved platform for microwave syntheses, and clearly demonstrate system design is critical to reaction analysis. The elimination of EMR leakage by vessel design that attenuate 100% of the impingent microwave radiation will allow researchers to better interrogate the complex reaction landscape in microwave chemistry. The understanding of microwave heating phenomena and its impact is not limited to chemical reactions, as it is also important in describing electromagnetic interference (EMI) screening, telecommunications, and the interaction of radar scattering by a surface. Whether the goal is to prepare phosphors for new solid state lighting control, organic material deposition for fabric coatings, new catalysts, or to develop novel EMI shielding technologies for the aerospace and telecommunications communities, advances in the field can only be achieved if the microwave interactions can be properly understood under the reaction conditions, and extrapolated to new ones.

2.2 Experimental

2.2.1 Materials.

Ethylene glycol (Sigma–Aldrich), ethanol (Fisher), acetonitrile (Fisher), and toluene (Fisher) were used without further purification. Concentrated nitric acid (70%) (Sigma–Aldrich), concentrated hydrochloric acid (37%) (Sigma–Aldrich), hydrogen peroxide (30%) (Sigma–Aldrich), potassium hydroxide (Sigma–Aldrich), silver nitrate (VWR), dextrose (Sigma–Aldrich) (3-Aminopropyl)-triethoxysilane (Sigma–Aldrich) and ammonium hydroxide (Sigma–Aldrich) were used without further purification.

2.2.2 Microwave Cross-section

The TOP-Te microwave cross section (tan $\delta = \varepsilon''/\varepsilon'$) values were measured at 2.45 GHz using a coaxial transmission line and MuEpsl software from Damaskos on a vector network analyzer (Anritsu Lightning 37347E). The value for the real (ε') and imaginary (ε'') values for the samples were calculated using the Nicholson–Ross–Weir algorithm. [41] Solvent microwave cross sections were taken from literature.

2.2.3 Microwave Field Perturbation

The perturbation of the microwave field by the reaction system, which includes the reactor vessel, the solvent, and solute, were analyzed by the frequency shift of the S_{11} standing wave reflection generated using the VNA coupled to a TE_{103} resonant cavity tuned to resonate at 2.45025 GHz. The frequency shift and broadening of the S_{11} reflection correlate to the magnitude of ε' and ε'', respectively.

2.2.4 Microwave Heating

Microwave heating was measured for 30 s in an Anton Paar - Monowave 300 operating in a single mode (TE_{10x}) self-tuning cavity at 300 W (constant power) for standard solvents (toluene, acetonitrile, ethanol, and ethylene glycol) with known tan δ and specific heat capacities (C_p). The microwave heating experiments were carried out on 3 mL of solvent in 10 mL reaction vessels composed of silicon carbide (SiC), borosilicate (BS), a silicon carbide with an inner silver coating (Ag/SiC), and an inner gold coating (Au/SiC).The metal coatings are 7 microns Ag and 10 microns Au respectively. The coating of the SiC vessel and borosilicate is described in the following paragraph. The vessels were sealed under ambient conditions, heated for 30 s at 300 W of continuous power with stirring (600 RPM), and the temperature simultaneously recorded externally via an infrared sensor and internally using a ruby thermometer. The experiments were carried out under continuous power to eliminate any issues associated with power oscillations due to differences in absorber strength. The maximum observed temperature (pressure) for SiC is 130 °C (10 bar) and BS 200 °C (10 bar).

2.2.5 Internal Metal Coating of Microwave Reaction Vials

The inside of the reaction vessel was metal plated by Tollens' reagent[74] for silver or electroplated for gold (Component Surfaces, Inc.). Metal coating of the SiC vessel required a more aggressive pre-treatment of the vessel, to ensure a uniform coating of the metal film. The SiC vial was cleaned with concentrated nitric acid (30 min), treated with a solution of H_2O_2, HCl, and D.I. water (1:1:5 v:v:v) for 10 min at 80 °C, and washed with DI water between each step. The cleaned SiC vial was dried under a stream of nitrogen, followed by oxygen plasma etching (100% O_2 atm., 30 W; Herrick Plasma Cleaner PDC-001) for 1 minute. For a silver coating, the SiC vial was activated by exposure to a solution of (3-aminopropyltriethoxysilane

Table 2.1. Microwave and thermal constants for the reaction system.

MATERIAL	ε'	ε"	tan δ	D_p @ 2.45 GHz (mm)	Density (g/mL)	Heat Capacity (J/mL K)	Thermal conductivity (W/cm K)	Thermal Diffusivity (cm^2/s)
SiC	9.57[2]	1.56[2]	0.164[2]	38.6*	---	---	---	---
Borosilicate	4.82[3]	0.026[3]	0.0054[3]	1637.8*	---	---	---	---
TOP-Te	2.63†	0.23†	0.088*	136.2*	~0.831[4]	---	---	---
Toluene	2.4[5]	0.096[5]	0.040[5]	313.4*	0.8669[4]	1.466[4]	0.00151[4]	0.00103*
Acetonitrile	37.5[5]	2.325[5]	0.062[5]	52.9*	0.786[4]	1.756[4]	0.00188[4]	0.00107*
Ethanol	24.3[5]	22.866[5]	0.941[5]	4.8*	0.789[4]	1.918[4]	0.00171[4]	0.00089*
Ethylene Glycol	37.0[5]	49.950[5]	1.350[5]	2.7*	1.1132[4]	2.681[4]	0.00256[4]	0.00095*

*Calculated, †measured

(ATPES) and toluene (volumetric ratio - 1:49) for 24 h, rinsed with toluene, and dried following literature protocol. [75] Approximately ten layers of Ag were deposited by ten sequential plating reactions carried out by addition of Tollens' reagent in the presence of 5 mM dextrose for 10 min. The Ag/SiC vessels were rinsed three times with D.I. water and finally with methanol. Fresh Tollens' reagent was prepared by mixing 12 mM KOH, 3 mM $AgNO_3$, and excess concentrated NH_3. For gold coating the SiC was gold plated commercially by Component Surfaces, Inc.

2.2.6 Modeling Electric Field

COMSOL Multiphysics based on finite-element methods simulated the microwave electric field and its absorption by various materials. To reduce the complexity of the system without losing the general applicability of the simulation, a 2-D waveguide was modeled. The dimensions of 114.41 mm in length and 72.136 mm in height was chosen to match a WR-284 waveguide. The simulated waveguide was composed of a top and a bottom aluminum wall (Fig

2.1). Additionally, the left wall (red line) was assigned as the activation port where the 2.45 GHz TE_{10} mode waveguide was excited; and the right wall (blue line) was designated as a transmitting port, avoiding reflection and interference of the microwave with itself. The physics-controlled mesh (5th wavelength) and extremely fine element size were chosen in mesh setting.

2.3 Results and Discussion

2.3.1 Microwave Interactions with the Reaction System

Designing a reactor vessel for a microwave synthetic reaction and understanding the observed impact of the vessel design on the rate of reaction requires a proper description of the impingent EMR microwave field on the reaction system components. In microwave chemistry, the absorbed microwave photon is converted into thermal energy by damping to the environment through molecular friction, ionic conduction, Ohmic (electron polarization), Maxwell–Wagner (charge oscillation) and magnetic processes.[16] For a typical microwave chemical reaction, the molecular friction and ionic conduction are the primary terms leading to heat generation following microwave absorption. While microwave irradiation can lead to molecular polarization without heat, the heating of a microwave synthetic reaction is due to the microwave photon absorption and scattering behavior of the molecules in the reaction mixture. The interaction of the impingent microwave field on any material is described in terms of the materials complex dielectric function ($\varepsilon^* = \varepsilon' - i\varepsilon''$). In effect, the microwave is absorbed or scattered by the material with the largest ε'' or ε' term in the system, and can be thought of as analogous to a Beer-Lambert law problem in absorption spectroscopy. The real component ε' is the scattering term, describing the ability of the material to store an electric field. The imaginary term (ε'') describes the absorption of the impingent photon, which is converted to heat through molecular motion and

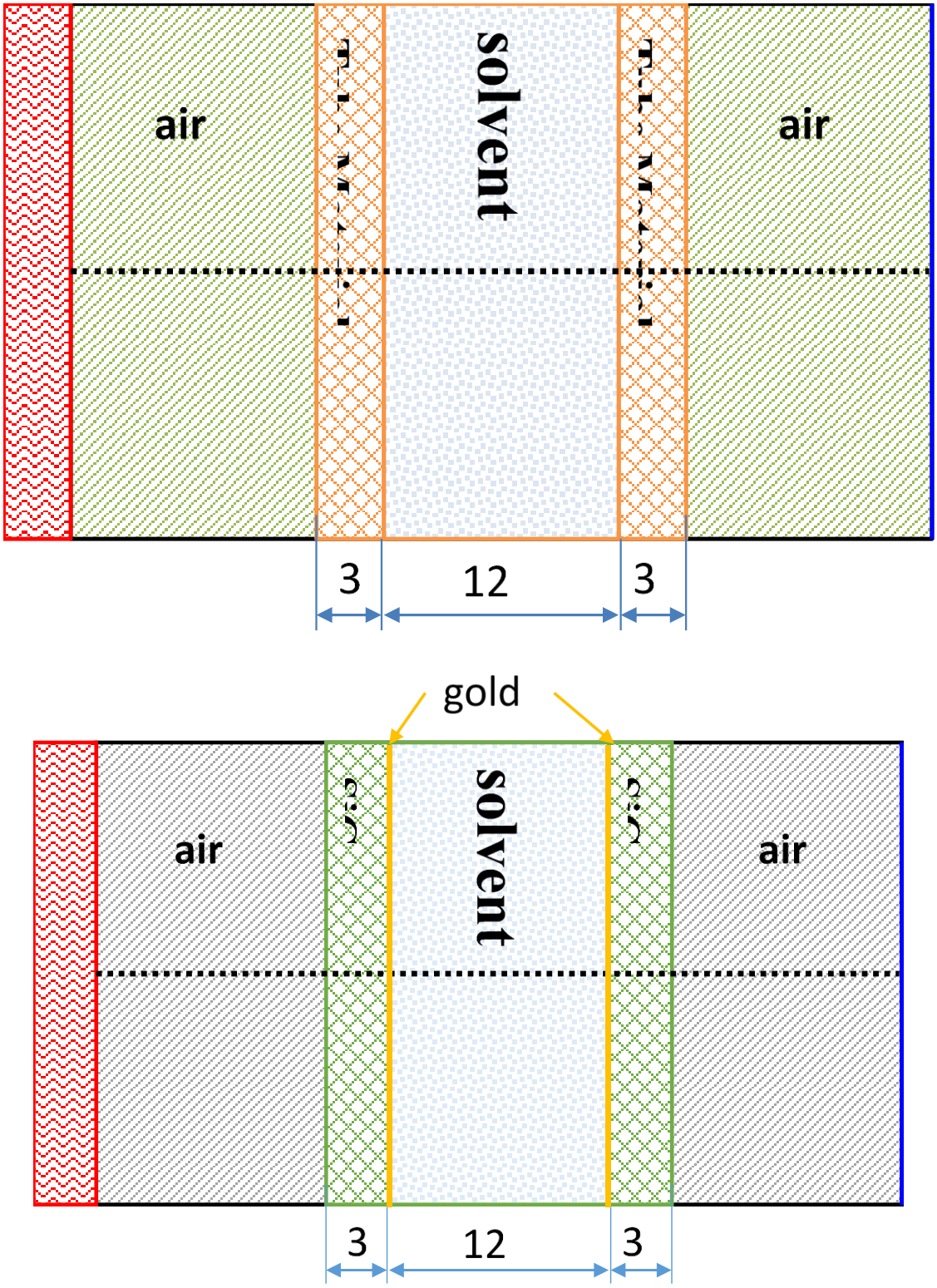

Figure 2.1: Diagram of COMSOL setup; all dimensions are in millimeters. The red rectangle on the left side represents the MW source. The dotted line is a centerline for simulation purposes.

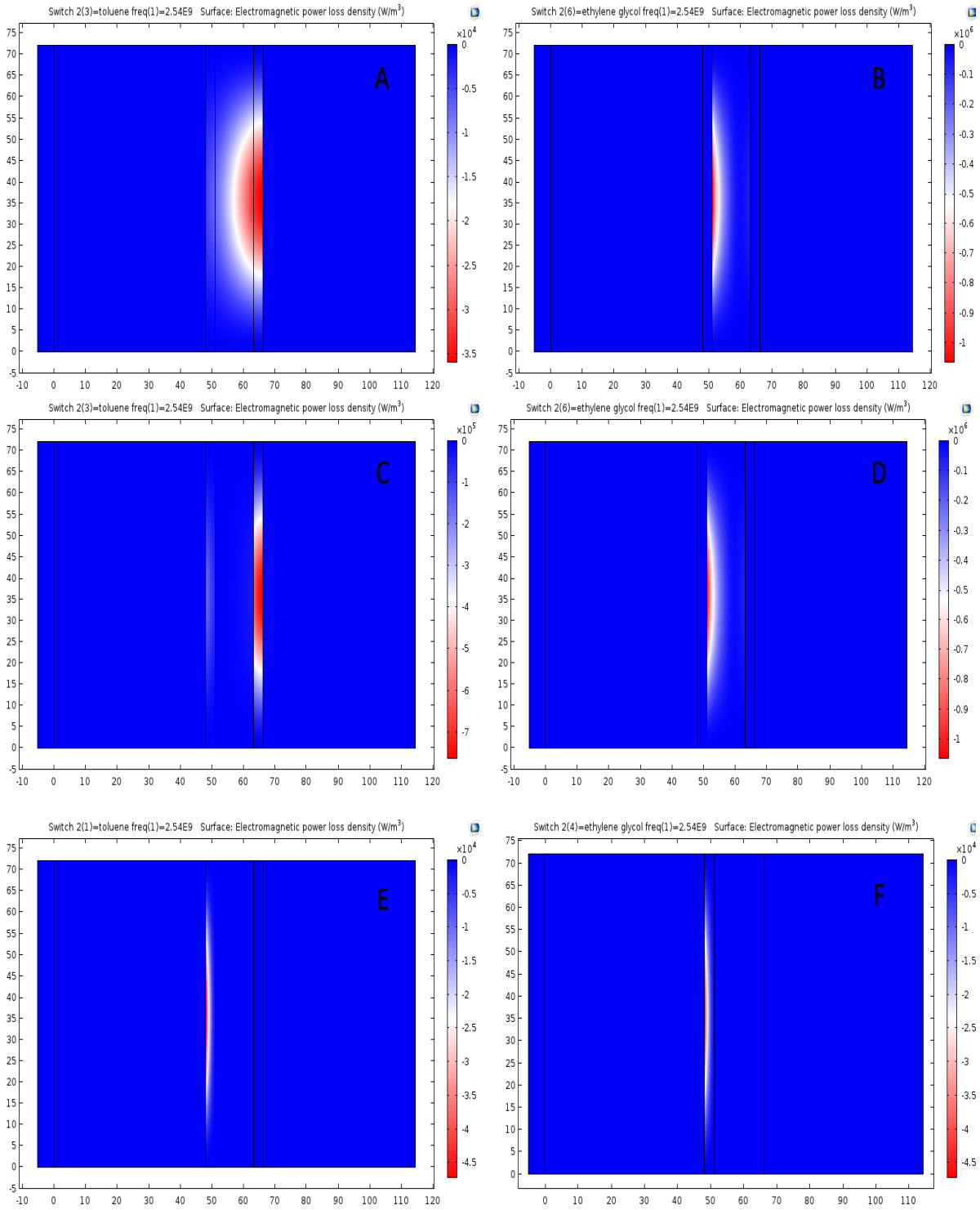

Figure 2.2: COMSOL Simulations of TE_{01} Cavity, excited at 2.45 GHz. A and B are of a BS tube placed in the cavity, C and D are of a SiC tube placed in the cavity, and E and F are of a gold plated SiC tube placed in the cavity. Images show the electric field loss vs. distance.

thermalization to the solvent following electronic excitation in molecules. The imaginary term will have a microwave cross section described in terms of the decrease of EMR amplitude to a value of 1/*e* over a defined material thickness, which is the penetration depth (D_p). The individual heat transfer for the components following microwave photon absorption is dependent on the ability of a material to store electrical charge, as described by ε' (scattering), and the electromagnetic losses or loss factor, represented by ε'' (absorption). Each constituent of the reaction system will have unique ε' and ε'' values, which is often reported in terms of the ratio of the dielectric function components,

$$\tan\delta = \frac{\varepsilon''}{\varepsilon\prime} \qquad [2.1]$$

Where the penetration depth (D_p) is dependent on tan δ, ε', and λ_o, the frequency of the impingent EMR field

$$D_p = \frac{\lambda_0}{2\pi(2\epsilon')^{\frac{1}{2}}}\left[(1+\tan\delta)^{\frac{1}{2}}-1\right]^{-\frac{1}{2}} \qquad [2.2]$$

The ability of the system to interact with the microwave field is specific and will scale as the ratio of tan δ. In Table 2.1, the tan δ and D_p values for selected solvents and molecular precursors used in nanoparticle synthesis is listed, along with the tan δ values for SiC and borosilicate, two common reaction vessels. The tan δ of the vessel, solvent and molecular reactants must considered individually, as the heating will reflect not only the microwave absorption and scattering, but also thermal conductivity and convection of the reaction system to adequately describe the thermal energy conversion process leading to product formation.[16]

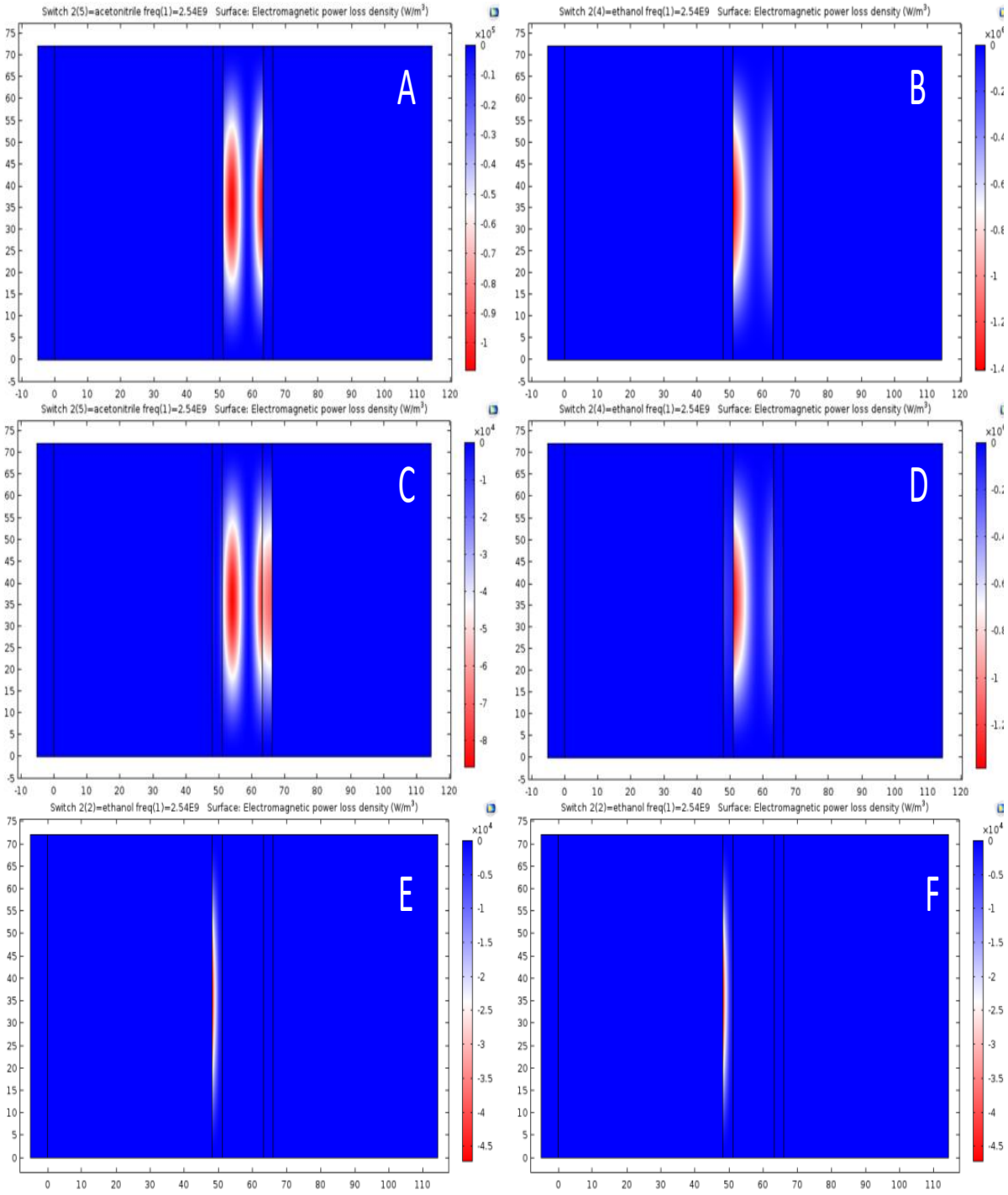

Figure 2.3: COMSOL Simulations of TE_{01} Cavity, excited at 2.45 GHz. A and B are of a BS tube placed in the cavity with acetonitrile and ethanol respectively, C and D are of a SiC tube placed in the cavity acetonitrile and ethanol respectively, and E and F are of a gold plated SiC tube placed in the cavity acetonitrile and ethanol respectively. Images show the electric field loss vs. distance.

The conversion of microwave absorption (ε') to molecular heating is described in terms of the Debye relaxation arising from molecular motion. Since, according to quantum mechanics, molecules can only absorb the whole photon,[76] there is a greater statistical probability that a higher tan δ molecule will absorb a given photon, as demonstrated in earlier microwave engineering literature.[77] Therefore, during a microwave reaction, selective heating in the reaction system occurs due to disproportionate heating of one molecule over another consistent with the magnitude of tan δ and the volume fraction of the molecules in the microwave field. In the absence of a strong microwave interaction with either the vessel or the solvent, the molecular precursors will interact with the microwave photon if they have a large tan δ.

As evidenced in Table 2.1, the magnitude of contribution will be dependent on wall thickness of the vessel, and in the case of a standard microwave reactor vessel (3 mm wall thickness), the microwave can interact with the solvent and reactants in the system, as well as the reactor vessel. From the tan δ values in Table 2.1, it is predicted that synthetic reactions carried out in borosilicate (BS) with ethylene glycol (EG) as the solvent predominately heat by microwave absorption and scattering by the EG. Likewise, reactions carried out in toluene in BS will be dominantly heated by the reactants dissolved in toluene, since BS has a low tan δ and a large D_p. When the reaction vessel is swapped for SiC, the magnitude of tan δ and Dp should lead to a competition between the vessel and the reactants for microwave heating. To accurately predict the magnitude of interaction and thus the effect of the complex dielectric function to heating in the microwave, an electrodynamics simulation of the total reaction system must be carried out.

An electrodynamic simulation to model microwave field penetration into a reaction vessel when operated under an alternating microwave field of 2.45 GHz within the cavity of a

TE_{01} waveguide for a series of solvent and reaction vessel configurations is shown in Figure 2.2 for toluene and EG. The ED simulations for acetonitrile and ethanol are reported in Figure 2.3. A graph of the electromagnetic power loss density (EM loss), which is related to the microwave loss (tan δ), for all solvents is plotted in Figure 2.4. For simplicity, the modeling assumes a 2D boundary condition operating under a single pass configuration to calculate the microwave photon absorption by the total reaction system in the cavity width of the microwave reactor used in this study. In order to simulate the reaction vessel, the 3 mm BS, SiC or Au/SiC walls with a 12 mm inner diameter is modeled as two 3 mm straight walls placed in the middle of the waveguide and separated by the 12 mm solvent volume. The Au/SiC simulation incorporates a 10-micron thick layer on the inner walls. The ED simulation confirms the prediction from Table 2.1 that the BS walls have negligible microwave loss, while the walls of the Au/SiC vessel have the largest EM loss. For the unaltered SiC vessel the situation is more complex. For a SiC vessel containing toluene, SiC wall absorption is the major contributor to EM loss (Figure 2.2c), but in the case of a SiC vessel containing EG, the solvent is the predominant EM loss component (Figure2.2d). The contrast between those two can be easily seen in the line-scan plot (Figure 2.4). The observation in the ED simulation is understandable by considering the differences imaginary permittivity ε'' for each component, such that the highest value leads to the largest microwave loss component to the ED simulated spectra.

The incorporation of the 10 micron noble metal film at the internal wall surface of the reaction vessel eliminates the contribution of microwave penetration into the reaction volume, thus the EM loss can only be observed in the left wall but not in the solvent and right wall. The simulation illustrates that although the tan δ for SiC is large, the large Dp value leads to a condition where the 3 mm wall thickness is inadequate to shield the contents from the impingent

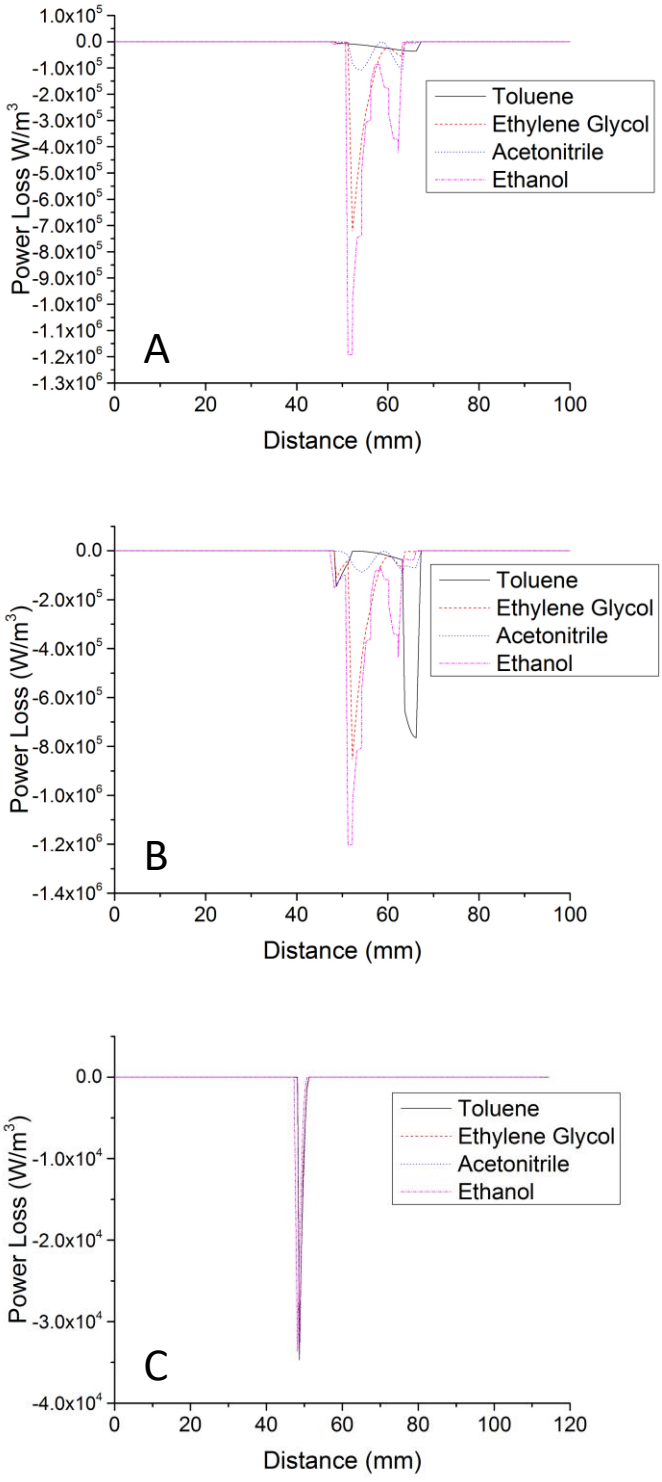

Figure 2.4: Graph of EM Power loss through A) BS, B) SiC and C) Au/SiC microwave vessels with four different solvents in each.

microwave photons. The result is that microwave leakage into the inner volume of a SiC vessel is ~52% of the original microwave photon flux. By contrast, the BS allows ~62% of the impingent microwave field to pass. Incorporation of the noble metal layer on the inside of the SiC vessel reduces the EMR penetration to < 1%.

The electrodynamics simulation predictions can be verified by measuring the microwave interaction for the various solvent, molecular precursor, and vessel configurations using a vector network analyzer (VNA) in a resonant cavity. In Figure 2.5, the resonance shift in the VNA cavity for the BS, SiC, and Au/SiC reaction vessels containing different tan δ solvents is shown. The resonance shift in Ag/BS and Ag/SiC are available in Figure 2.6. The VNA measurement represents a qualitative treatment of Slater's perturbation theory to analyze the microwave interaction with the system. The shift in peak resonance frequency reflects the weighted average ε' contribution, while changes in full width at half maximum (FWHM) correspond to ε''.[36] The measured frequency shift of the S_{11} mode measured in a TE_{103} resonant cavity tuned to the resonate frequency of 2.45025 GHz VNA and the FWHM for air, ethanol (EtOH), ethylene glycol (EG), acetonitrile (MeCN), and toluene in each reaction vessel (BS, SiC, and Au/ SiC) is tabulated in Table 2.2.

As predicted from the ED simulations, the frequency shift and FWHM are more significant in the BS vessel than for identical conditions in the SiC, and there is no observable shift for the Au/SiC reactor vessel due to metal scattering of the microwave photons. The solvent VNA results demonstrate microwave leakage is occurring for the SiC vessel, which is inconsistent with previous reported claims.[71,78] Evidence of the leakage is quantifiable by inspection of the resonance shift for BS vs. SiC where it is observed that the resonant frequency is observed to shift as the solvent polarity increases. If the microwave field was absorbed only at

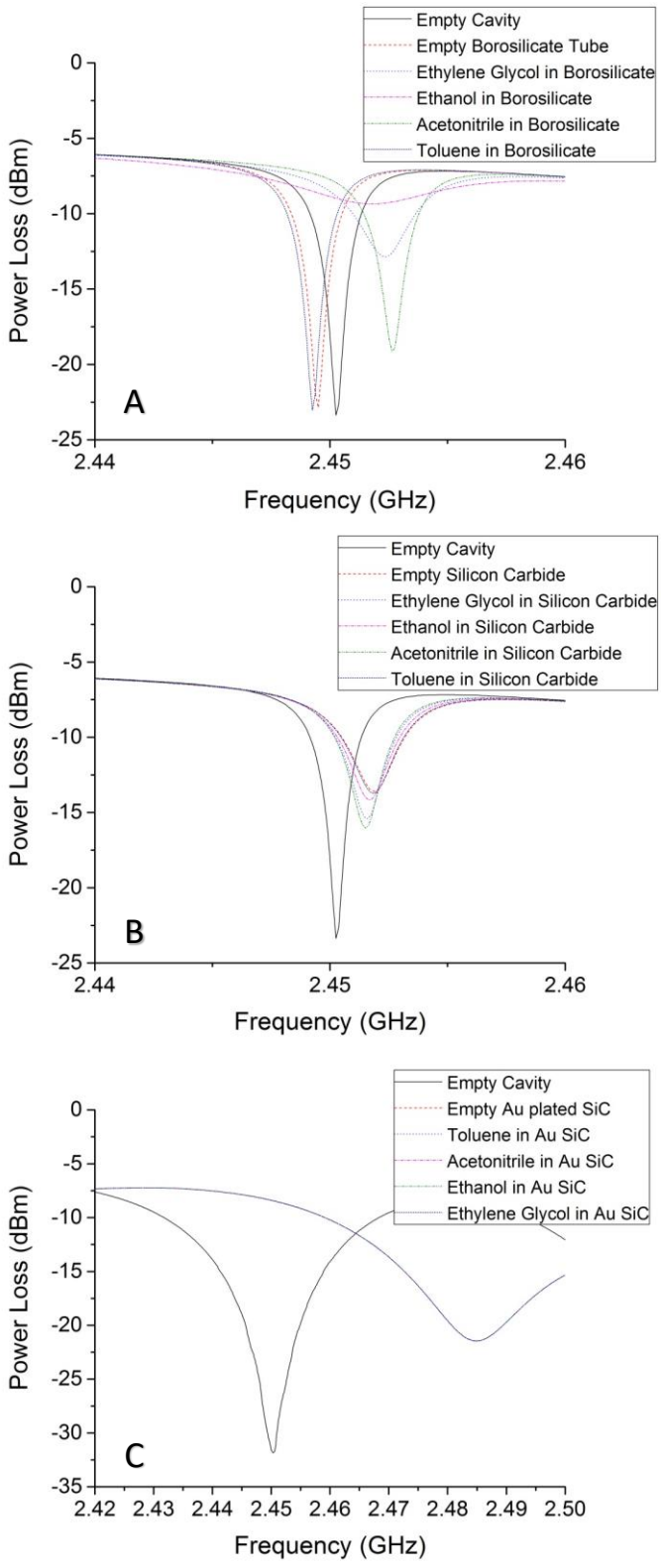

Figure 2.5: Solvent dependent resonance peaks measured in the VNA single mode cavity, A) borosilicate (BS), B) silicon carbide (SiC), and C) gold plated silicon carbide (Au/SiC).

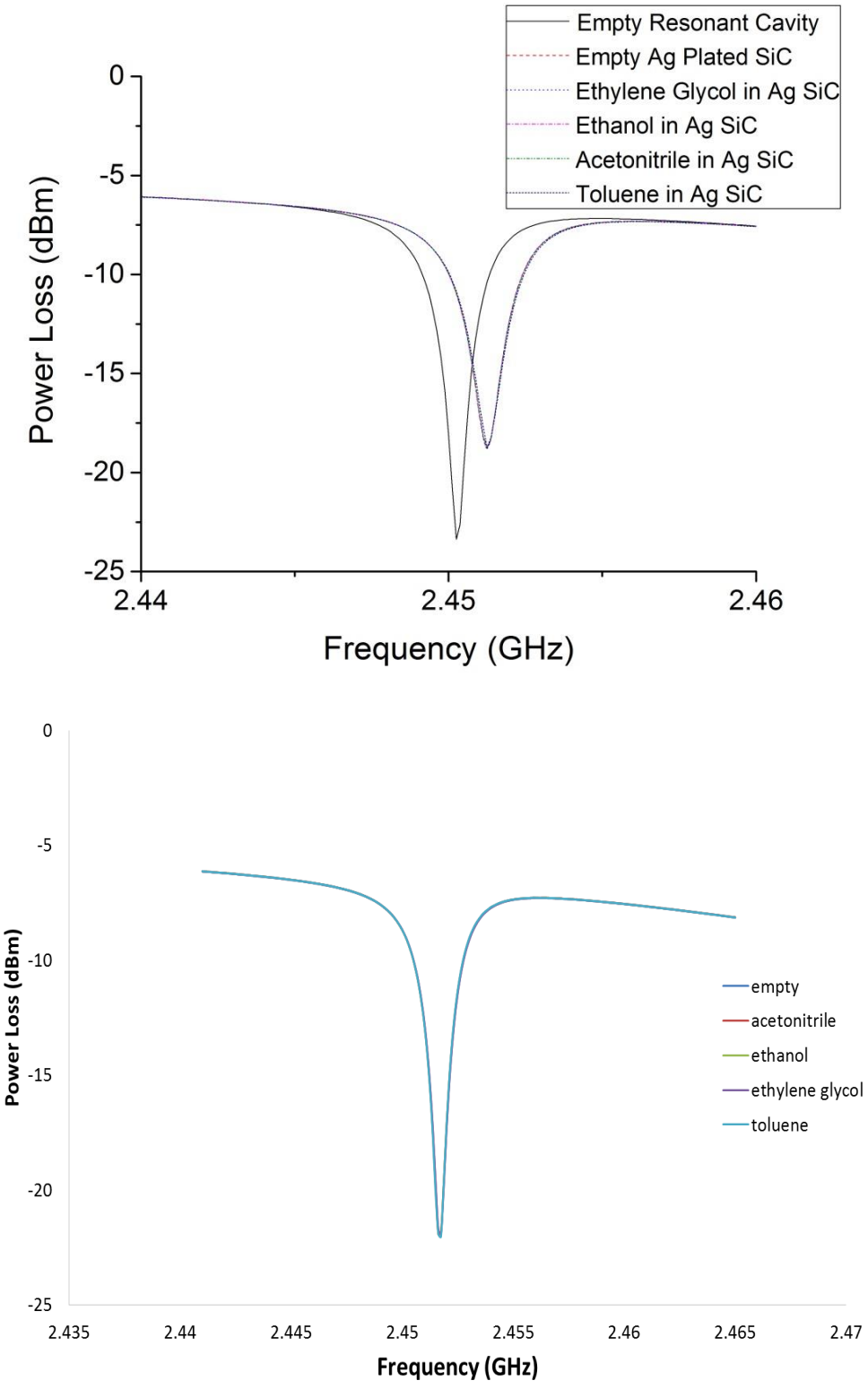

Figure 2.6: Resonance shifts for A) Aug plated SiC and B) Ag plated BS.

the SiC walls, no resonance shift would be observed. The microwave field penetration into the interior of the SiC vessel is easily confirmed by measuring the concentration dependent shift in frequency for a highly polarizable solute in a non-polar solvent. In Figure 2.7, the concentration dependent frequency shift of TOP-Te in toluene is shown in BS, SiC, and Au/SiC. The experimental data yields a definitive resonance shift with increasing concentration of TOP-Te for BS and SiC, but no shift in the Au/SiC vessel. The observed shift is consistent with theoretical treatment of EM fields in the microwave engineering literature, and confirms the microwave photons penetrate a standard microwave SiC and BS vessel. The VNA frequency shift results support the electrodynamics simulations that microwave penetration even through SiC is an important consideration when describing a microwave enhanced molecular reaction.

2.3.2 Microwave Vessel Transparency Effects on Reaction Heating Rates

The potential impact on a chemical reaction in the microwave for a given vessel configuration is most easily understood by measuring the microwave heating rate from room temperature to 100 ^{o}C for the non-polar and polar solvents in the BS, SiC, and Au/SiC plated reactor vessel under identical conditions. To ensure the heating rate is comparable across systems, the experiment is carried out by employing a 30-s pulse at 300 W and comparing the internal temperature measured by a ruby thermometer to the external temperature reported by the IR thermometer. The pressure of the reaction vessel was maintained at ~8–10 bar for all solvents, and an upper temperature limit of 200 °C is used to minimize the effect of changes in tan δ with temperature, since, tan δ decreases as temperature increases in liquids.[16,76]

In Figure 2.8, the heating curves obtained from the ruby (internal) are plotted for each solvent in BS, SiC, and Au/SiC. The heating curve measured by the IR thermometers (external) is available in Figures 2.9. The measured thermal lag (ΔT_t) and the heating rates (dT/dt) are

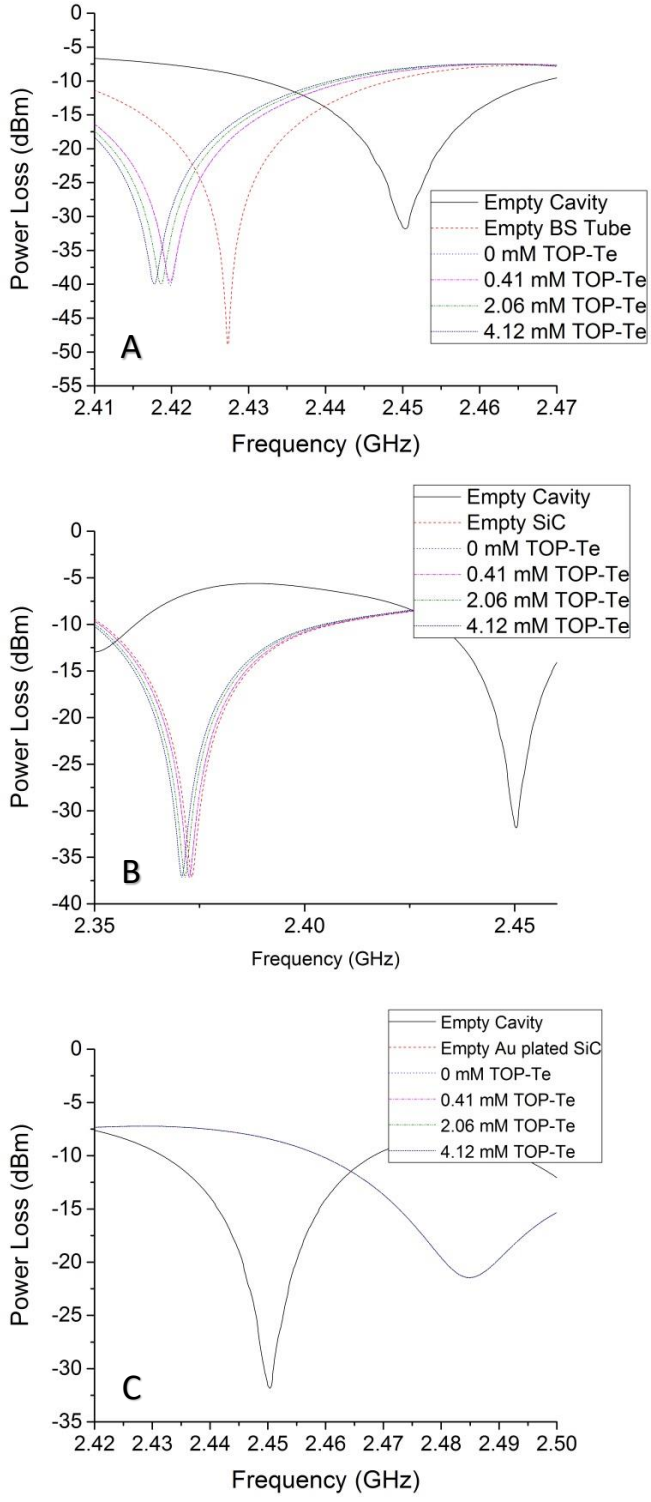

Figure 2.7: Concentration dependent shift in Resonance peaks for ToP-Te dissolved in toluene in A) BS, B) SiC, and C) Au/SiC.

presented in Table 2.2. In BS the thermal lag (3 s) is the same across all solvents and the rate of heating scales with the solvent microwave cross section (tan δ) and is impacted to a lesser degree by thermal diffusivity (Figure 2.9a). For Au/SiC (Figure 2.9d), the ΔT_t and *dT/dt* are solvent dependent, scaling with the solvent thermal diffusivity and not tan δ. The behavior for Au/SiC is consistent with predictions for a microwave opaque reaction vessel design. The SiC vessel (Figure 2.9b) is intermediate between the two extremes with the tan δ influence of the SiC clearly notable. The similarity between SiC and BS support the microwave penetration in to the solvent is occurring and the microwave interaction with reactants can thus not be ignored. While it is clear that the microwave absorption into the solvent raises the reaction temperature, thus increasing reaction rate, it is unclear whether a molecular reactant at concentrations used for the nucleation of a nanocrystal under microwave field in an non-absorbing can play a significant role. To test the potential for microwave driven nucleation arising from the interaction of the microwave photon with the molecular reactant, the heating behavior and VNA results for TOP-Te are analyzed. TOP-Te has been reported to be an effective microwave absorber for initiating CdTe nanocrystal nucleation in the microwave reactor. [15,31] The rate of heating for the TOP-Te solution will be influenced by the tan δ and thermal diffusivity of solvent and vessel. If a vessel absorbs the predominance of energy than the reaction temperature is expected to lag between internal and external temperatures, and more importantly will be independent of the appropriate solvent tan δ, and vice-a-versa. The *dT/dt* plots for TOP-Te (0 mM to 4.12 mM) in toluene for BS, SiC, and Au/SiC are shown in Figure 2.10. The heating curves are shown in Figures 2.11

The effect of microwave absorption into TOP-X when dissolved in a non-microwave absorbing solvent can be understood within the context of the Debye theory that predicts that a

Table 2.2: Frequency shifts and full width at half max measurements for the reaction vessel and solvent configurations.

	BS	Toluene in BS	Acetonitrile in BS	Ethanol in BS	Ethylene Glycol in BS
Frequency Shift (GHz)from 2.45025 GHz	-0.0007	-0.001	0.006	0.0015	0.002
FWHM (GHz)	.00875	0.00875	0.00125	0.00575	0.00225

	SiC	Toluene in SiC	Acetonitrile in SiC	Ethanol in SiC	Ethylene Glycol in SiC
Frequency Shift (GHz)from 2.45025 GHz	0.01625	0.01625	0.00125	0.001375	0.00125
FWHM (GHz)	0.002	0.002	0.0015	0.003	0.0015

	Au/SiC	Toluene in Au/SiC	Acetonitrile in Au/SiC	Ethanol in Au/SiC	Ethylene Glycol in Au/SiC
Frequency Shift (GHz)from 2.45025 GHz	0.0346	0.0346	0.0346	0.0346	0.0346
FWHM (GHz)	0.027	0.027	0.027	0.027	0.027

	BS	0 mM TOP-Te in BS	0.41 mM TOP-Te in BS	2.06 mM TOP-Te in BS	4.12 mM TOP-Te in BS
Frequency Shift (GHz)from 2.45025 GHz	-0.023	-0.03	-0.03	-0.032	-0.325
FWHM (GHz)	0.0044	0.0076	0.0076	0.008	0.0085

	SiC	0 mM TOP-Te in SiC	0.41 mM TOP-Te in SiC	2.06 mM TOP-Te in SiC	4.12 mM TOP-Te in SiC
Frequency Shift (GHz)from 2.45025 GHz	-0.077	-0.077	-0.078	-0.0786	-0.0794
FWHM (GHz)	0.007	0.007	0.007	0.007	0.008

	Au/SiC	0 mM TOP-Te in Au/SiC	0.41 mM TOP-Te in Au/SiC	2.06 mM TOP-Te in Au/SiC	4.12 mM TOP-Te in Au/SiC
Frequency Shift (GHz)from 2.45025 GHz	0.0346	0.0346	0.0346	0.0346	0.0346
FWHM (GHz)	0.027	0.027	0.027	0.027	0.027

polar solute in a nonpolar (relatively speaking) solvent will have a linear dependence of tan δ based on the molar ratios of the solute to solvent as shown in Eqn. 2.3

$$\tan\delta\,(\omega) = C_0 \frac{(\varepsilon'+2)}{\varepsilon' k_b T} \boldsymbol{\mu}^2 \frac{\omega\tau_{\text{mean}}}{1+(\omega\tau_{\text{mean}})^2} \quad [2.3]$$

Where C_0 is a constant dependent on the molar ratios, ε' is the real dielectric function of the solvent, and $\boldsymbol{\mu}$ and τ_{mean} are the dipole moment and the relaxation time respectively of the solute. Eqn. 2.3 correlates the microwave absorption cross section with tan δ and thus solvent heating rate

$$P_{\text{abs}} = MC_p \frac{(T-T_0)}{t} = 0.556x10^{-10}\nu\varepsilon' * \tan\delta * E_{\text{rms}}^2 V \quad [2.4]$$

where C_p of a solution is a weighted average of the solvent and the solute, and at parts per thousand of TOP-Te in toluene can be assumed to be unchanged, thus the temperature is proportional to the change in tan δ for the system, such that

$$P_{\text{abs}} \propto \frac{(T-T_0)}{t} \propto \tan\delta \propto C_0 \quad [2.5]$$

The P_{abs} is proportional to the measured frequency shift in the VNA and the heating rate response is analogous to the Beer–Lambert law in optical absorption studies, as the microwave energy absorption is cumulative to the total reaction system.

The TOP-Te heating rates exhibit a linear concentration dependence for heating with a slope of 0.6 in BS and 0.2 in SiC, consistent with Eqn.2.5. The noble-metal-coated SiC is invariant with concentration reflecting the reduced photon flux penetrating through the SiC due to the stronger absorption by the SiC vessel. The observation of reactant heating in SiC and BS when a microwave transparent solvent is used are further confirmed by comparing the rate of heating for TOP-Te in toluene to the concentration dependent heating curve for TOP-Te in

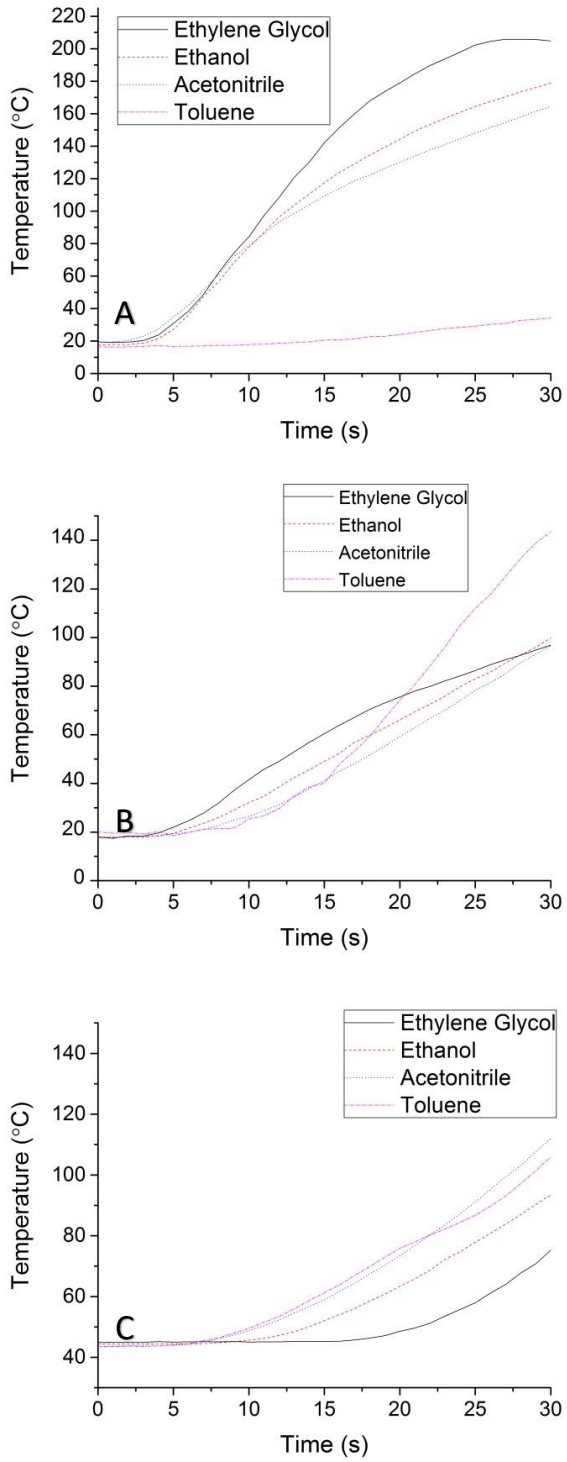

Figure 2.8: Internal heating curves of four different solvents in A) BS, B) SiC, C) Au plated SiC tubes.

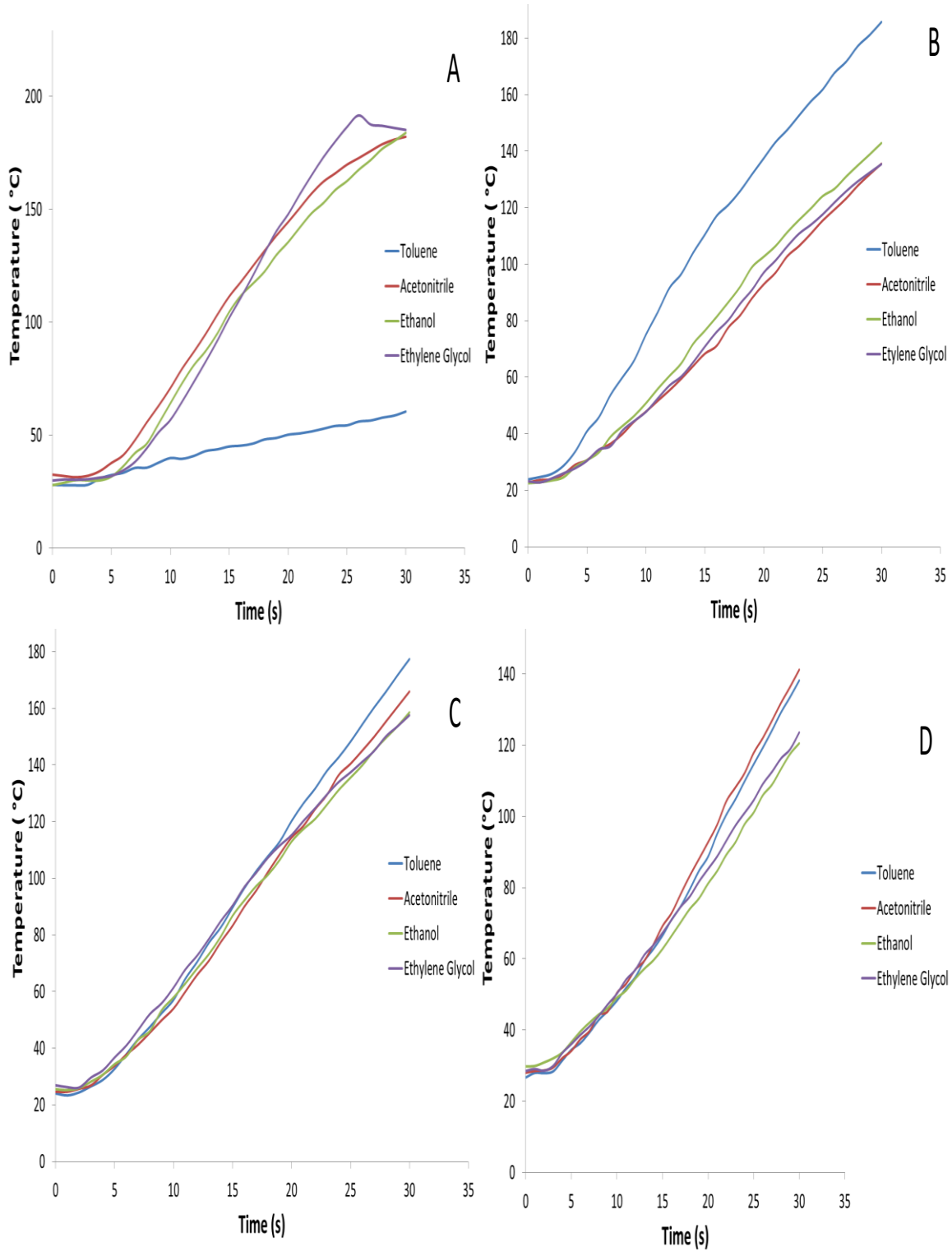

Figure 2.9: IR (external thermometer) heating curves for four different solvents in A) BS vessel, B) SiC vessel, C) Ag plated SiC vessel and D) Au plated SiC vessel.

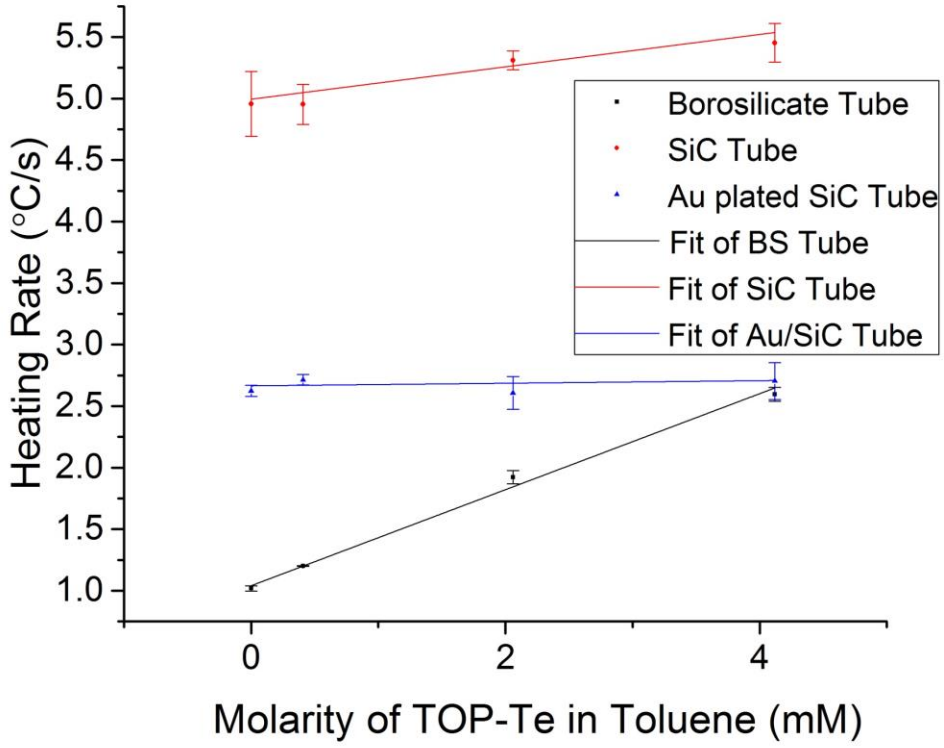

Figure 2.10: Concentration dependent heating rates for TOP-Te in toluene in BS, SiC and Au /SiC reaction vessels.

ethylene glycol (Figure 2.11d) where the rate is invariant with concentration due to the ethylene glycol contributing > 99% of the microwave absorption.

A recent manuscript by de la Hoz confirms the concept that materials that absorb microwave radiation in a non-polar solvent can enhance reaction rates by transferring energy to the reaction solvent.[13,14] In fact, the confusion by many researchers with regards to microwave specific effects likely reflect the difference in solvent usage dominating the reaction conditions leading to the unfortunate controversy with respect to microwave absorption.

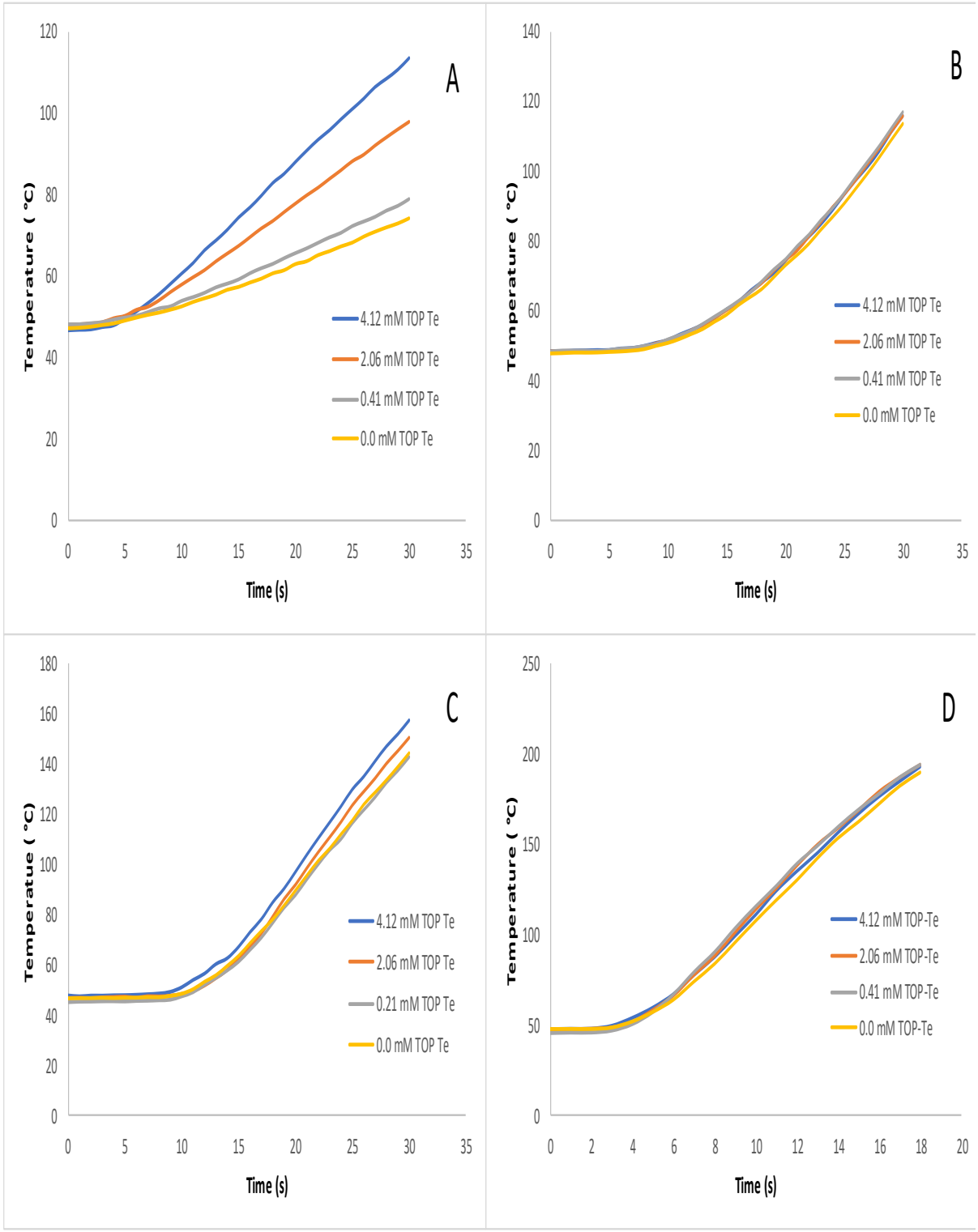

Figure 2.11: Heating curves for four molarities of TOP-Te in toluene in A) BS, B) Au/SiC, C) SiC. D) is the heating curves for four molarities of TOP-Te in ethylene glycol.

2.3.3 Designing a Better Microwave Reaction Vessel

When considering the design of a reaction vessel, in order to ensure the microwave energy is absorbed in the wall of the vessel in order to act as a thermal susceptor in a microwave synthetic experiment, it is imperative to interrogate the power absorbed by the vessel. The absorbed power can be translated to the effect on microwave reaction rates since microwave chemistry is a simple thermodynamics problem, where the rate of the reaction scales with reaction temperature above some critical activation energy producing products. In a microwave the heating rate will depend on the ability to absorb the microwave energy, which is easily understood by considering the fact that the probability of absorption scales as the penetration depth of the microwave energy (D_p), and the thickness of the material being irradiated (x).

$$P_{abs} \propto e^{-x/D_p} \qquad [2.6]$$

The results of the study show definitively that SiC is merely an effective molecular susceptor but is not an effective microwave screener, as the VNA results exhibit a frequency shift that is correlated the tan δ of the internal solvent. For instances requiring EMI shielding or in the discussion of microwave driven chemical reactivity, metal plating is imperative. To achieve the same effect in SiC, the wall thickness would have to be a minimum of five penetration depths (193.0 mm for SiC) to shield the contents from 99% of the impingent microwave radiation. The data demonstrates to completely screen the impingent microwave field, the SiC vessel must by noble metal plated. It is important to note though that for most reactions, the use of SiC vessels represents an important breakthrough pioneered by Anton Parr particularly in cases where microwave absorptivity into the solvent is poor.

2.4 Conclusion

Microwave chemistry suffers from the failure to treat the microwave field as an impinging EMR field by many researchers. The number of publications that confuse microwave absorption with microwave bond cleavage or modifications to reaction pathways that ignore thermodynamics is common place in the field. As discussed widely in the literature and still appearing in the current literature, many studies have indicated enhanced reaction rates in chemical reactions are due to the poorly defined term “microwave specific effects” when in reality the enhancement reflects the solvent absorptivity and thus rate of heating rather than the conversion of microwave absorption into heat. In microwave synthetic chemistry, the possibility of microwave specific effects have led to attempts to separate the interaction of the reaction mixture from the reaction vessel in an attempt to verify that microwave heating leads to accelerated reaction rates following microwave photon absorption. Use of a SiC vessel to remove the potential for solvent or reactant microwave absorption was an important suggestion to be able to understand reaction rates in the microwave, but the lack of a detailed measurement of the amount of microwave leakage in SiC vessels that are 3 mm in wall thickness have generated significant confusion by researchers. The observed transparency observed in the VNA experiment for SiC may impact conclusions with respect to microwave activated processes in microwave chemistry and suggests the results for reaction mechanisms may need to be considered more fully to compare microwave heating to conventional heating.

Dielectric function spectroscopy coupled to theoretical modeling using electrodynamic theories allows the microwave penetration to be properly analyzed providing a strong foundation for understanding the effects of microwave irradiation on synthetic chemistry. The experimental data confirms that in order to eliminate microwave penetration into the reaction system a thin

metal layer must be incorporated. The observed frequency shift in BS and SiC suggests microwave leakage effects in a microwave reaction cannot be ignored when describing reaction mechanisms for microwave chemistry. The observation that parts per thousand concentrations of a strong microwave absorbing reactant such as TOP-Te in a non-absorbing solvent can influence the heating rate has important implications for microwave controlled nanocrystal growth from molecular precursors dissolved in non-microwave absorbing solvents. The results of the study are consistent with earlier report where it was observed that preferential microwave absorption into TOP-X (X= S, Se, or Te) initiates nucleation of the nanocrystal via rapid heating, which leads to controlled growth of the CdX binary semiconductor quantum dot during microwave synthesis. For reactions such as nanocrystal synthesis, where the solvent or molecular precursor exhibit poor microwave cross-section, a microwave susceptor whether molecular or the reaction vessel is required to generate the energy to drive the reaction. While microwave susceptors, highly absorbing vessels, or highly absorbing solvents enhance energy absorption, the thermal transfer is dependent on the solvents' thermal diffusivity. The ability to distinguish between direct microwave interactions with molecules in solution, direct solvent heating, or efficient convective radiative transfer from a reaction vessel in a microwave is important.

CHAPTER 3

MICROWAVE ENHANCEMENT OF AUTOCATALYTIC GROWTH OF NANOMETALS

This data was previously published in "Enhancement of Autocatalytic Growth of Nanometals." *ACS Nano* **2017**, 11 (10), pp 9957–9967 **DOI:** 10.1021/acsnano.7b04040

3.1 Introduction

The early days of nanoscience were focused on developing efficient synthetic methods, including hot injection, microwave, microfluidic, and use of single source precursors.[79] Since then the nanoscience field has matured with a growing focus on understanding the growth mechanisms for nanocrystals and how the reaction can be controlled via heating and precursor addition.[80,81,82,83,84,56] Of the recently developed synthetic tools for reproducible preparation of nanomaterials, microwave heating techniques3-15have been purported to enhance nucleation and growth rates and produce improved material quality in II–VI,[83,84] III–V,[56,85] IV[86] semiconductors, and metals.[87,88,89,13] While there is no doubt of the claims, the rationale for enhancement has not been satisfactorily explained.

In nanometal growth in a microwave, the reported enhanced reactions are poorly understood but clearly must reflect the absorption of the microwave energy to produce heat, which is measurable by dielectric function spectroscopy. There is no possibility that a single microwave photon at 2.45 GHz can initiate a reaction; however, the absorption of the 2.45 GHz photon can produce heat via frictional processes.[63] In addition, the formation of nanometal under identical reaction conditions must follow the well-defined thermodynamic and kinetic models for

nanoparticle growth from a monomer. The growth behavior of Ni and Au nanoparticles grown under mildly reducing conditions in a convective reaction has been fully developed and ascribed to an autocatalytic mechanism.[90,91,92] The autocatalytic mechanism for metal growth, occurs under conditions where a M^0 monomer is formed far below saturation conditions due to a slow kinetic conversion of the metal coordination complex (precursor) to an active monomer step. This leads to a condition where the separation of nucleation and growth occur due to the rate of growth being faster than the rate of nucleation. Turkevich, et al.[92] originally observed this behavior in AuNPs, which led to Finke, et al. proposing an autocatalytic mechanism occurring through a series of steps.[80] More recently the autocatalytic theory was expanded to account for multiple steps in the reaction to explain the narrow size dispersity of materials.[93,94,33] The Finke–Watzky (F-W) mechanism for NP growth assumes activation of the precursor is kinetically slow while growth at a nuclear facet is energetically more favorable than formation of new nuclei. The autocatalytic mechanism is unlike the LaMer classical nucleation theory where super saturation is required to initiate burst nucleation and diffusion limited growth.

Since the earliest report of autocatalytic growth by Turkevich and defined by Finke-Watzky, the autocatalytic mechanism has been validated for several transition metals,[95,96,97] including Ni,[90] and has even been expanded to describe several natural phenomena, including plaque formation in Alzheimer's disease.[96] Measuring the growth kinetics of a nanometal under microwave reaction conditions and correlating the behavior with the predictive autocatalytic models can allow the microwave enhancement to be understood and correlated to observation in convective reactions.

To interrogate the growth mechanism for metal NPs in mildly reducing solvents in a microwave reactor and the influence of the microwave field, the growth of NiNPs, and as a

comparison to literature reported autocatalytic growth for AuNPs,[93,97] is analyzed. While AuNPs are well studied in the field due to plasmonic properties, Ni NPs was chosen as a classical soft magnetic material that mechanistically has been studied in solvothermal reactions[90,98] and is an important material for applications in electromagnetic shielding and catalytic applications.[89] By correlating the microwave power absorbed and the temperature of the reaction it is demonstrated that the microwave-facilitated growth of metal NP follows the F-W autocatalytic model.[80] The data support a model wherein microwave-induced growth enhancement is due to efficient energy coupling to the reactants, and sustained growth is due to microwave absorption into the metal NP as it grows, resulting in uniform nucleation, accelerated NP growth, and thus narrower size dispersities. The results of this study are consistent with recent work by de la Hoz,[13,14] which showed that, for a chemical reaction in the microwave, both the activation energy and microwave absorption are important factors in determining that a reaction performed in a microwave reactor will or will not improve noticeably when compared to a conventional lyothermal reaction. A theoretical framework comparing size and temperature response of metal NPs grown in a 2.45-GHz microwave field can provide a context to understand the growth of nanometals in a microwave cavity.

As part of the study, scaling law behavior for metal NP microwave absorption is developed to elucidate the temperature- and size- dependent permittivity, permeability, and role of potential oxides at the surface on the NiNP during nucleation and growth. The permittivity and permeability data of the isolated Ni nanocrystals support the rapid formation of a native oxide layer (3 monolayers, ~1.2 nm) on the surface following isolation of the Ni from the reaction and not during the reaction. The presence of a stable oxide that rapidly forms after isolation may answer a common question why NiNPs embedded in polymers to enhance EMI

shielding exhibit reduced shielding until the percolation threshold is exceeded. The observation can be explained by the oxide contributions, as the experimental size-dependent dielectric function data suggest that the presence of as little as a monolayer of oxide results in loss of the dielectric function benefits of NiNP inclusion for EMI shielding.[89,99]

Although NiNP and AuNP are the only metal NPs fully explored in this manuscript the insights can be extended to materials grown in a microwave reactor when the precursor activation step is kinetically slow. By carrying out nanometal growth reactions in mildly reducing conditions, control of growth behavior can be achieved through power and concentration even at conditions below supersaturation. The understanding of the microwave growth behavior for a nanometal as merely a thermodynamic and kinetic problem allows the extension of microwave methods to a much wider range of materials without invoking non-thermodynamic effects.

3.2 Experimental

3.2.1 Materials

The NiNP standards, and 15-, 25-, and 40-nm *fcc*-NiNPs were prepared and characterized previously (Figure 3.1),[1] and the 94- and 111-nm NiNPs were synthesized as described below. Nickel acetylacetonate ($Ni(acac)_2$), 70% oleylamine (OAm), and 90% oleic acid (OA) were purchased from Sigma–Aldrich. Paraffin wax and solvents were used without further purification.

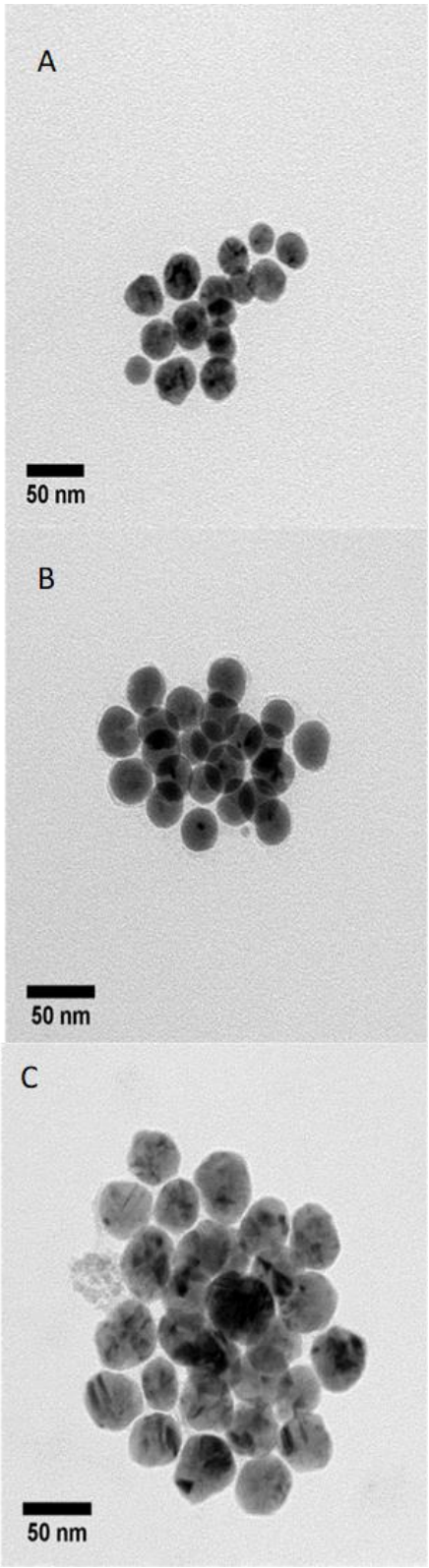

Figure 3.1: TEM of A) 15 nm Ni, B) 25 nm Ni, and C) 40 nm Ni nanoparticles.[1]

3.2.2 Synthesis of Ni standards (94 and 111 nm)

Spherical *fcc*-NiNPs 94 and 111 nm in diameter were synthetically prepared using microwave-assisted decomposition of $Ni(acac)_2$ in a 5:1 OAm-to-OA mole ratio medium. The synthetic preparation of the spherical, 94- (111-) nm *fcc*-Ni was carried out by mixing 3 mmol (6 mmol) of $Ni(acac)_2$, 50 mmol of OAm and 10 mmol of OA in a round-bottom flask and degassing under vacuum at 110 °C. Nine mL of the clear, deep blue solution was transferred under ambient conditions into a G30 (30-mL) Anton Paar microwave vessel and capped. No stir bar or inert atmosphere was used in the reaction vessel. The vessel was placed into the Anton Paar Monowave 300-microwave system and the reaction temperature was ramped to 280 °C at 300-W power, held at 280 °C for 8 min, and cooled by forced air to 55 °C. NPs were isolated from the reaction mixture by magnetic separation from the solution, sonication in 10 mL toluene to re-suspend the Ni, and a second magnetic separation. The resultant solid was dispersed in 10 mL methanol with sonication and magnetically separated. The washing procedure was repeated two more times, then the NPs were dried at room temperature under vacuum.

3.2.3 Synthesis of AuNP

The AuNP were formed by creating a 0.01 M solution of chloroauric acid in 36.8 mL of oleylamine. This solution was heated to 60 °C and degassed under vacuum. For each reaction, 4 mL of the precursor solution was added to a microwave vial with a stir bar. The vials were then placed into a CEM microwave using a frequency of 2.45 GHz at constant power of 150 W to reach varying temperatures ranging between 120 and 150 °C. When the microwave reached temperature, the temperature was held for 1 second, then immediately air cooled to 55 °C.

3.2.4 Characterization

The 94- and 111-nm NiNPs (Figure 3.2) and the AuNPs were fully characterized by pXRD and TEM. The 94- and 111-nm NiNPs can be indexed to the *fcc* structure (card PDF#01-08-7128) measured on a Rigaku DMAX 300 Ultima III Powder X-ray diffractometer (using Cu K_α λ = 1.5418 Å radiation). The AuNPs can be indexed to the *fcc* structure (card PDF#98-000-0056) measured on a Rigaku DMAX 300 Ultima III Powder X-ray diffractometer (using Cu K_α λ = 1.5418 Å radiation). The size, size dispersity and morphology were measured by transmission electron microscopy (TEM) with a JEM-ARM200cF electron microscope at 200-kV accelerating voltage. Diluted NP samples were drop-cast from dispersion in toluene onto 300-mesh copper grids and left to dry under reduced pressure overnight. Histograms generated from image capture of >300 nanocrystals in ImageJ was used to generate the size distribution curves. Solution absorption spectra were obtained using a Varian Cary 50 UV–visible spectrophotometer in a 1-cm quartz cuvette.

3.2.5 Complex Dielectric Function Measurements

Complex dielectric function measurements at 2.45 GHz (298 K) were performed on isolated NiNPs (15, 25, 40, 94 and 111 nm) using a vector network analyzer (Anritsu Lightning E model 37347E) impedance matched to a coaxial cavity manufactured by Damaskos, Inc. (M07T). The measurements were performed on isolated Ni@NiO NPs (15 nm, 25 nm, 40 nm, 94 nm, and 111 nm) blended in a 5% v/v ratio with paraffin wax, and molded into a toroidal shape that fit into the coaxial cavity made by Damaskos, Inc. The Nicholson–Ross–Weir algorithm in the Damaskos software was used to calculate the complex permittivity and permeability of the composites at 2.45 GHz.

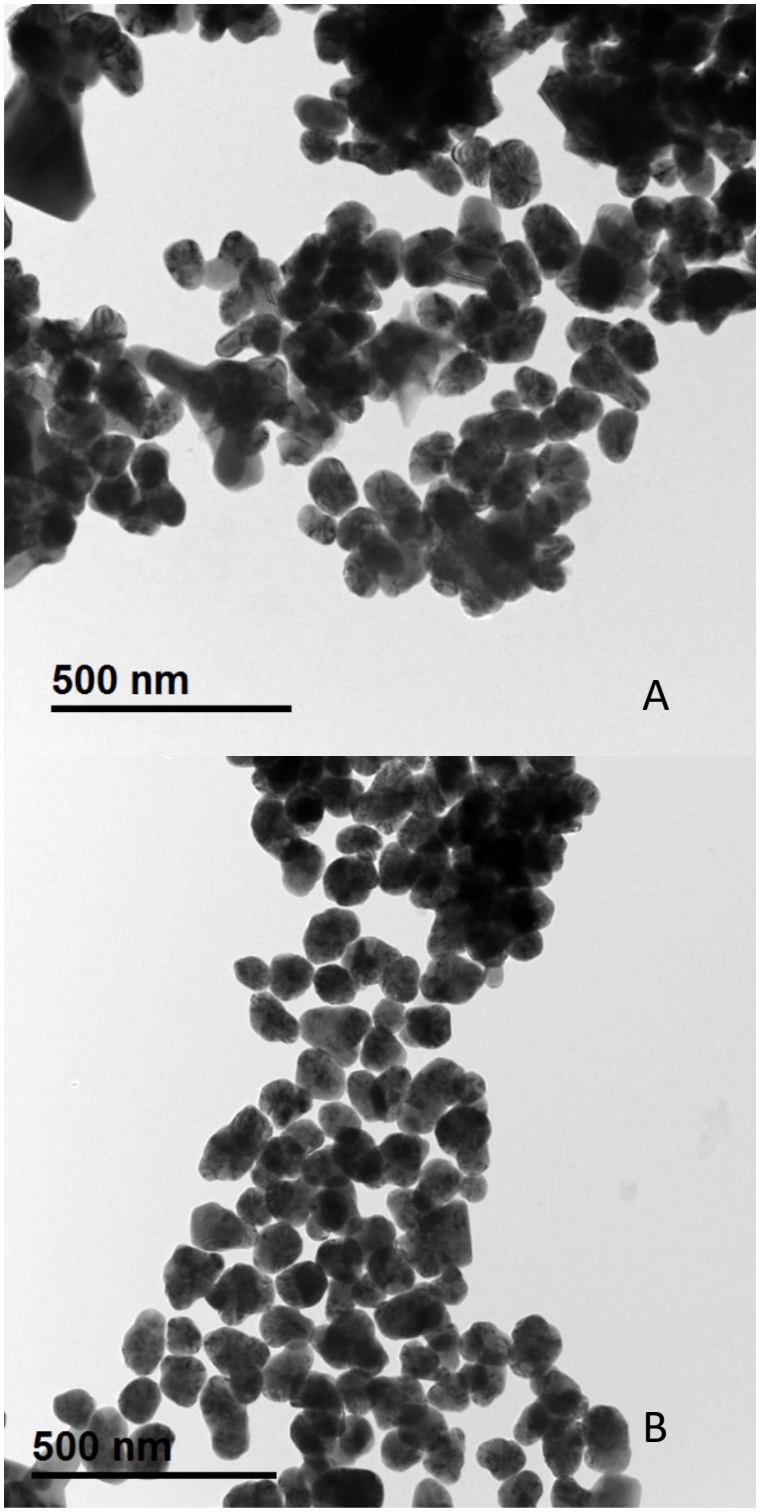

Figure 3.2: TEM of A) 96 nm Ni and B) 111 nm Ni nanoparticles. Histograms generated from image capture of >300 nanocrystals in ImageJ was used to generate the size distribution curves.

To calculate the permittivity and permeability, effective medium theory (EMT) is employed for this calculation. The Maxwell Garnett theorem is ideal for a metallic inclusion in an insulator,[100,101] and is thus the EMT is used for this calculation as well.

3.2.6 Growth Kinetics

The formation rate of NiNPs was monitored under microwave irradiation at 2.45 GHz at 1500 W, 1600 W, and 1700 W using single-wavelength absorption spectroscopy at 488 nm (Ar^+ ion laser). The change in absorption intensity at 488 nm was monitored on a Si diode (ThorLabs DET10A) connected to an oscilloscope (LeCroy WaveRunner 6051) with data points recorded every 2.5 s for 450 s. The measurements were performed on a 0.01 M solution of $Ni(acac)_2$ in OAm. Microwave measurements were performed in a resonant cavity (TE_{013}) coupled to a Gerling microwave source with 10 mL of reaction solution contained in a square (1.4 cm x 1.4 cm) quartz reactor vessel. Figure 3.3 shows the setup. Temperature and power were monitored actively during the reaction. The *in situ* measurement was validated by UV–visible measurements from 400 to 1000 nm at defined time intervals (120 s, 240 s, and final reaction time dependent on power used).

The AuNP reaction dynamics were measured at 2.45 GHz at 150 W in a single mode cavity (CEM). The change in plasmon absorption at 530 nm was monitored by UV-Vis absorption at static time points (0, 81, 101, 110, 126, 139, and 141 s) using separate microwave reaction vessels. To measure the absorption changes, a 0.1 mL aliquot was diluted in toluene. For sizing, TEM images were measured on the AuNPs isolated form he reaction mixture using about 5 mL of toluene and 1 mL of methanol. This process was repeated four times with sonication occurring after each toluene addition.

3.3 Results and Discussion

3.3.1 Size- and Temperature-Dependent Microwave Absorption

During the growth of a metal NP from a molecular precursor the impingent microwave energy is converted into heat through molecular motion driven by dipolar polarization of the solvent and precursors to initiate critical nuclei formation. As the precursor is consumed and the metal NP grows, the dipolar cross-section of the system will evolve. For a metal, microwave coupling also includes ohmic losses, charge separation, and Maxwell–Wagner heating at the solution– metal interface, which enhances the microwave heating. The contribution from the individual components will evolve with the size-dependent metallic properties of the growing metal NP. Additionally, solvent and vessel contributions, which vary with temperature and dielectric function properties, must also be considered.

The complex dielectric function is related to the absorption cross-section or the point at which the amplitude of the impinging microwave field decreases by 1/*e*. The rate of decrease is proportional to the complex permittivity of a material, $\varepsilon^* = \varepsilon' + i\varepsilon''$ and is frequency and temperature dependent. The complex dielectric function includes a term for the ability of a material to store electrical charge—known as the permittivity and represented by ε'—and a term for the combined electronic losses (dipole, ionic, and Maxwell–Wagner) of a material, known as the loss factor, represented by ε''.[16] For simplicity, microwave chemists often use the term tan $\delta = \varepsilon''/\varepsilon'$ because the absorbed power (P_{abs}) $\propto$ tan δ. The rate of growth of the metal NP from the precursor will depend on P_{abs} into the system (microwave cavity, vessel, solvents, and precursors). P_{abs} is related to the complex dielectric function and the heat capacity, such that

$$P_{abs} = M\, C_p \frac{\Delta T}{t} = \frac{1}{2}\omega\varepsilon_0\varepsilon''_{eff}\int_V\left(\vec{E}^* \cdot \vec{E}\right) dV + \frac{1}{2}\omega\mu_0\mu''_{eff}\int_V\left(\vec{B}^* \cdot \vec{B}\right) \quad [3.1]$$

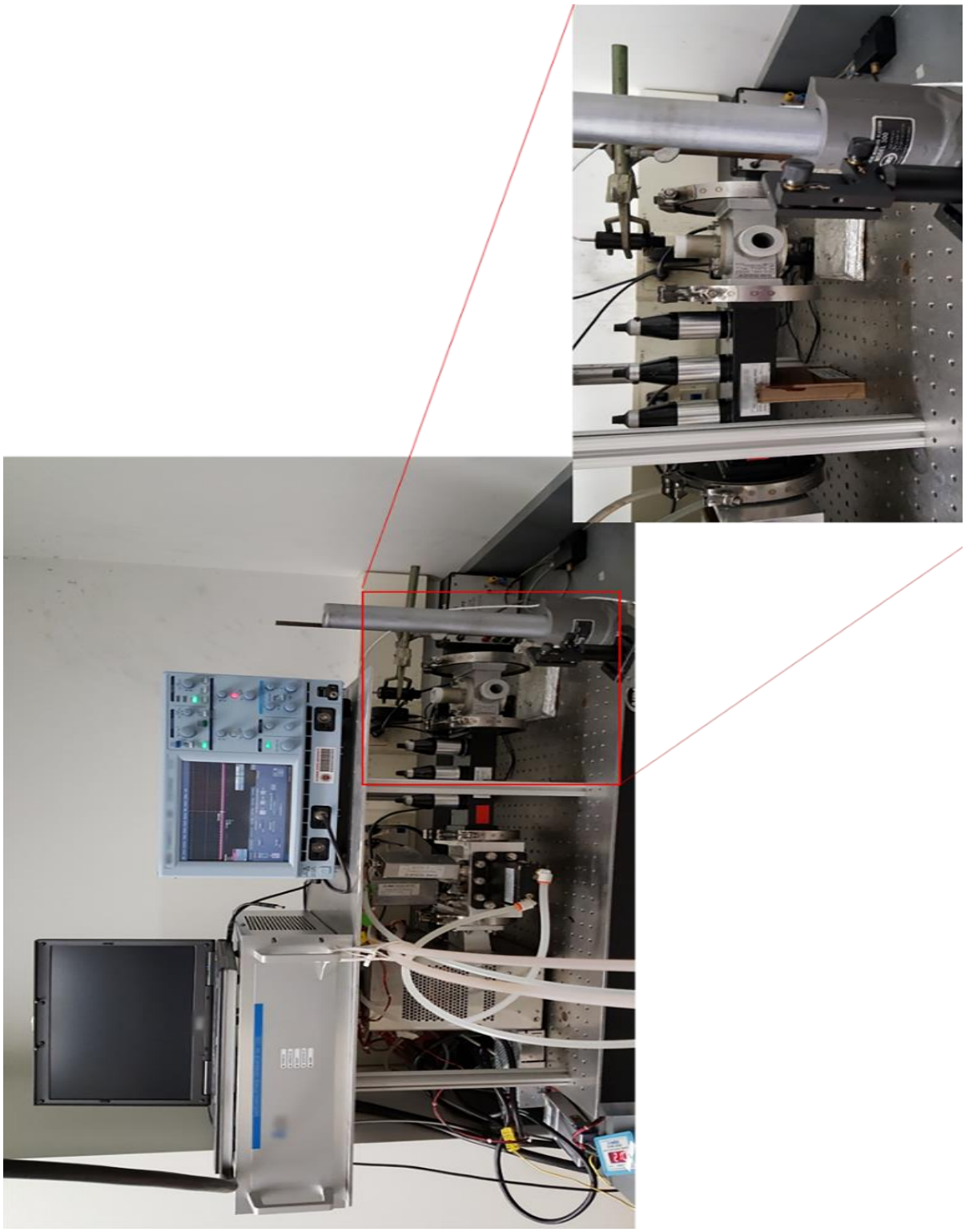

Figure 3.3: Experimental set-up for laser-based absorption measurements during growth of fcc-Ni from NI(acac)$_2$ in oleylamine under continuous MW irradiation (Gerling).

M is the mass, C_p is the specific heat capacity, ΔT is the change in temperature, t is time, ω is frequency, ε_0 is the permittivity of free space, $\varepsilon''_{\text{eff}}$ is the lossy permittivity of the material, μ_0 is the permeability of free space, μ''_{eff} is the lossy permeability of the material, V is volume, $\overrightarrow{E^*}$ is the complex conjugate of the electric field, $\vec{E}$ is the electric field, $\overrightarrow{B^*}$ is the complex conjugate of the magnetic field, and $\vec{B}$ is the magnetic field.

The magnitude of coupling of the impinging microwave photon on a reaction mixture will strongly depend on the electric dipoles of the reaction constituents. Applying the Beer–Lambert assumption in absorption spectroscopy leads to the simple conclusion that the microwave energy is absorbed by the material with the largest ε'' and scattered by the material with the largest ε' term in the system.[16]

P_{abs} for the solvent decreases with increasing reaction temperature, while P_{abs} for the precursor and NiNP will be time dependent as the precursor is consumed and the NiNP grows. As the microwave cross section of the precursor is orders of magnitude lower than for the NiNP, the largest change in microwave absorption will reflect the size-dependent evolution of the NiNP's complex dielectric. To account for the change in microwave absorption a scaling law can be derived by considering the work of Gor'kov and Eliashberg[40,41] and of Marquardt and Nimtz,[42,43] on the size-dependent dynamic electric susceptibility (x_e) of metallic NPs in a microwave field. The early studies demonstrated that the value of ε^* can be described within a quasi-DC quantum model when the size difference between the photons and the NPs is 6–8 orders of magnitude. The complex dielectric function can be written as the Gorkov–Eliashberg equation

$$\varepsilon * = 1 + \frac{m^* k_F (2r)^2}{20\pi^2 a_B} + \frac{139}{1200\,\pi^2 a_B}\left(2 + i\frac{\omega m^* k_F (2r)^3}{6\hbar}\right) \quad [3.2]$$

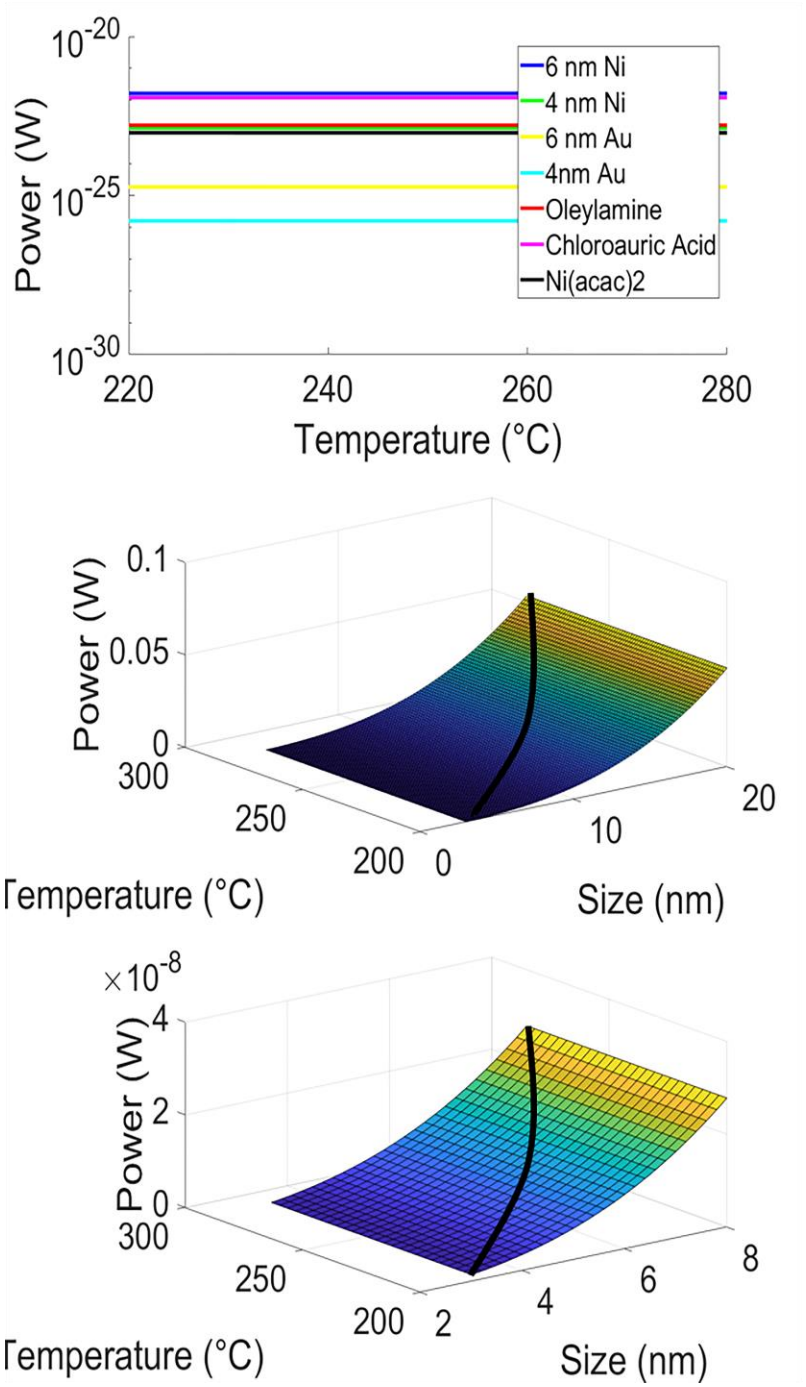

Figure 3.4. A) Theoretical P_{abs} vs. temperature plot for oleylamine (OAm), $Ni(acac)_2$, $HAuCl_4$, 4-nm, and 6-nm NiNP and AuNP based on experimental room temperature dielectric functionmeasurements on neat materials. B) Plot of P_{abs} vs. size and reaction temperature for Ni nanoparticles based on the size- and temperature-dependent change in permittivity (Eqns 3.2 and 3.3). C) Plot of P_{abs} vs size and reaction temperature for Au nanoparticles based on the size- and temperature-dependent change in permittivity (Eqns 3.2 and 3.3). In (B) and (C) the solid line is a guide to eye for the reaction trajectory.

where m^* is the effective electron mass, a_B is the Bohr radius, r is the radius of the NP, ω is the frequency of EM radiation, k_F is the magnitude of the Fermi wave vector, and $\hbar$ is the reduced Plank's constant. The temperature dependency of the dielectric functionconstant can thus be written by coupling the Debye equation[16,25,102] to the Gorkov–Eliashberg equation, such that $\varepsilon^*(T)$ is expressible as

$$\varepsilon^*(T) \cong \varepsilon'_0\left(1+\frac{e^{-2/\Delta T}}{e^{1/\Delta T}+e^{-1/\Delta T}}\right)+i\varepsilon''_0\left(1+\frac{e^{-1/\Delta T}}{e^{1/\Delta T}+e^{-1/\Delta T}}\right) \quad [3.3]$$

A detailed derivation of Eqn 3.3 is provided in Chapter 1. The model predicts that as the metal NP's size and reaction temperature increase, the power absorbed also increases, creating a positive feedback loop of continuously increasing power absorption.

Using Eqns 3.1–3.3, the evolving dielectric functionenvironment that leads to microwave heating can be evaluated in terms of the size and temperature. In Figure 3.4A, the theoretical P_{abs} is compared as a function of temperature for single molecules of oleylamine (OAm), $Ni(acac)_2$, $HAuCl_4$ and single 4- and 6-nm Ni and AuNPs. The 8 nm AuNP and monomers are also plotted in Figure 3.4A for comparison. Using Eqn 3.1, the theoretical P_{abs} is calculated from dielectric functionmeasurements at 2.45 GHz at room temperature on neat material using a vector network analyzer (VNA). Tan δ for OAm is 0.040, for $Ni(acac)_2$ is 0.006, for $HAuCl_4$ is .031, (though this number is complicated by the highly hygroscopic nature of $HAuCl_4$) and the predicted values for 4- and 6-nm Ni and Au are derived using Eqn 3.2. From the tan δ values, the order of P_{abs} will be Ni > OAm >$Ni(acac)_2$ for the neat materials. The same behavior is observed for the AuNPs. This leads to the conclusion that in the formation of NiNPs, during the reaction, the contribution of $Ni(acac)_2$ to microwave absorption is nominal, as at this concentration of $Ni(acac)_2$ (0.15 mmol) to OAm (45 mmol), the microwave power absorbed by $Ni(acac)_2$ will be four orders of magnitude lower than by OAm.

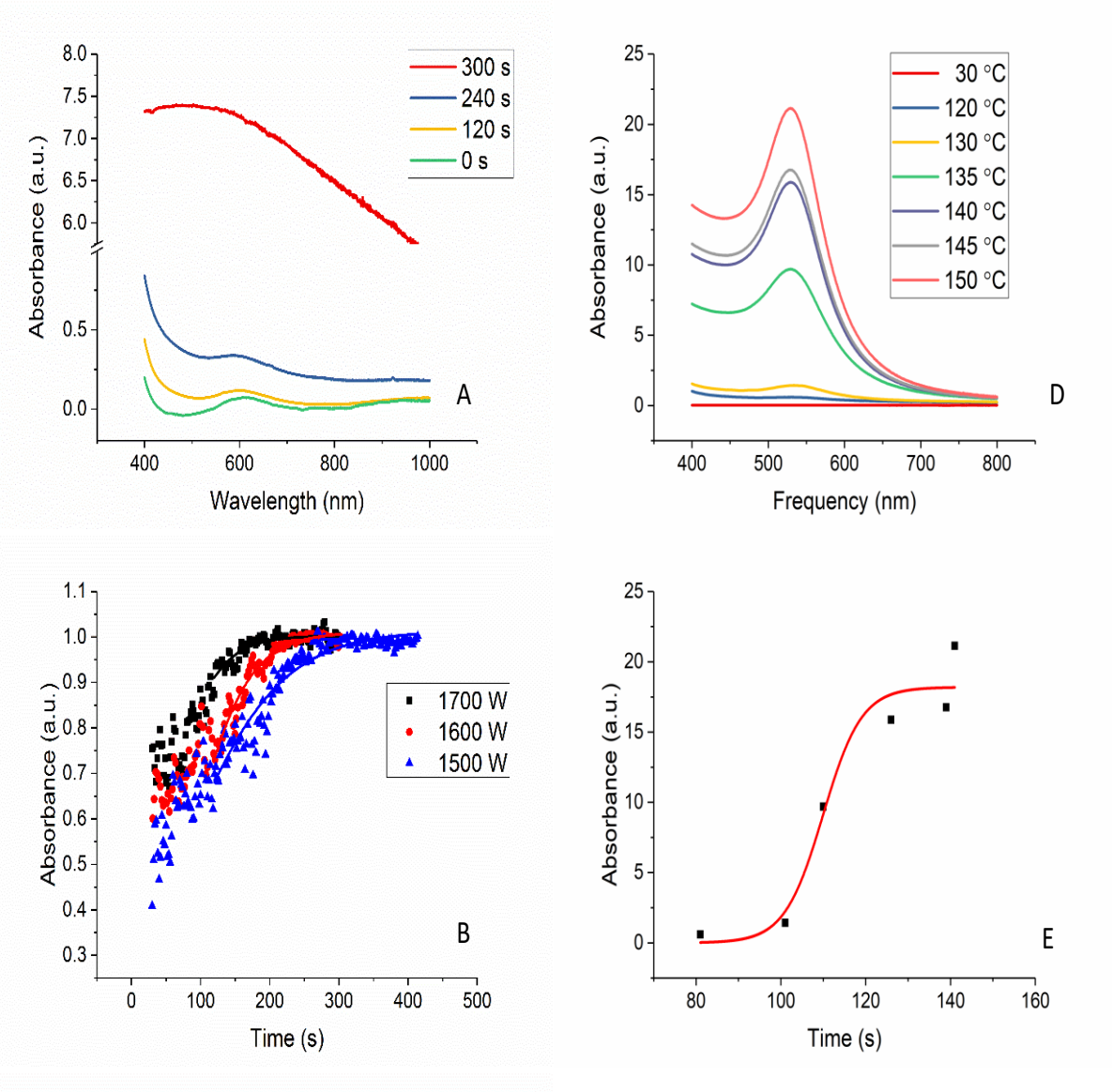

Figure 3.5: Time dependent change in optical absorption of 0.01M $Ni(acac)_2$ irradiated in OAm at 2.45 GHz. A) absorption spectrum at t = 0 s, 120 s, 240 s, and 300 s for 1700-W irradiation, and B) a plot of A_{488} vs time at 1500, 1600, and 1700 W, with a sigmoidal fit and C) a plot of time and temperature at 1500, 1600, and 1700 W. Figures 3.5A-3.5C have an n=3, though error bars are left out for clarity of the figure. Time dependent change in optical absorption of 0.01 M $HAuCl_4$ irradiated in OAm at 2.45 GHz, D) absorption spectrum at t = 0 s, 81 s, 101 s, 110 s, 126 s, 139 s, and 141 s, n=3 E) a plot of A_{530} vs time at 150 W, with a sigmoidal fit, n=1 and F) a plot of time and temperature for AuNP synthesis, n=1.

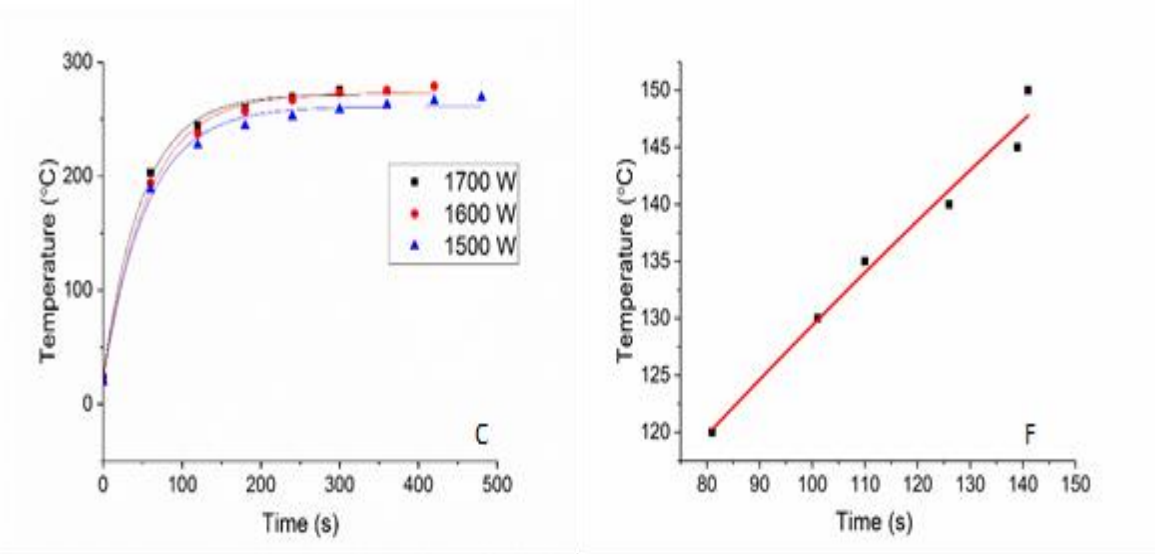

Figure 3.5 continued

The same trend by analogy will be observed for AuNP growth within the microwave field.

As shown in Eqn 3.1–3.3, the cross section for microwave absorption for the metal NP evolves in time as the NP grows and the precursor is depleted. Therefore, as a reaction progresses to completion, microwave absorption is expected to evolve from simple dipolar polarization-driven motion of precursor and solvent molecules to contributions arising from NP absorption and scattering, depending on the material's dielectric.

The predicted heating-vs.-NiNP size correlation is graphed in Figure 3.4B, while the curve for AuNP is plotted in Figure 3.4C. The solid line represents the predicted reaction trajectory assuming normal diffusion controlled growth in both graphs. Inspection of Figure 3.4B confirms that at the temperature of the reaction (280 °C), absorption by the 20-nm NiNP is an order of magnitude larger than by the 3-nm NiNP. For the 8-nm AuNP, the heating curve is steeper than for Ni reflecting the increased ε" contribution to heating as Au increases in size (larger ε" or Au vs. Ni). In addition, the AuNP reaction is held at 150 °C and is not allowed reach

the boiling point of the solvent. Based on the theoretical heat plots in Figures 3.4B and C, the increased dielectric functionabsorption leading to higher reaction temperatures as the metal NP grows may explain the microwave enhanced rates and control observed in microwave-based reactions.

3.3.2 Evidence of Finke–Watzky Growth

The growth of AuNPs under mild reducing conditions was originally described within the autocatalytic mechanism by Turkevich, and theoretically described by Finke and reported by others.[93] The autocatalytic mechanism was extended to explain Ni growth under mildly reducing conditions in organic solvents by Tilley, *et al*.[90] In both cases the autocatalytic growth occurs for reactions performed below supersaturation conditions, wherein burst nucleation cannot occur due to the slow continuous formation of reactive M^0 monomers from M(II) ionic precursors.[103,104, 105] The autocatalytic mechanistic behavior for the growth of metal nanoparticles thus reflects the kinetic barrier for formation of M^0 monomers effectively suppressing nuclei formation.[105,34] The autocatalytic growth mechanism is described effectively as a two-step mechanism with nucleation in step 1, $M^0_{monomoer} \rightarrow M_{crit}$ with a rate of k_1 (M_{crit} is the critical nuclei), followed by the addition of additional monomer to generate a larger nuclei, where $nM^0_{monomoer} + M_{crit} \rightarrow M^*$ with a rate of k_2. The growth to the final NP size occurs by repeating step 2 so that M* represents a continuously evolving larger nuclei. In effect, the final M NP size is achieved by continuous growth from the evolving nuclei once the monomer is depleted, such that $nM^0_{monomoer} + M^* \rightarrow$ M NP. It is worth noting that the autocatalytic mechanism equations are often misinterpreted as formation of two-nuclei due to the nomenclature being erroneously interpreted as new nuclei rather than increasing nuclei size.[17,105,94, 106]

In the autocatalytic mechanism the rate of nucleation (k_1) therefore is slow relative to the rate of growth (k_2) due to the surface energy. Since $k_1 << k_2$, growth from the initially formed nuclei is energetically favored over formation of new nuclei The kinetic slow step is the amine reduction of the metal complex to produce M^0 monomers prior to nucleation of a critical sized cluster.[14,105]

In the nomenclature of the autocatalytic mechanism the ratio of growth to nucleation rates, *i.e.* $k_2[M_{SA}]/k_1$, is defined as the R_{FW}-value, where M_{SA} is the number of surface atoms on the growing nuclei. High R_{FW} values indicate a high level of kinetic control, and at high R-values the reaction produces smaller nanoparticles with a tighter size dispersity, and vice-versa for a low R_{FW}-value. A correlation between k_1 and k_2 can easily be derived from the rate expression expressed at constant temperature with respect to the growing M* (M is Au or Ni)[107]

The rate of formation of d[M NP]/dt can thus be expressed as Eqn 3.4

$$\frac{d}{dt}[\text{M NP}] = -k_1[\text{M salt}] + k_2[\text{M salt}][\text{M}*] \qquad [3.4]$$

while the depletion of monomer ($M^0_{monomer}$/dt) can be expressed as

$$-\frac{d}{dt}[\text{M}^0] = k_1[\text{M salt}] + k_2[\text{M salt}][\text{M}*] \qquad [3.5]$$

In the reaction, it is assumed that the M* concentration is invariant in time ($d[M^*]/dt \sim 0$), and will be equal to the concentration of critical nuclei formed at the nucleation. [M*] during the reaction can be evaluated,

$$[\text{M}^*]_t = \frac{[\text{M salt}]_0 + [\text{M}_{\text{crit}}]_0}{1 + \frac{[\text{M salt}]_0}{[\text{M crit}]_0} e^{-([\text{Msalt}]_0 + [\text{Mcrit}]_0)kt}} \qquad [3.6]$$

Where [M salt] is the concentration of the precursor ($Ni(acac)_2$ or $HAuCl_4$), and $[M_{crit}]_0$ is the critical concentration of nuclei to trigger NP growth. Solving Eqn 3.6 produces a sigmoidal growth curve at large R-values.

By coupling the predictions of Eqns 3.4 and 3.6 to the microwave cross section for a growing metal NP (Figure 3.4), a large value of R_{FW} should arise leading to a narrow dispersity. From the dielectric function arguments, the growth rate will increase as the NP volume increases ($V \propto r^3$) and herefore as P_{abs}, which is proportional to the microwave power and microwave cross section, while the nucleation rate will remain constant at constant temperature or follow an Arrhenius behavior as the reaction temperature increases. It is worth noting that the influence of microwave absorption of energy on the kinetic rates would theoretically continue to enhance the reaction behavior until either all the precursor in the initial solution is consumed or until a steady state is reached at which heat being emitted by the NPs back into the solution is equivalent to the heat being generated by the NP's power absorption.

To test this hypothesis, the growth mechanism for Ni and Au in a microwave cavity is evaluated using absorption spectroscopy to follow the increase in the localized surface plasmon intensity for Ni and Au during microwave irradiation. The Ni absorption was followed in real time, while the AuNP results were analyzed at selected time-points. The NiNP reaction is carried out at 1500, 1600, and 1700 W (2.45 GHz) in a single pass cavity. The Au reactions were carried out at 150 W in a single mode cavity.

Inspection of the absorption properties of $Ni(acac)_2$ and NiNPs in solution reveals that $Ni(acac)_2$ does not absorb at 488 nm, while for the NiNP a strong extinction feature attributable to the localized surface plasmon is observed at 488 nm (Figure 3.5A). The non-overlapping absorption simplifies monitoring of Ni growth, allowing the rate of growth of Ni* (d[Ni]/dt) to be directly monitored by plotting the change in the Ni absorption at 488 nm as a function of time, as absorption intensity will scale linearly with [Ni] following from the Beer–Lambert law.

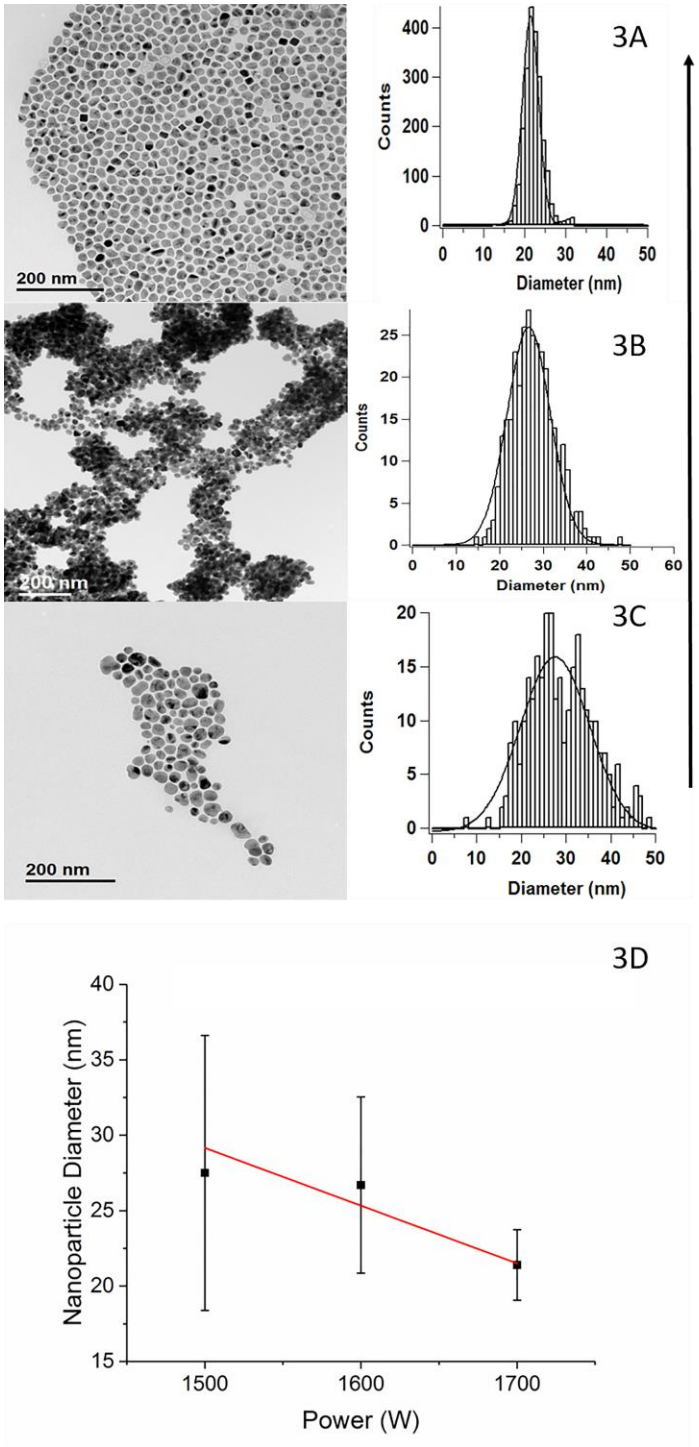

Figure 3.6: TEM of Ni NPs formed at A) 1700 W, B) 1600 W and C) 1500 W with distribution curves of >300 NPs. D) Shows a plot of the average NP diameter formed at each power, with error bars of the FWHM showing that the higher the power, the smaller the NP size and the tighter the distribution

In Figure 3.5A, growth of Ni was monitored by measuring the absorption spectrum with a UV–visible spectrometer at defined time points (0, 120 s, 240 s, and t_∞, where t_∞ is the time point at which all precursor has converted into NiNPs). Each line is the average of 3 runs in the UV-Vis. In Figure 3.5B growth was monitored at 488 nm (A_{488}) during continuous irradiation with absorption data collected every 2.5 s from 0 to t_∞. Each line is the average of three runs in the Gerling, smoothed with boxcar averaging (window of 3). The value of t_∞ varies from 300 to 450 s depending on the power applied. As can be seen in Figure 3.5C, the thermal ramp stabilizes beyond ~120 s. The temperature at each time point at a given power only varied 2-4 °C.

In an effort to baseline the studies to a well-known autocatalytic reaction, the same approach was applied to monitor AuNP growth in a microwave cavity. In Figure 3.5D, the localized surface plasmon for a gold nanoparticle was followed in order to monitor the growth rate of 8 nm AuNP carried out at a maximum temperature of 150 °C at 150 W. The reaction was monitored at fixed time points (0 s, 81 s, 101 s, 110 s, 126 s, 139 s, 141 s) during the growth and the change in the absorption value plotted in Figure 3.5E. The reaction asymptotes after 120 s at a temperature of 140 °C. Unlike the Ni reaction, a single power was carried out (150 W) and the maximum temperature was set at 150 °C thus in Figure 3.5F only the linear region for heating oleylamine is plotted.

To evaluate the correlation of the absorption changes for Ni and AuNPs with $d[M^*]/dt$, it should be remembered the extinction coefficient (ϵ) will follow a simple size-dependent scaling function ($\epsilon \propto r^3$) if the NPs remain spherical. The assumption of near sphericity is confirmed by the TEM data, wherein Ni spheres of ~25 nm (Figure 3.6) and Au spheres of 12 nm (Figure 3.7)

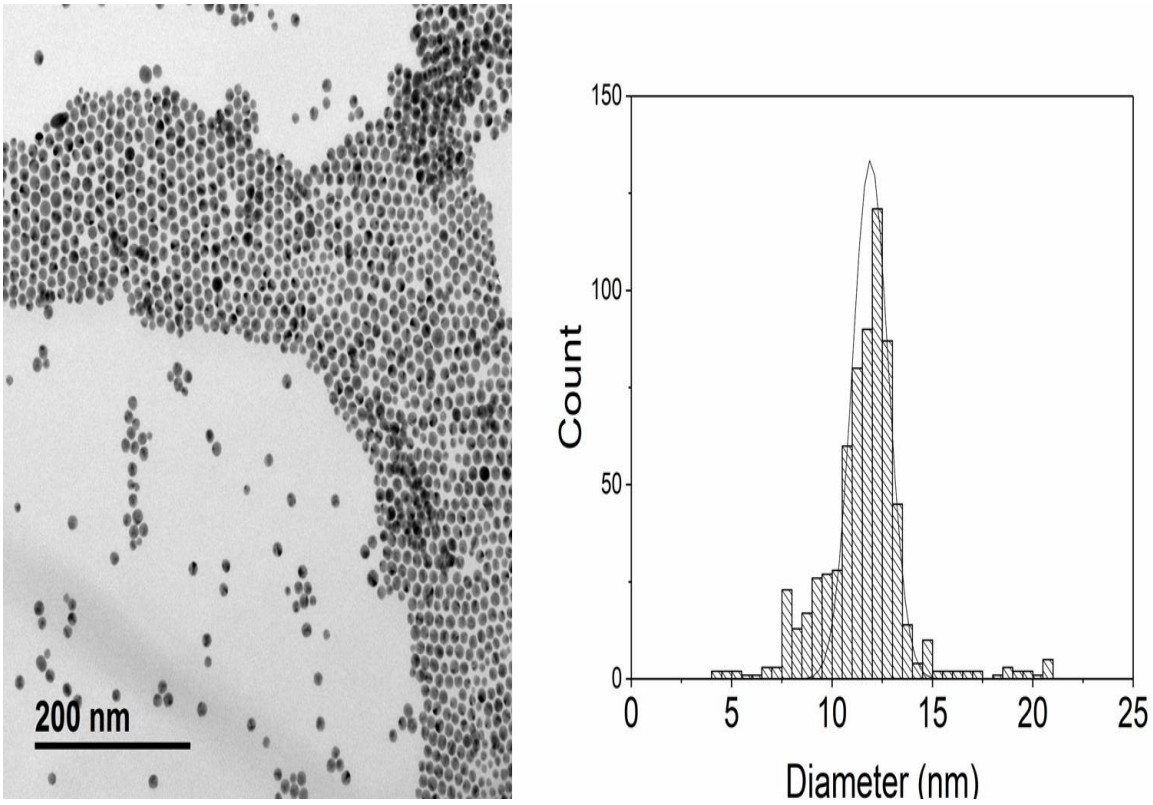

Figure 3.7: TEM of Au NPs formed at 150 W with distribution curves of >300 NPs.

are formed from thermal decomposition at 2.45 GHz. The size-dependent scaling for the absorption behavior for can thus be estimated by considering the Drude model, which predicts that the dielectric function dispersion will scale with the number of metal atoms. For Au, the localized surface plasmon can be effectively followed to monitor the number of AuNPs in solution[108, 109]; however, for Ni which does not exhibit a well-defined plasmon modes, the Ni absorption manifold will show only intensity and not spectral changes.

By using the size-dependent extinction value for Ni, the experimental UV–visible data (Figures 3.5A, 3.8, 3.9) can be fit to the autocatalytic expression (Eqn 3.4), yielding a k_1 value of $2.43\times10^{-5} \pm 2.66\times10^{-5}$ s^{-1} and a k_2 value of $1.20\text{x}10^{-2} \pm 0.006$ $M\cdot s^{-1}$. The reported $k_1 = 1.5 \times 10^{-5} s^{-1}$

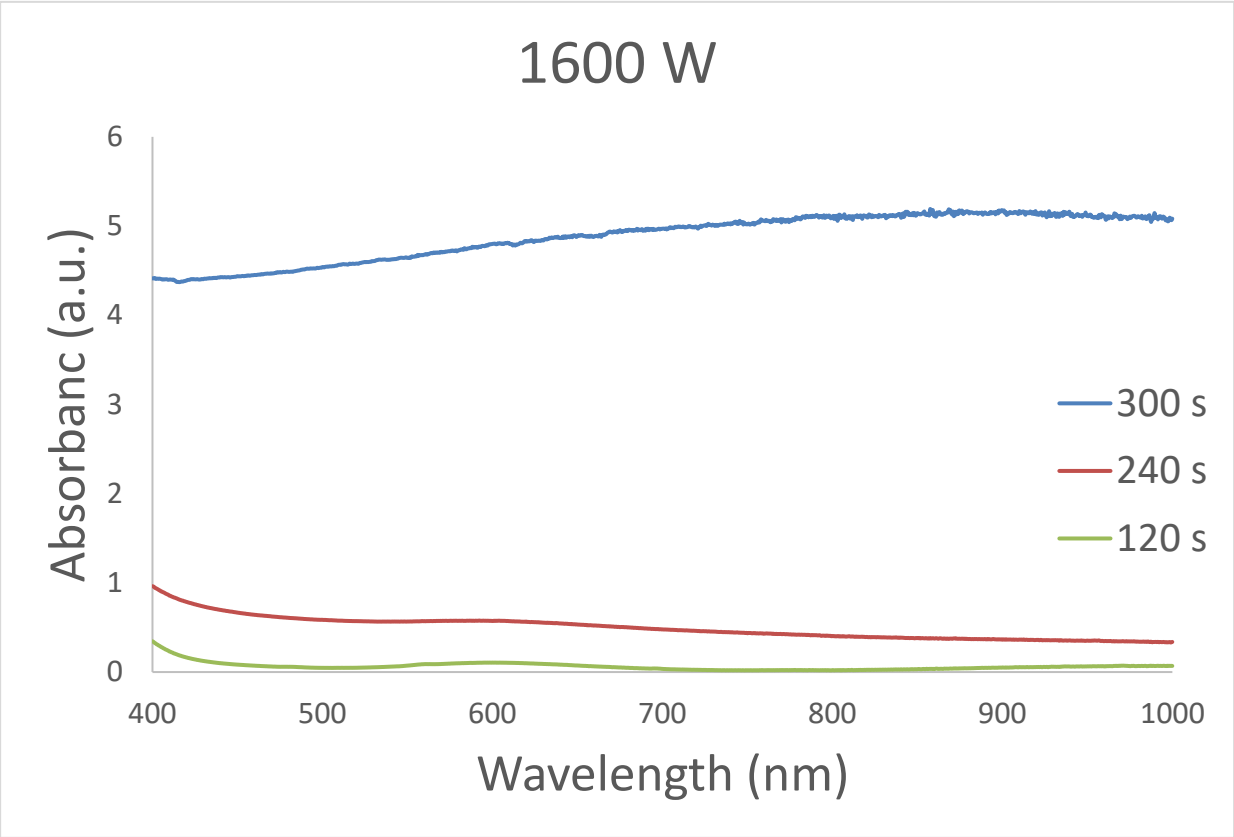

Figure 3.8: UV-vis spectra of 1600 W MW reaction at three time points

and k_2 = 1.1 x 10^{-2} M·$s^{-1}$for Ni grown in the presence of trioctylphosphine at 0.06M $Ni(acac)_2$ in OAm.[90] The value of k_1 is slightly enhanced while k_2 is unchanged, albeit the reaction conditions are different. The experimental UV Vis data for the AuNP (Figure 3.5E) fit to Eqn 3.4 yields values for $k_1 = 1.21\times10^{-5} \pm 1.53\times10^{-6}$ s^{-1} and $k_2 = 0.102 \times10^{-2} \pm 1.53\times10^{-4}$ M·s^{-1}. While no values were reported for AuNPs for $k_1$and k_2, extraction of the values form Liu's results yield rates of k_1 ~ 1 x 10^{-8} s^{-1} and k_2 ~ 1 x 10^{-4} M·s^{-1}.[110] The enhancement in k_1 is notable but requires further investigation to conclusively correlate the rate to the microwave effects.

As expected for an autocatalytic reaction, k_1 (10^{-5} s^{-1}) << k_2 (10^{-2} M·s^{-1}) for the observed metal NP growth. The agreement in the measured and reported kinetic rates for metal NP growth

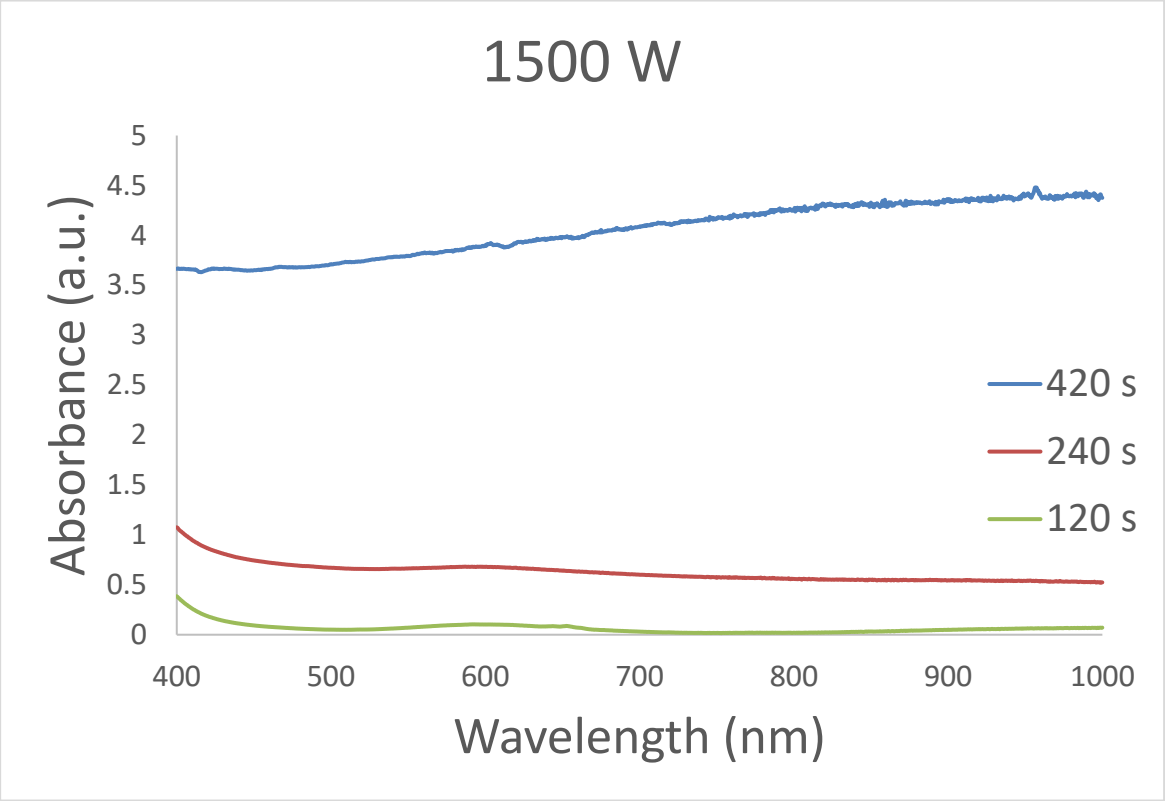

Figure 3.9: UV-vis spectra of 1500 W MW reaction at three time points

in a convective reaction and in a microwave, supports the conclusion that reactions follow the same thermodynamic paths and the observed microwave effects arises from the efficiency of coupling microwave energy to the reaction components to reach reaction temperature, rather than invoking special microwave processes, as suggested in earlier literature.[11]

3.3.3 R_{FW} Values

A notable effect in the microwave is the power dependence of the size dispersion of the Ni (Figure 3.6). The power-dependent Ni sizes at the completion of the reaction are 27.5 ± 9.12 nm at 1500 W, 26.7 ± 5.84 nm at 1600 W, and 21.4 ± 2.33 nm at 1700 W. The TEM distributions observed for the power dependent Ni reactions do not show the typical tailing to

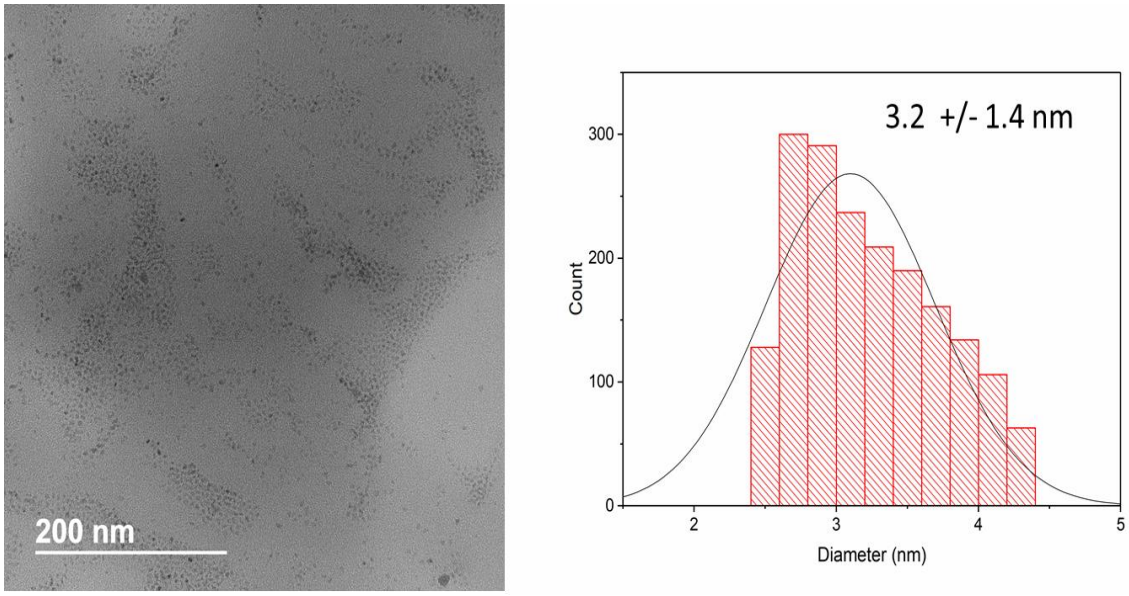

Figure 3.10: TEM of Ni NP at 1500 W after 2 min. The nanoparticles are 3.2 nm in diameter.

smaller sizes observed in Ostwald ripening and exhibit a size distribution much narrower than observed for isolated NiNPs grown *via* hot-injection synthetic methods.[79,56,1,111]

The power dependent enhancement in dispersity for NPs grown in a microwave is readily explained within the F-W autocatalytic mechanism without invoking microwave special effects. In a microwave, higher power will not affect the rates but rather the number of nuclei produced at the initiation of the reaction. In addition, within a microwave cavity nucleation will be uniform since heating is volumetric and does not possess thermal gradients typical of convections reactions.[11,112] Thus, the larger R_{FW} values will lead to better-controlled growth and tighter size distributions.

The assumption that the power dependent narrowing of size dispersity is related to microwave absorption can be demonstrated by calculating the power-dependent R_{FW} value. Finky-Watzke assumed the value of R_{FW} can be approximated from the number of nanoparticles in solution at the end of the reaction since the number of nuclei are invariant during the reaction

allowing $R_{FW} \sim k_2[M_{NP}]/k_1$.[80] A more rigorous calculation would require the number of surface atoms (M_{SA}) to be explicitly known as the NP grows, which is experimentally intractable.

Using the formalism of F-W, for the growth of metal NPs, it is assumed the number of nuclei at the start of the reaction (M*) are equal to the number of nanoparticles at the completion of the reaction (M_{NP}).[80] The nuclei concentration can therefore be calculated from the solution absorption spectrum using the size dependent Mie scattering absorption cross-section of a single nanoparticle.[37,51,52] The calculation of the number of nuclei follows from the methods employed in CdSe QDs and AuNPs. Using Mie scattering to find the size dependent extinction cross-section[51]

$$\sigma_{\text{ext}} = \frac{9V\epsilon_{\text{m}}^{3/2}}{\text{c}} * \frac{\omega\epsilon_2}{[\epsilon_1+2\epsilon_2]^2+(\epsilon_2)^2} \qquad [3.7]$$

Where V is the volume of the nanoparticle, ε_{m} is the dielectric function of the medium, assumed to be invariant with frequency, c is the speed of light, ω is the frequency being absorbed, and ε_{i} and ε_2 are the frequency dependent real and imaginary parts of the dielectric function of the nanoparticle respectively.

We use the extinction cross-section to find the absorption in an equation analogous Beer's Law[52]

$$A = \sigma_{\text{ext}} bN \qquad [3.8]$$

Where b is the path length of the cell, and N is the number of nanoparticles per unit volume.

It is worth noting the F-W reactions are carried out below saturation (LaMer limit) making the estimation of nuclei easier. For the NiNP power dependent study, the calculation yields concentrations of 3.42×10^{-5} M (1500 W); 4.58×10^{-5} M (1600 W); and 1.47×10^{-5} M (1700 W).

The validity of the assumption from F-W that the number of nuclei in the reaction are equivalent to the final NP concentration can be tested by analyzing the number of nuclei at the initiation of the reaction. TEM images of NiNPs 2 min into the reaction (1500 W) are 3 nm in size (Figure 3.10) and as shown in Figure 3.6 reach 27.6 nm. Using the Mie scattering extinction value for a 3 nm Ni, yields a value of 3.2×10^{-5} M for the number of NPs in solution. The value is within experimental agreement with the number of NPs at the completion of the reaction. Such agreement supports the F-W assumption, as this would not be expected in a classical LaMer model where small NPs dissolve to form larger NPs. [106]

From the calculated k_1, k_2, and number of NPs, the power- dependent R_{FW} values for the Ni reactions are 1.02×10^{19} (1500 W), 1.36×10^{19} (1600 W), and 2.04×10^{19} (1700 W). Similarly, the gold nanoparticles grown at 150 W have a concentration of 1.36×10^{-4} M, and yield an R_{FW} value of 6.93×10^{18}. The narrowing of size dispersity observed for the NiNPs with increasing power correlates with the change in NP concentration, and thus the R_{FW} values. In effect, increased power increases the number of nuclei in the reaction due to the more efficient absorption of energy within a microwave cavity where volumetric heating occurs.

3.3.4 Role of Magnetic Moment (Permeability) and Surface Oxides on Microwave Heating

From the above results it is clear the growth of Ni and Au in a microwave follow the expected autocatalytic growth behavior. The improvement of metal NP formation in the microwave, as reflected by the dispersity with increasing power, reflects the more efficient conversion of microwave energy leading to more uniform nuclei formation with a power dependent R_{FW} value and not changes to the reaction mechanism. For completeness of understanding the special effects that might arise for microwave grown materials, the size

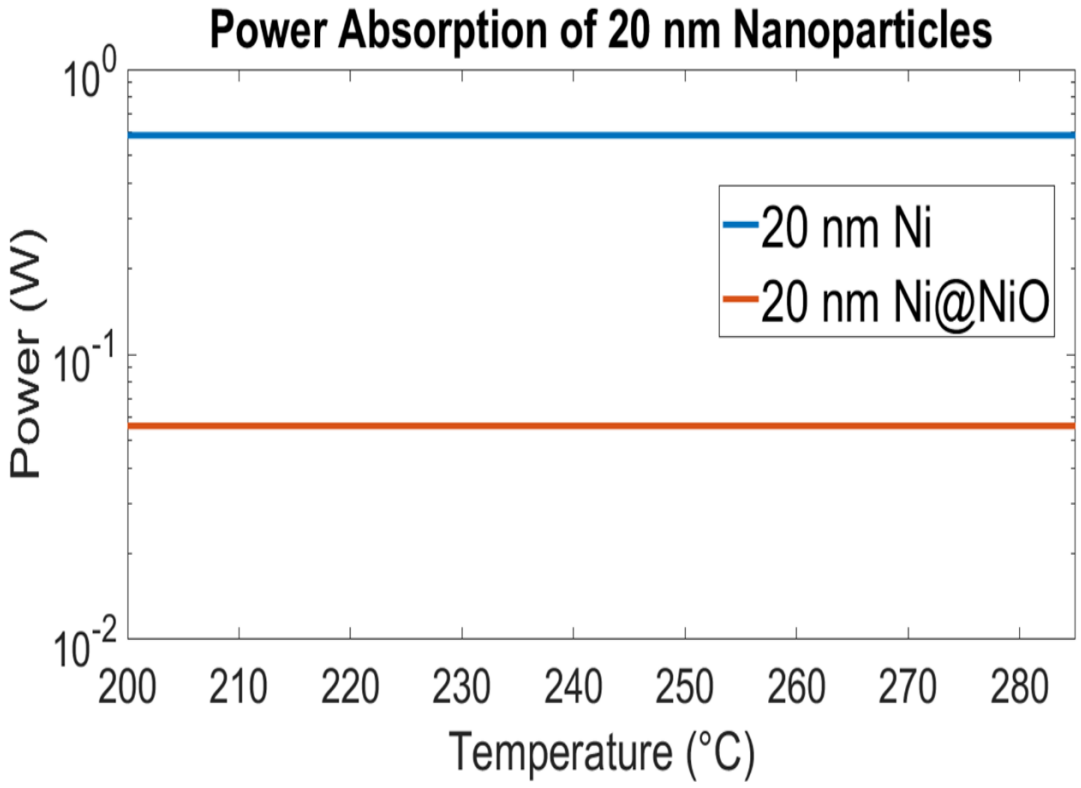

Figure 3.11: Plot of Pavs vs reaction temperature for 20 nm Ni and Ni@NiO nanoparticles based on the size- and temperature- dependent change in permittivity (Eqns 3.2-3.5). Note that the absorption by Ni is an order of magnitude greater than that of Ni@NiO.

dependence of permeability and the presence of a surface oxide forming a core@shell motif should be considered theoretically.

In analogy to the effect of size dependent permittivity on microwave reactions (Eqns 3.1-3.3), the size dependent complex permeability (μ*) can be calculated, although in this study the contribution will be small in the temperature-dependent growth as the magnetic field strength is 1/377 the electric field strength,[113] and the reaction temperatures are well above the blocking temperature for the NiNPs (15 nm super paramagnet limit) in this study.[114,115]

The frequency- and size-dependent permeability can be described by the Landau–Lifshitz–Gilbert expression.[116,117]

$$\mu * = 1 + \frac{(4\pi M_s)^2}{2K - \left(\frac{\omega}{2\pi\gamma}\right)^2 + i\alpha(4\pi M_s)\left(\frac{\omega}{2\pi\gamma}\right)} \quad [3.9]$$

where γ is the gyromagnetic ratio, α is the dampening factor, K is the crystalline anisotropy and M_s is the saturation magnetization. Both K and M_s are size- and shape-dependent, with the size dependency of K written as[23]

$$K = K_v + \frac{6}{x}K_s \quad [3.10]$$

in which K_v is the crystalline anisotropy, K_s is the surface anisotropy and x is the diameter of the NP. The size dependency of M_s is[24]

$$M_{s(nano)} \approx M_{s(bulk)}\left(1 - \frac{2d}{x}\left(1 + \frac{S_{vib}}{3R}\right)\right) \quad [3.11]$$

where $M_{s(bulk)}$ is the bulk magnetic saturation moment, d is average distance between atomic centers, x is the diameter of the NP, S_{vib} is the vibrational melting entropy, and R is the ideal gas constant.

The presence of an oxide forming a core@shell structure will have impact the permeability and the permittivity. In the case of a core@shell NP the change to the permeability effects is proportional to the value of $M_{s(nano)}$. When the shell is antiferromagnetic (AFM), as is the case of NiO, the saturation moment for the core can be redefined as a core@shell moment ($M'_{s(nano)}$)

$$M'_{s(nano)} = \frac{2K}{4\pi H_{ex}} + \frac{J}{x_c H_{ex}} \quad [3.12]$$

where H_{ex} is the exchange bias coercivity, J is the exchange bias constant, K is the core anisotropy, and x_c is the diameter of the core. The effect on the microwave reaction for Ni and Au is insignificant reflecting the reaction temperature, NP size, and magnetic moment of the metal cores.

The effect on permittivity will be more significant though, as an oxide has a much lower dielectric function value, and thus a lower P_{abs}. The effect of a surface oxide is easily seen by considering the size-dependent permittivity for Ni by derivation of the size-dependent complex dielectric function(ε^*) in Eqn. 3.2. The effective ε^* value for a Ni@NiO core@shell NP can be calculated using the Maxwell Garnett effective medium theory, which determines the effective polarizability (α_k), and the Claussius–Mossoti equation, which relates α_k to ε^*_{eff}, such that

$$\varepsilon^*_{eff} = 1 + \frac{\alpha_k}{1 - \alpha_k/3} \quad [3.13]$$

and

$$\alpha_k = 3\frac{(\varepsilon^*_s - 1)(\varepsilon^*_c + 2\varepsilon^*_s) + g(2\varepsilon^*_s + 1)(\varepsilon^*_c - \varepsilon^*_s)}{(\varepsilon^*_s + 2)(\varepsilon^*_c + 2\varepsilon^*_s) + 2g(\varepsilon^*_s - 1)(\varepsilon^*_c - \varepsilon^*_s)} \quad [3.14]$$

where ε^*_s is the dielectric function of the shell, ε^*_c is the dielectric function of the core and g is the radius of the core squared divided by the radius of the NP squared.

From Eqns 3.13–3.14, the impact of a native 1.2 nm oxide on a 20-nm NiNP vs a pure NiNP results in an order of magnitude higher P_{abs} for Ni vs. Ni@NiO (Figure 3.11). Based on the theoretical predictions, the presence of NiO formed during the reaction would effectively slow the heating rate. The effect of oxides on AuNPs is assumed to be minor due to surface passivation, and thus while the equations can be applied to AuNP, it is not considered further in this manuscript to conserve space.

The size dependent behavior for isolated NiNPs embedded in wax can be used to test the predictions in Eqns 3.9–3.14 (Figure 3.12A–B). As one can see, the wax and NiO layers flatten the difference between sizes, but there is a slight rise with size in the dielectric functionand, from 15 to 25 nm, in the permeability. Figure 3.12C–F also shows data with respect to the theoretical permittivity and permeability of NiNPs from 15 to 111 nm with and without an oxide layer without the wax matrix, showing the NiO layer suppresses the permeability and permittivity. For

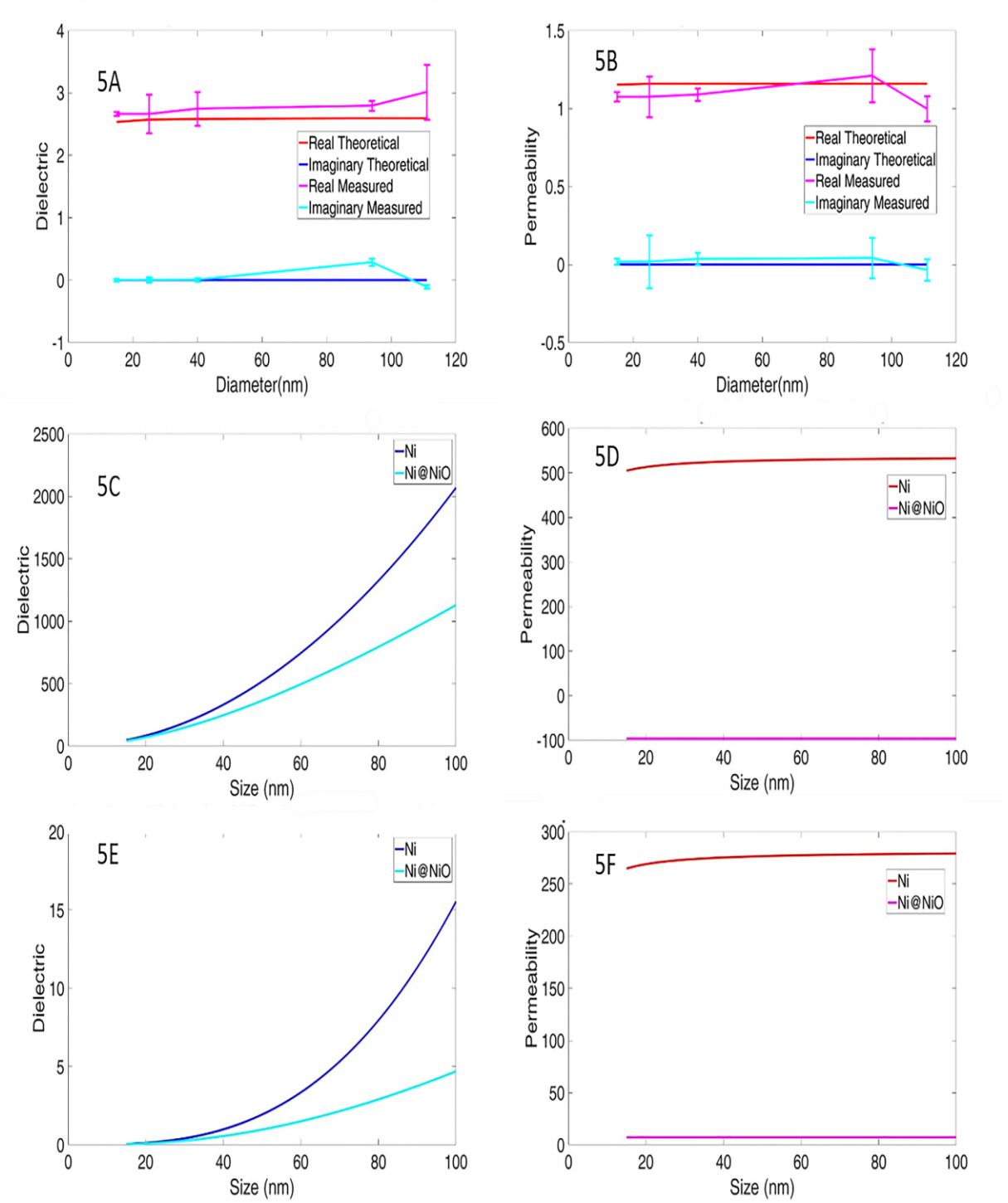

Figure 3.12: A and B) Complex permittivity and permeability of Ni@NiO nanoparticles embedded in wax theoretical compared to measured. *n*=3. C-F) Theoretical complex permittivity and permeability of Ni vs Ni@NiO nanoparticles showing the NiO layer suppresses the dielectric functionand the permeability.

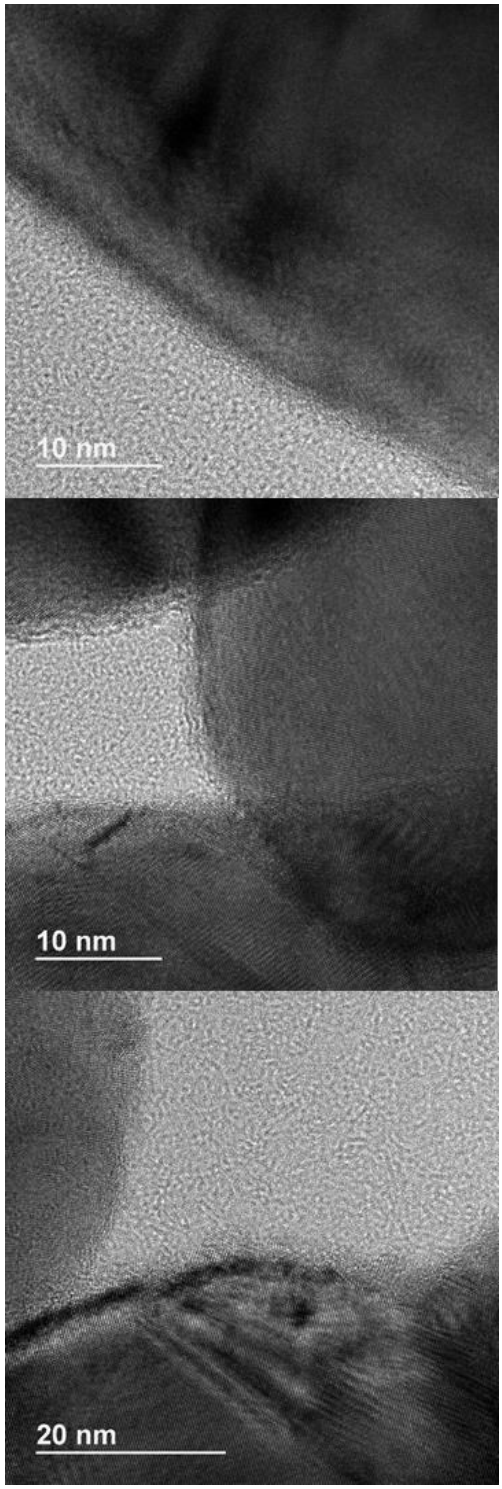

Figure 3.13: High resolution TEM of the 97 and 111 nm Ni NP showing a 1.2 nm oxide layer. The diffraction lines on the edges of the nanoparticles (indicated by red arrows) match to the [110] crystal plane of NiO.

the dielectric function both the real and the imaginary components rise sharply with size, whereas for the permeability, the real and imaginary components reach a maximum just above the single domain size (~20 nm). The NiNPs, as analyzed in the VNA, show that the oxidation layer makes a pronounced difference to the final measured results—once the oxide layer is accounted for, theory and experiment match.

For a microwave reaction, the measurements allow speculation of the impact on a reaction for NiNP growth if an oxide layer is present during the growth step. From TEM images (Figure 3.13), the thickness of the oxide is 1.2 nm, consistent with the reported values. The 1.2 nm oxide layer would lead to a large suppression in ε^* and μ^* accompanied by an order of magnitude suppression of $P_{abs.}$ While it would be exciting to measure the microwave dielectric function spectrum of the NiNPs during growth, the experiment is impractical as *in situ* microwave absorption experiments are difficult due to the difference of 5–6 orders of magnitude between the power needed to induce a microwave-assisted chemical reaction (kW) and the power needed to measure small dielectric function perturbations (microwave) caused by a sample in a field.

3.4 Conclusions

Microwave chemistry has come a long way since the mid twentieth century. Given its potential for green chemistry applications and rapid prototyping of novel materials, a deeper understanding of the exact nature of the evolution of a chemical reaction is desirable. By combining theoretical work with static and dynamic measurements of metal NP synthesis, the enhanced dispersity and growth behavior of metal NPs in a microwave cavity can be understood purely from mechanistic arguments and thermodynamics.

The theoretical work shows that metal NPs will grow until all precursor is consumed, and their final size will then be dependent on the initial concentration of the solution, and the nucleation process. Classical nucleation theory says that the nucleation step is instantaneous, then growth occurs on the nuclei to form NPs. This agrees with the data from the laser absorption and UV–vis experiments, which show the conversion of the precursor into NPs at rates that correspond with the increase in power, lower powers having slower formation times. The laser absorption data also confirm that NPs made in a microwave-assisted reaction follow Finke–Watzky theory, with a sigmoidal dependence of the growth of NPs from solution. The UV–visible data allow us to extract k_1 and k_2 values from the reactions, giving us more insight into the kinetics of the reaction.

The observation that the enhanced reaction rate for a metal grown in a microwave cavity arises from increased microwave interactions with the growing NP may actually provide the thermodynamic basis for the observed improvement in metal NP formation within a microwave reported in Au and Fe/Pt,[87,54] and supports the findings of Liu et.al.[118] for growth of silver NPs in a microwave cavity. Thus the dielectric function arguments leading to microwave enhanced reaction rates can be tied to the autocatalytic process by measuring the rate of reaction as a function of power.

CHAPTER 4

DEPENDENCE OF NANOCRYSTAL GROWTH ON MICROWAVE FREQUENCY AND POWER

4.1 Introduction

There is no doubt that microwave chemistry is a powerful synthetic methodology being employed in organic, peptide, materials, and catalytic chemistry. The observation of accelerated reactions with lower energy demands has led to the argument that microwave chemistry can be a sustainable industrial process. The influence of the microwave on the reaction is still widely debated in various communities. While it has been clearly shown that frequency photons do not possess the energy necessary to cleave even the weakest of chemical bonds,[11,12] several researchers have observed that when a reaction is performed via heating, rather than through convective heat transfer, reaction rates proceed faster than the measured temperature would suggest via the Arrhenius equation.[63] Researchers have rationalized that the accelerated rates arise from the microwave creating a more favorable alignment between molecules leading to an increased dielectric function constant (chaperone effect);[62,119] or potentially due to raising the vibrational energy of the polar molecules thought absorption of the impingent microwave electric field, which Richert referred to as configurational temperature.[72,64,61] Kappe has shown that field density affects formation of Grignard reagents, irrespective of temperature.[120] In II-VI and III-V quantum dots, the effect of microwave power was noted to impact growth rates.[32,59] Vazquez found that higher microwave powers (for the same time) in the synthesis of ZnS nanoparticles resulted in more complete conversion of the precursors, likely resulting from the more rapid decomposition of TTA.[121] In the growth of Ni and Au nanoparticles, the observed rate enhancement was directly

related to the change in absorption cross section as the nanoparticles increases in size, allowing the microwave effect to be understood in terms of the impact on kinetics. Hunt, et. al. demonstrated that the Boudouard reaction has a lower enthalpic energy equilibrium point under heating than under thermal heating, reflecting formation of electron-hole pairs at the surface of the carbon caused by interactions with the radiation.[67]

To understand a microwave reaction, one must consider the effect on thermodynamics and kinetics and how it is correlated to the amount of energy absorbed (P_{abs}). The energy absorbed will produce the latent heat to drive the reaction since $P_{abs} \alpha \Delta T/dt$. In a typical microwave reaction, P_{abs} depends on the applied power at a given frequency for a defined thickness of material. In analogy to absorption spectroscopy in the visible spectrum, it is convenient to define a penetration depth (D_p) for a reaction system, which is defined in terms of the weighted average of the complex dielectrics for the reaction components. For general reactions, the temperature dependent solvent dielectric function defines the P_{abs}, [17, 112,16] although in an nanometal reaction the weighted average will evolve as a function of the temperature dielectric function for the solvent and the size dependent dielectric function of the growing nanometal. Since the dielectric function is frequency dependent, the microwave frequency may also play a role. In gas phase synthesis the role of microwave frequency was observed,[122] but the role of frequency on nanocrystal nucleation and growth in solution has been largely ignored by the microwave chemistry field. The effect on nanocrystal size using different microwave frequencies was investigated by Abe, et al, and no frequency dependence was observed for gold nanoparticles (AuNP) when formed in ethylene glycol (a high microwave absorbing solvent).[123] Intriguingly, though, Abe observed that if oleylamine (a low microwave absorbing solvent) was used no AuNPs were formed at 2.45 GHz (for 60 W power), but were formed at 5.8 GHz.[123] In

CdSe, Massa, et al observed that size and surface morphology were frequency dependent, with 12 GHz producing the largest nanoparticles, and frequencies above and below that producing smaller particles.[124] in $BaTiO_2$, Suib, et al saw that higher frequencies lead to tighter distributions and more spherical particles.[125] In the following manuscript, the influence of both power and frequency on a microwave reaction are explored for the growth of Ni nanoparticles from Ni salts using a mild reducing agent. The growth of the Ni nanoparticles follows an autocatalytic growth mechanism allowing the effect of microwave power and frequency on the kinetics of the reaction to be systematically evaluated. The growth kinetics were followed at three different frequencies (18 GHz, 15.5 GHz, and 2.45 GHz) and three powers chosen to keep the heating rate ($\Delta T/dt$) constant for each reaction. The experimental results clearly show the kinetics for nucleation and growth are enhanced by increasing microwave field strength. The enhanced reaction rate is due to the increased configurational energy of the system consistent with thermodynamic expectations. The observation that both frequency and power define the electric field is expected based upon a simple electromagnetic field absorption argument, and does not require modification of activation energies or pre-exponential factors. The resultant study lays the foundation for further work to allow the translation of traditional round bottom convective reactions to microwave enhanced reactions. Microwave enhanced reactions can allow efficient scale up of synthetic reactions without the complexity of thermal transport in batch reactors.

4.2 Experimental

4.2.1 Materials

Nickel acetylacetonate ($Ni(acac)_2$), 70% oleylamine (OAm), and 90% oleic acid (OA) were purchased from Sigma–Aldrich. Paraffin wax and solvents were used without further purification.

4.2.2 Synthesis of Ni NP

A 7.5 GHz to 18 GHz multimode cavity (16 cm cube) of aluminum with mode stirrer was attached to a IFI Traveling Wave Tube Amplifier 188-500, capable of producing 7.5 to 18 GHz microwave radiation, with a WRD 750 waveguide was used for the 15.5 and 18 GHz synthesis. The TWTA was driven by an Anritsu MG3692C signal generator. The top of the multimode cavity was modified to hold CEM 10-mL tubes and CEM fiber optic thermometer. Additionally, a single mode resonant cavity (TE_{015}) coupled to a Gerling microwave source was used for the 2.45 GHz synthesis

Spherical *fcc*-NiNPs were synthetically prepared using microwave-assisted decomposition of $Ni(acac)_2$ in 0.01 M solution of $Ni(acac)_2$ in OAm. The synthetic preparation of the *fcc*-Ni was carried out by mixing 5.0 mmol of $Ni(acac)_2$ and 500 mL of OAm in a round-bottom flask and degassing under vacuum at 90 °C. Five mL of the clear blue solution was transferred under ambient conditions into a 10-mL borosilicate CEM microwave vessel and capped. No stir bar or inert atmosphere was used in the reaction vessel. The solution was irradiated until 240 °C, 260 °C, 280 °C and until reaction completion in either the TWTA multimode or the Gerling single mode cavity. Temperature and power were monitored actively during the reaction.

4.2.3 Characterization

The NiNPs were fully characterized by pXRD and TEM. The NiNPs can be indexed to the *fcc* structure (card ICSD#98-002-72027) measured on a PanAnalytical Empyeran DY870 Powder X-ray diffractometer (using Cu K_α λ = 1.5418 Å radiation). The size, size dispersity and morphology were measured by transmission electron microscopy (TEM) with a JEM-ARM200cF electron microscope at 200-kV accelerating voltage. Diluted NP samples were drop-cast from dispersion in toluene onto 300-mesh copper grids and left to dry under reduced pressure overnight. Histograms generated from image capture of >300 nanocrystals in ImageJ was used to generate the size distribution curves. Solution absorption spectra used for the growth kinetics were obtained using a Varian Cary 50 UV–visible spectrophotometer in a 1-cm quartz cuvette from 400 to 1000 nm.

4.3 Results and Discussion

4.3.1 Effect of Microwave Frequency and Power

Microwave heating can be classically described in terms of as an alternating EM field passes through a material, any polarizable molecules or particles can couple with the EM field. Preliminary studies suggest microwave frequency and power play a role on nucleation, size, and structural phase.[74-76] The observation is easily understood when considering that in microwave chemistry, the microwave energy is defined by the power and the frequency of the source. The absorption of the microwave field will be dependent on the complex dielectric function $\varepsilon^*(=\varepsilon' - i\varepsilon'')$ which is often expressed in terms of the dielectric function loss function $\tan \delta = \varepsilon''/\varepsilon'$. The P_{abs} will scale with the concentration of molecules in solution that have significant dielectric function loss, and in a dilute reaction can be envisioned as analogous to the absorption of EMR radiation

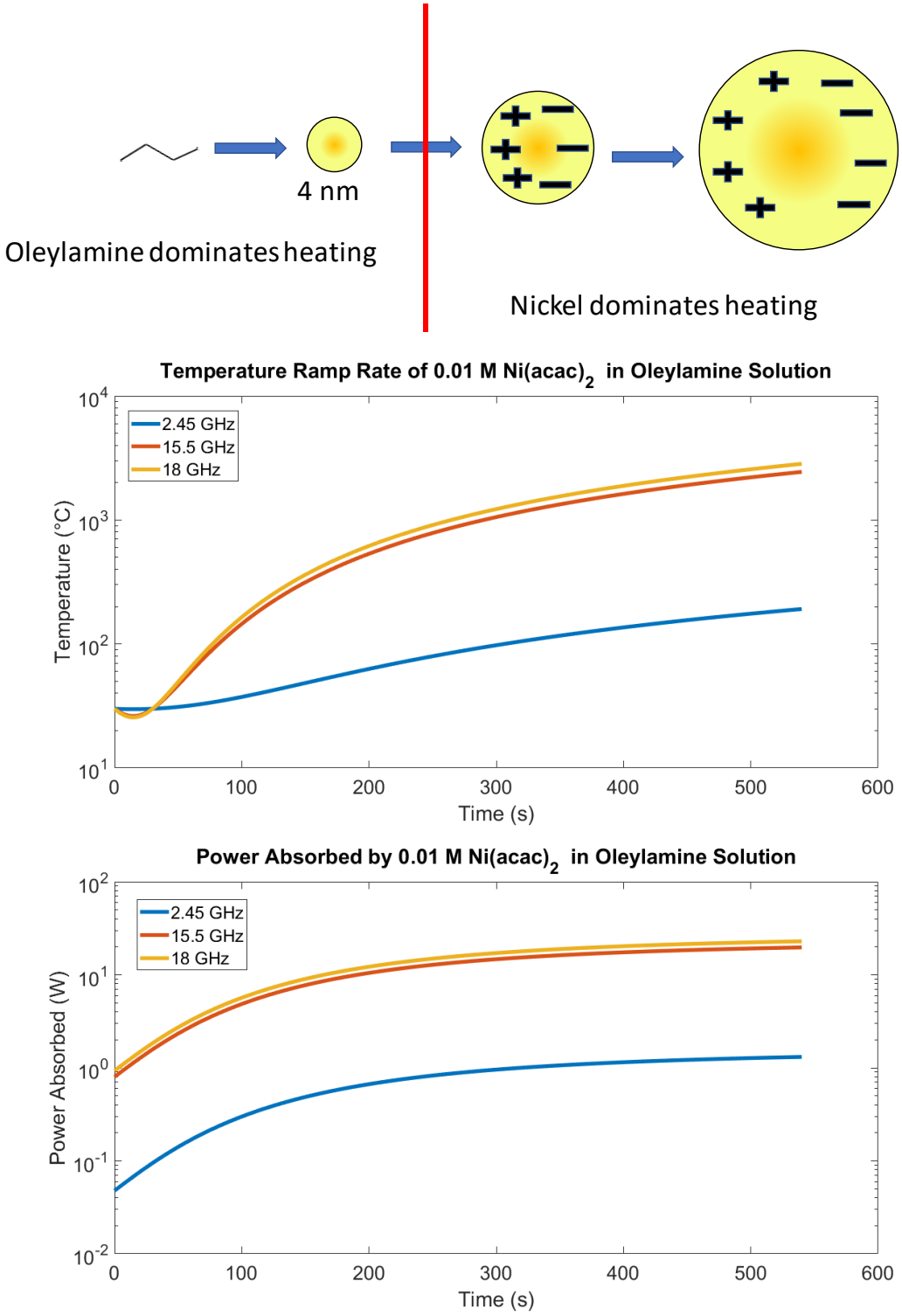

Figure 4.1: A) Illustration of when reaction goes from microwave absorption dominated by oleylamine to nickel nanoparticles. B) Temperature vs. time for reaction at different frequencies, and C) Power absorbed for reaction at different frequencies. B and C both assume a steadily growing nanoparticle.

and will follow Beer–Lambert law behavior. It is important to note that the energy of the photon is not sufficient to break bonds or excite electrons, but rather generates heat by friction as the dipole reorients with the oscillating field. Since each material will have a unique electromagnetic absorption and scattering cross section, a solution or mixture can experience selective heating impacting the rate of heating for a reaction and therefore the overall kinetics.

In the autocatalytic growth of Ni by the mild reduction of $Ni(acac)_2$ with oleylamine (Figure 4.1A), the microwave field is primarily absorbed into the oleylamine early in the reaction and as the reaction progresses, the absorption will become a weighted average of the oleylamine and the size dependent Ni dielectric function value. The increasing absorption of the microwave field by the growing Ni nanometal will give rise to a situation where an elevated configurational energy can arise. Under this condition, one expects an acceleration of the growth rate for the Ni once the Ni nuclei has formed. The ramp rate ($\Delta T/\mathrm{d}t$) for the reaction can be calculated by equating the absorbed microwave power (P_{abs}) to the calorimetric equation

$$P_{\mathrm{abs}} = M \frac{dC_p}{dt} \frac{\Delta T}{dt} = \left(\frac{1}{2}\omega\varepsilon_0 \frac{d\varepsilon''_{\mathrm{eff}}}{dt} \int_V \left(\vec{E}^* \cdot \vec{E}\right) dV\right) \quad [4.1]$$

where M is the mass, C_p is the specific heat capacity, ΔT is the change in temperature, t is time, ω is frequency, ε_0 is the permittivity of free space, $\varepsilon''_{\mathrm{eff}}$ is the lossy permittivity of the material, V is volume, E^* is the complex conjugate of the electric field, and E is the electric field. $\varepsilon''_{\mathrm{eff}}$ is a frequency dependent term. For a metal the dielectric function dispersion generally increases with increasing microwave frequency, and therefore an increase in heating rate is anticipated at higher microwave frequencies. In the case of autocatalytic Ni nanocrystal growth, Eqn 4.1–4.2 can be used to predict the reaction temperature and absorbed energy as a function of frequency

Table 4.1: The dielectric function loss for the reaction precursors at the three microwave frequencies used in the experiments. The * denotes calculated values.

	2.45 GHz	15.5 GHz	18 GHz
Oleylamine[128]	0.102±.011	0.207±.008	0.238±0.014
$Ni(acac)_2$[128]	0.001±.004	0.012±0.010	0.011±0.009
Ni (4 nm)[128]	0.010*	0.063*	0.073*
Ni (6 nm)[128]	0.034*	0.212*	0.247*

with respect to the changing size dependent dielectric function of the Ni NP growing with time, and the evolving heat capacity of the system.[16,20,21]

$$\varepsilon * \ = 1 + \frac{m^* k_F (2r)^2}{20\pi^2 a_B} + \ \frac{139}{1200\,\pi^2 a_B}\left(2 + i\frac{\omega m^* k_F (2r)^3}{6\hbar}\right) \qquad [4.2]$$

Figure 4.1 assumes a constant electric field (E_0) throughout the reaction. The dip in the temperature plot (Figure 4.1B) arises from the change in heat capacity for oleylamine with increasing temperature prior to growth of the Ni nanocrystals to a size regime where microwave absorption begins to play a substantive role. The dielectric function loss values for the reaction components used in Eqn 4.1 are extracted experimentally using a vector network analyzer (VNA) and are listed in Table 4.1. From the ε'' values, the order of P_{abs} will be Ni > OAm >$Ni(acac)_2$ for the neat materials. Using the values in Table 4.1, a theoretical plot of P_{abs} (Figure 4.1C) can be generated to predict the effective evolution of microwave absorption with growing Ni size and decreasing C_p for the solvent. Inspection of Figure 4.1B and C leads to the observation that, during the reaction, oleylamine will dominate the heating profile initially until

the Ni nanoparticle grow to sizes > 4nm. At this point the microwave absorption will steadily shift from oleylamine to Ni nanocrystal as the weighted average of oleylamine absorption and absorption by the Ni, which scales with size and concertation.

The initial step in the autocatalytic reaction (formation of Ni^0 precursors and initial nuclei formation governed by k_1) will follow classical Arrhenius law behavior ($k = Ae^{Ea}/_{RT}$).[126,127] The second step (k_2) is defined by the growing nucleus and also will be governed by Arrhenius law.[126,127] In both cases the rates will follow exponential behavior. In the autocatalytic mechanism the ratio of $k_2[Ni^0]/k_1$ is defined as the R-factor and dictates the size distribution. By assuming the reaction Arrhenius law behavior, it can therefore be anticipated that a significant acceleration of reaction rate will occur due to more efficient heating. In effect, carrying out the microwave growth of a material that follows autocatalytic growth at higher frequency should lead to faster reaction times, smaller nanocrystals, and tighter size dispersions based upon the autocatalytic growth R_{FW} value, which was previously reported to follow the empirical law for size y = -0.0026(x) + 26.4 (x = power applied, y = size) and for distribution y = -0.034(x) + 60.1 (x = power applied, y = dispersion).[128]

4.3.2 Frequency Dependent Growth of Ni

The frequency dependent effects on reaction rate and nanoparticle properties were tested for growth of Ni nanocrystal under mild reducing conditions. The Ni reactions are performed using 5 mL of 0.01 M $Ni(acac)_2$ in oleylamine solution in a microwave cavity operating at constant power to ensure constant heating rates $\Delta T/dt$ of 9 min, 4 min and 2.5 min) at 2.45 GHz (140 W, 148 W, and 160 W), 15.5 GHz (138 W, 174 W, and 232 W), and 18 GHz (91 W, 123 W, 151 W). The size and size dispersity of the Ni nanocrystals extracted from TEM

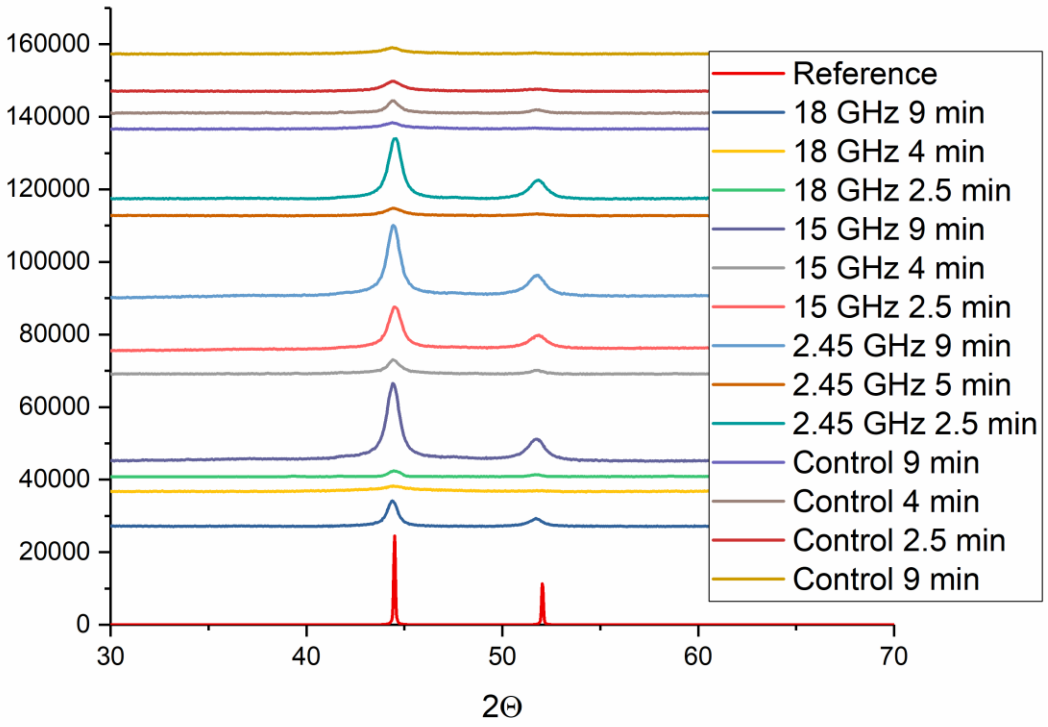

Figure 4.2: pXRD of fcc-nickel nanoparticles

measurements for each reaction condition is shown in Figure 4.2 and summarized in Table 4.2. Powder X-ray diffraction of the samples is detailed in Figure 4.2 and confirm the isolation of *fcc*-Ni in all reactions. The rate of formation of the Ni by consumption of $Ni(acac)_2$ is monitored using UV-Vis absorption spectroscopy at fixed time points to follow the increase in Ni dielectric function absorption, which is broad and featureless, and the loss of the $Ni(acac)_2$ absorptions at 610 nm and a rising absorption above 420 nm (Figure 4.4). As shown in Figure 4.1, the theoretical change in absorption of the microwave field from 2.45 GHz to 18 GHz should increase by two orders of magnitude leading to more rapid heating. Consistent with this, a plot of the frequency dependence vs size in Figure 4.5A, reveals that for each frequency the size decreased and the size dispersion narrowed as the power increased. However, there is no

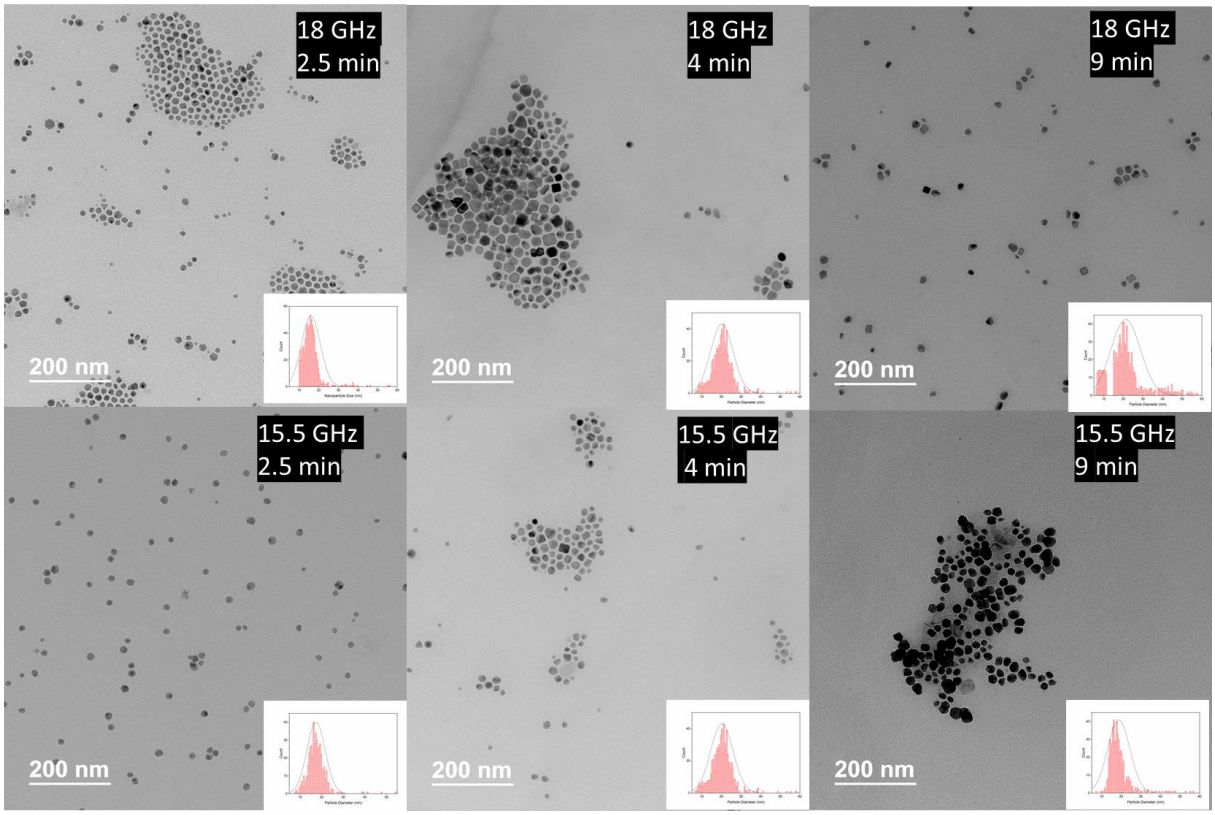

Figure 4.3: TEMs of the nanoparticles formed in the MW at 18, 15.5, 2.45 GHz, and control experiments. Histograms are based on >300 particles.

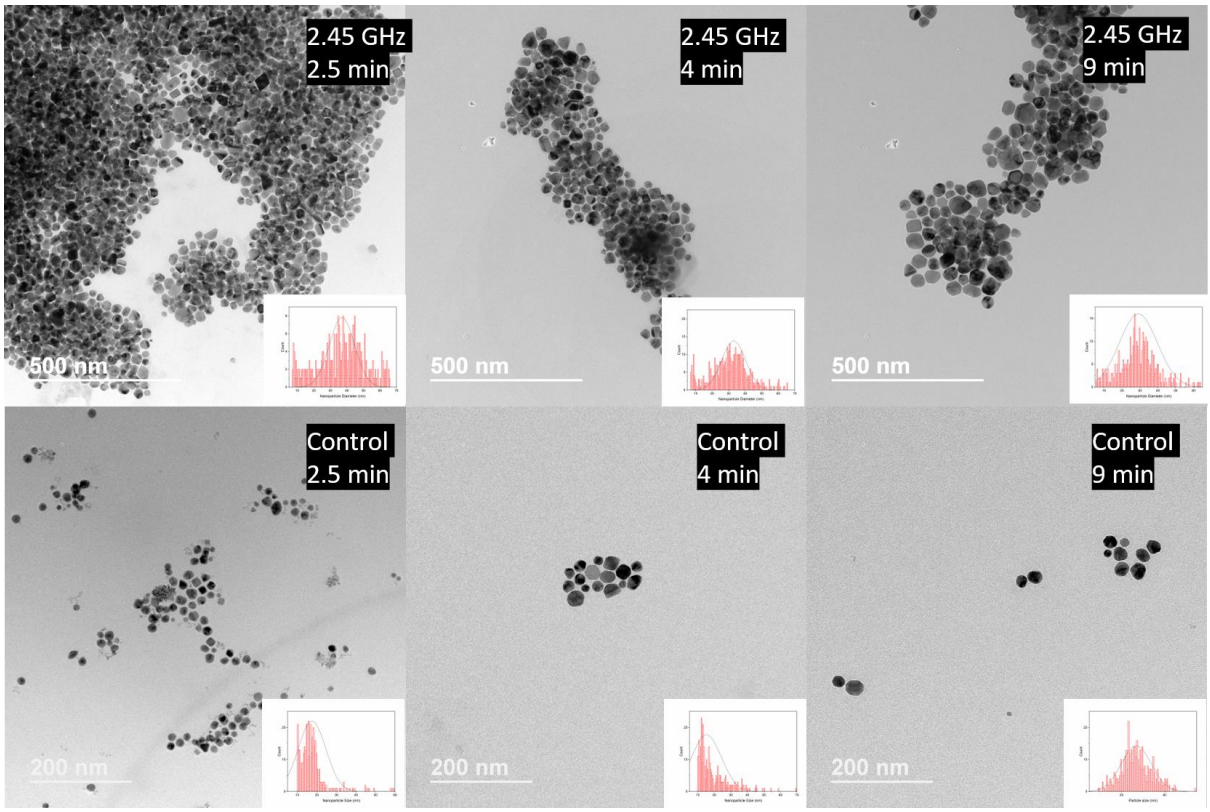

Figure 4.3 continued

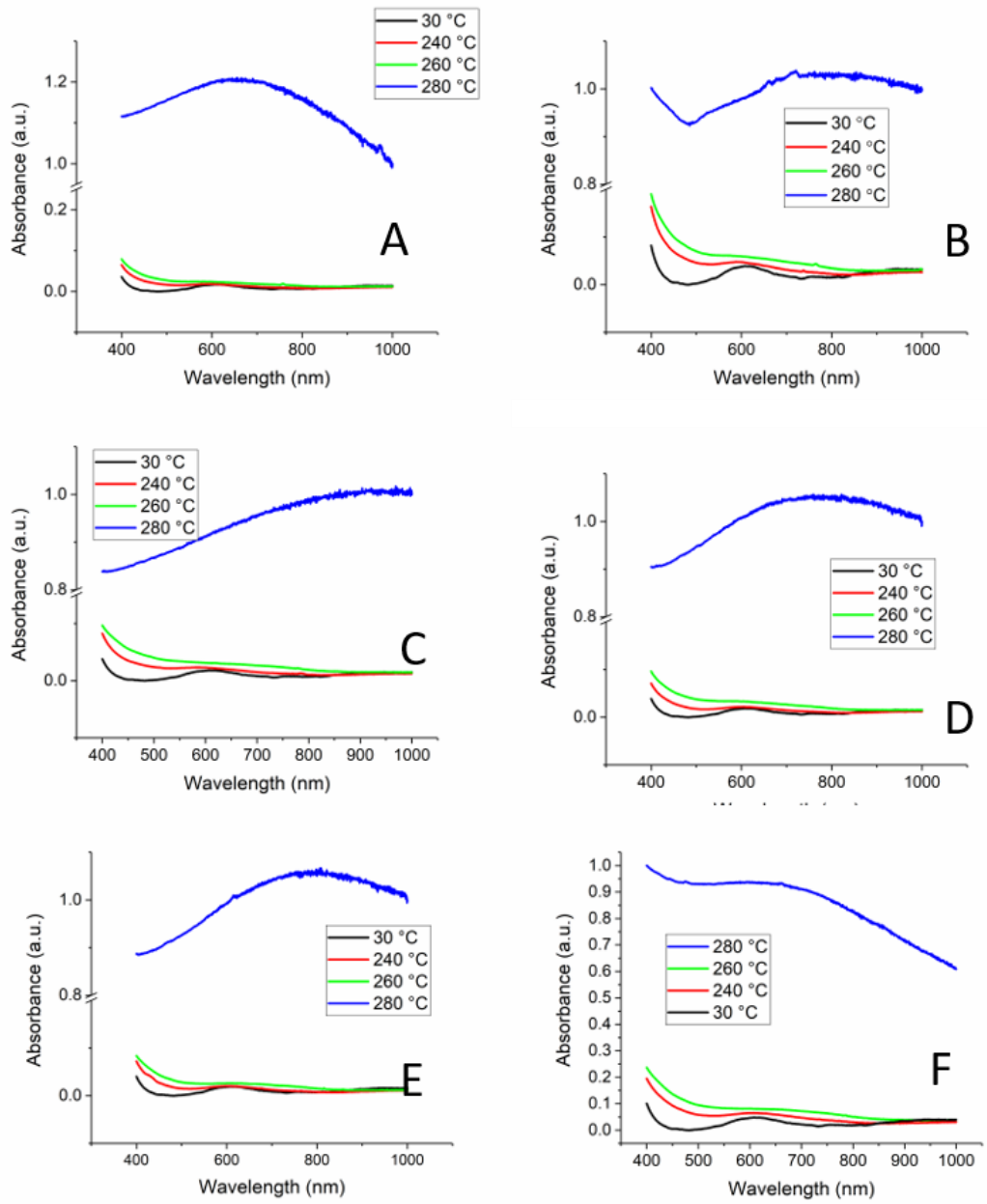

Figure 4.4: UV-Vis spectra for all experiments A) 18 GHz 2.5 min, B) 18 GHz 4 min C) 18 GHz 9 min; D) 15.5 GHz 2. 5 min, E) 15.5 GHz 4 min, F) 15.5 GHz 9 min; G) 2.45 GHz 2.5 min, H) 2.45 GHz 4 min, I) 2.45 GHz 9 min; J) Control 9 min, K) Control 4 min, L) Control 2.5 min. N = 2 for all.

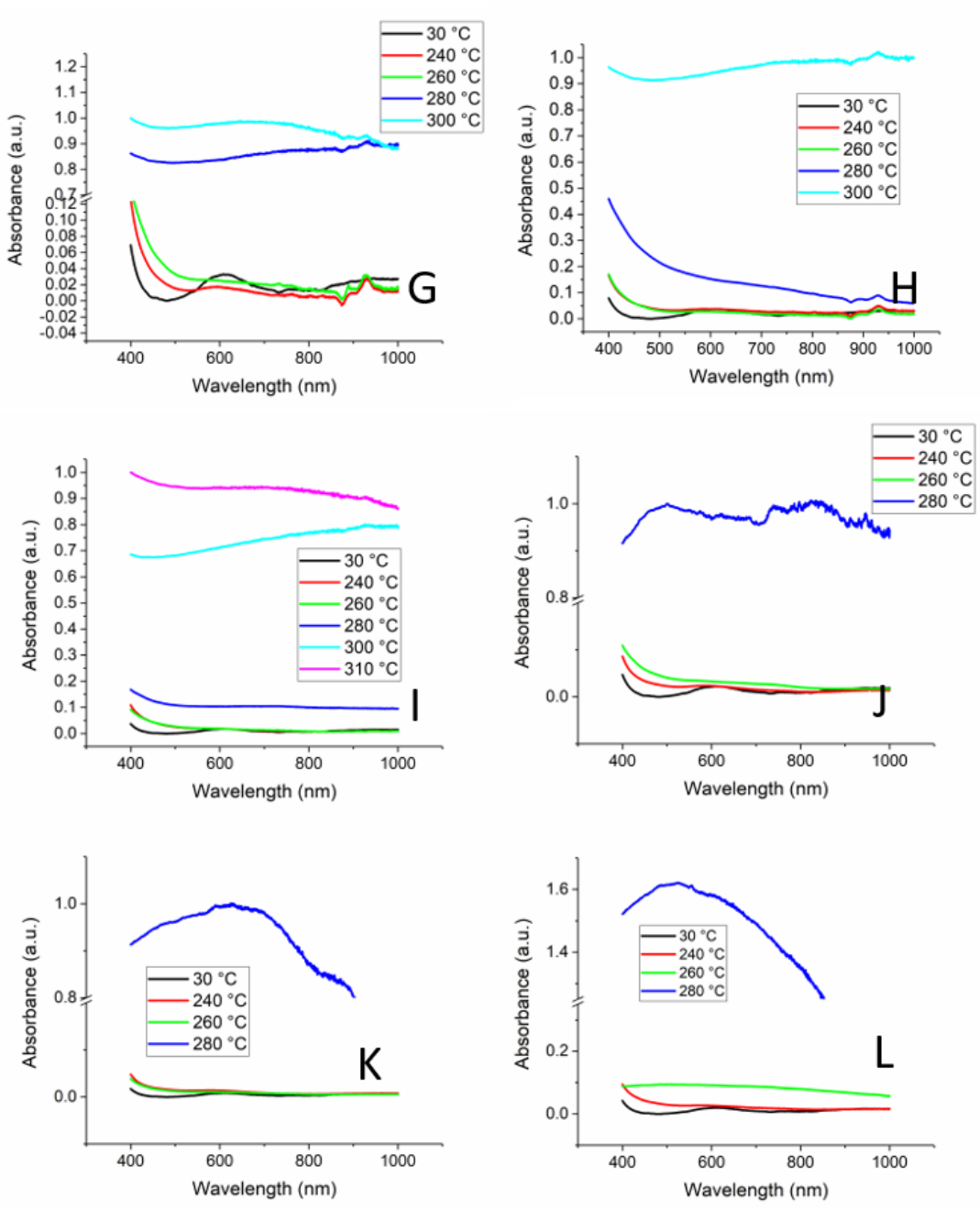

Figure 4.4 continued.

immediately apparent correlation between size and frequency, suggesting the complexity requires analysis of the frequency dependent effects on the kinetic steps of the autocatalytic mechanism.

Evaluation of the frequency dependence on the reaction mechanism rate for Ni formation (d[NP]/*d*t) can be accomplished by plotting the change in absorption intensity at 488 nm, where no $Ni(acac)_2$ absorption exists and as shown previously corresponds to absorption by only the Ni nanocrystal, and extracting the values for k_1 (nucleation) and k_2 (nuclei growth) from the kinetics plot.[128,90] The change in absorption vs. time for the Ni growth can be fit using the Finke-Watzky (F-W) autocatalytic mechanism,[80,128] which states that for transition metals in a weak reducing environment, there is a slow nucleation step whose rate (k_1) is dependent on the slow reduction of Ni^0 monomers form the Ni salt, followed by a rapid, self-catalyzed nanoparticle growth step characterized by k_2. Unlike an Ostwald mechanism, in the autocatalytic mechanism the metal monomer M^0 concentration is below saturation, the number nuclei formed at the start of the reaction is invariant over the reaction time, and $k_1 <<< k_2$, allowing the rate of Ni formation (d[NP]/d*t*) to be expressed as

$$\frac{d}{dt}[\mathrm{NP}] = -k_1[\mathrm{M\ salt}] + k_2[\mathrm{M\ salt}][\mathrm{M}*] \qquad [4.3]$$

The autocatalytic mechanism has been fully described for formation of Ag,[129,130] Au,[126,110,92,97] Ru,[127] and Ni[90] in convective reactions and demonstrated to describe growth of Ag,[118] Ni,[128] and Au[128] in a microwave reactor.

In Figure 4.6, the change in absorption at 488 nm shows the classical autocatalytic mechanism sigmodal growth curve behavior. To calculate k_1 and k_2 from the absorption data, the value for [M*] must be assumed to be equivalent to the number of nanoparticles in the reaction at t_∞. The number of nanoparticles is extracted from the absorption data at 488 nm using the Ni

Table 2.2: The frequencies, powers, E_0, nanoparticle size and absorbed power for each of the nine MW experiments. E_0 is based on the power measured in the cavity, not the set power of the instrument. For the TWTA these are the same, but for the Gerling, due to the water dump, the measured power is ~10% of the set power. 9 min, 4 min and 2.5 min are time from room temperature to 280 °C, and directly correspond to the powers listed in the second column.

Frequency (GHz)	Time (min)	Dissipated MW Power (W)	E_0 (V/m)	NP Diameter (nm)	k_1 (s^{-1})	k_2 ($M \cdot s^{-1}$)
18.00	9	91	6.23×10^{4}	21.2±9.6	$1.141\times10^{-4}\pm 1.05\times10^{-4}$	0.0058± 0.00488
18.00	4	123	7.24×10^{4}	20.2±5.7	$2.12\times10^{-4}\pm 1.37\times10^{-4}$	0.0112±0.00374
18.00	2.5	151	8.02×10^{4}	16.3±5.1	$3.17\times10^{-4}\pm 1.79\times10^{-4}$	0.0176±0.00403
15.50	9	138	7.96×10^{4}	18.8±5.6	$4.62\times10^{-4}\pm 4.72\times10^{-5}$	0.0058 ± 5.2010^{-4}
15.50	4	174	8.94×10^{4}	17.9±4.7	$3.61\times10^{-4}\pm 2.05\times10^{-4}$	0.0181±0.00249
15.50	2.5	232	1.03×10^{5}	15.6±6.4	$4.1\times10^{-4}\pm 1.98\times10^{-4}$	0.0189±0.00142
2.45	9	140	1.64×10^{5}	35.1±11.6	$3.85\times10^{-4}\pm2.07\times10^{-4}$	0.02±0.0022
2.45	4	148	1.68×10^{5}	30.7±15.5	$1.52\times10^{-5}\pm 2.06\times10^{-4}$	0.0008± 0.00213
2.45	2.5	160	1.74×10^{5}	29.2±10.6	$1.176\times10^{-4}\pm 1.08\times10^{-4}$	0.0059± 0.00493
Control	9	N/A	N/A	26.8±7.15	$4.5\times10^{-5}\pm 1.01\times10^{-4}$	0.0025±0.008
Control	4	N/A	N/A	19.3±9.34	$6.7\times10^{-5}\pm 2.89\times10^{-4}$	0.0061±0.028
Control	2.5	N/A	N/A	17.48±7.09	$2.4\times10^{-4}\pm 6.34\times10^{-5}$	0.0238±0.006

extinction values for the isolated TEM sizes at the completion of the reaction and the numbers are listed in Table 4.2, along with the values for k_1 and k_2.[128,51,52,108] The frequency dependence on the values of k_1 and k_2 are shown in Figure 4.5 B and 4.5 C, and exhibit no immediate correlation.

To develop a model that allows the frequency dependent behavior to be understood the configurational energy of the reaction, which is related to the power absorbed (P_{abs}) by the

reactants must be considered. This will be a function of both power applied and frequency, as shown using the theoretical treatment of EM heating of molecules of proposed by Richert, et al.[72,73] The configurational energy is anticipated to be proportional to the power absorbed divided by the heat capacity of the molecule, and the difference between it and the bath temperature may explain the observed enhanced reactions. The configurational energy approach of Richert assumes the increase in energy can be modeled as a temperature difference, such that

$$\Delta T = T_{\text{configurational}} - T_{\text{bath}} = \frac{\varepsilon_0 E_0^2 \Delta\varepsilon}{2\Delta c_v}\left(\frac{\omega^2\tau^2}{1+\omega^2\tau^2}\right) = \frac{\tau P_{\text{abs}}}{\Delta c_p} \quad [4.4]$$

T_{bath} is the measured solution temperature, E_0 is the strength of the electric field in the cavity (dependent on power and frequency of the microwave, as well as the dimensions of the cavity), $\Delta\varepsilon$ is the dielectric function strength (the static dielectric function constant minus the dielectric function constant at very high frequencies), Δc_v is the slow mode part of the volumetric specific heat (approximated as ½ the volumetric specific heat for liquids,), Δc_p is the slow mode part of the specific heat (approximated as ½ the volumetric specific heat), ω is the frequency in radians, and τ is the relaxation time of the molecule. E_o is determined from the power, frequency and volume of the cavity (if cubic or rectangular multimodal with mode stirrer) using

$$E_0 = E_{\text{rms}} = \left(4\frac{(P/V)\,Q}{\omega\varepsilon_0}\right)^{1/2} \quad [4.5]$$

Where P is the power dissipated in the system, V is the volume of the cavity, and Q is the quality factor of the cavity, which can be estimated by $2V/\sigma S$, where σ is the skin depth of the cavity at frequency ω, and S is the surface area of the inside of the cavity. For a single mode cavity (TE_{10n}), where the power is not uniformly distributed, $E_0 = \sqrt{2}\cdot E_{\text{rms}}$. The configurational temperature (energy) will be small is empirical understood as the energy arising when a molecule

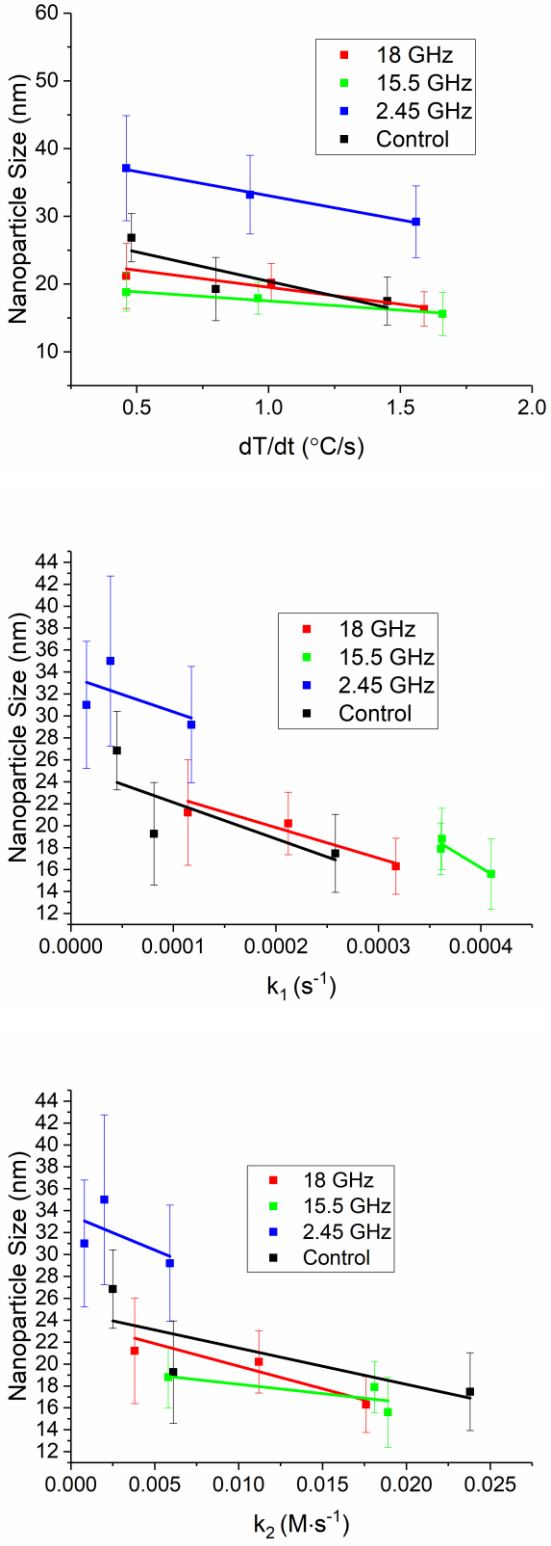

Figure 4.5: Plots of nanoparticle size vs A) dT/dt of reaction, B) k_1 of reaction and C) k_2 of reaction. N=2 for all.

(nanocrystal) absorbs a microwave photon increasing its mobility in solution above diffusional rates for the molecule (nanocrystal) at the temperature of the ensemble solution.

To calculate ΔT, the relaxation time (τ) of the molecule can be calculated from the Debye equation,

$$\varepsilon^* = \varepsilon_\infty + \frac{\varepsilon_\infty - \varepsilon_s}{1 + i\omega\tau} \quad [4.6]$$

Using a linear Cole-Cole plot of ε' vs ε''/ω, where ε' and ε'' are taken from VNA measurements (Table 4.1). The relaxation time (τ) is the slope of the Cole plot.[25]

Experimentally, ΔT is unmeasurable as the value at typical microwave powers is nano-kelvin. However, the value of ΔT is directly related to $P_{abs} * \tau$, where τ is the relaxation time in picoseconds. Therefore, a plot of the P_{abs} vs. the nanocrystal size isolated in the microwave reactions is meaningful (Figure 4.7A). While it is commonly accepted that microwave effects will be undetectable at ΔT's lower than a few Kelvin, a clear trend is noticeable here. The plot can be fit to an exponential function across all frequency ranges providing a scaling law for microwave absorption. The scaling law behavior can be rationalized as a result of the change in dielectric function constant for a metal with size, that scales as the diameter cubed,[110,51,108] where for sizes below 50 nm the absorptivity term (ε'') dominates the dielectric function contribution. The surprising correlation is reasonable, and more importantly might explain the observed dependence on microwave power applied and frequency observed in the Ni reactions. If there were no microwave influence, we would expect to see only three sizes of NP, one for each of the $\Delta T/dt$'s. This assumption is clearly demonstrated by inspection of Figure 4.7B, where control experiments were performed under identical conditions to the microwave studies under convective heating. For comparison, control experiments were done with CEM tubes in an aluminum block. The block was heated

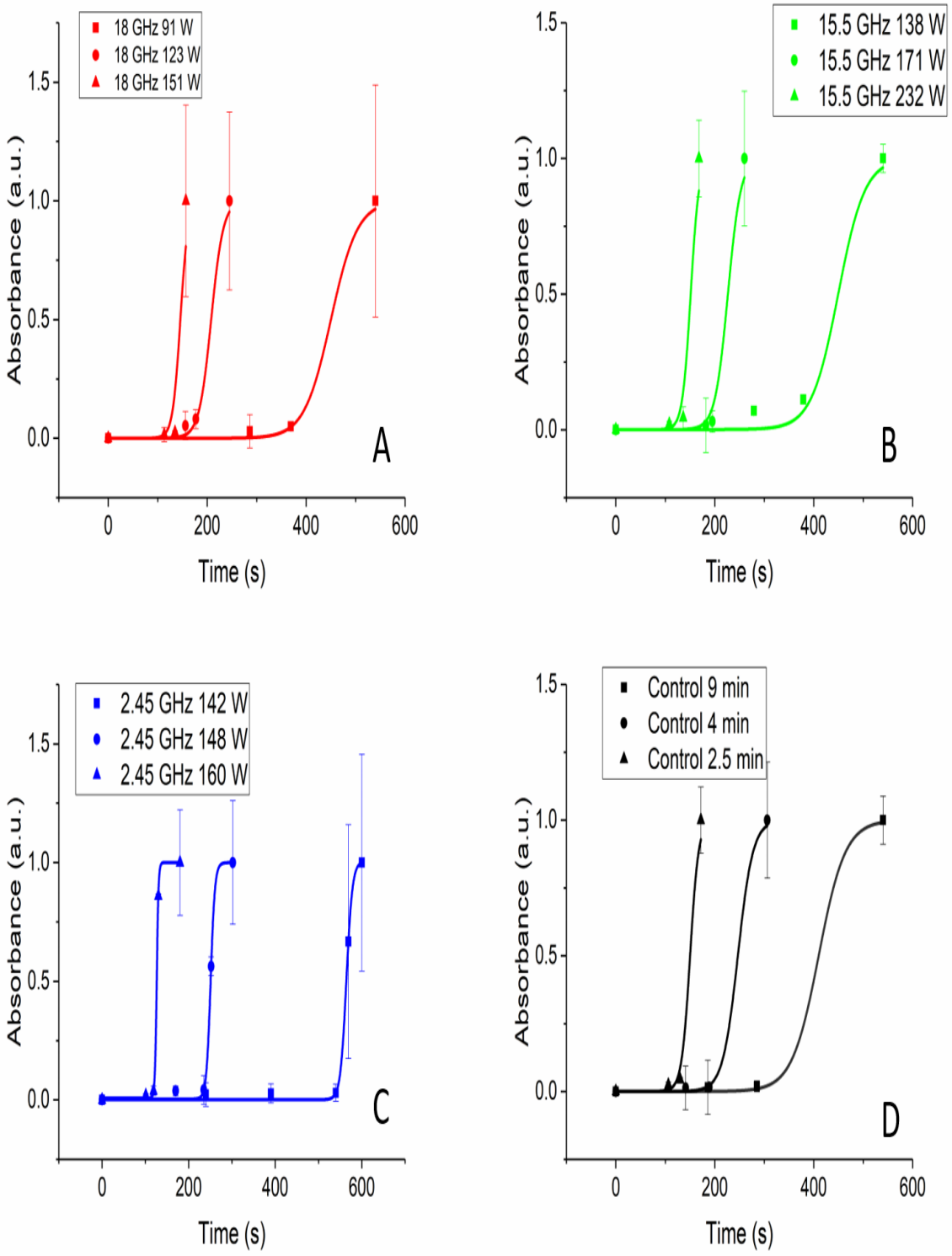

Figure 4.6: Plot of 488 nm absorbance for all reactions showing the classic sigmoidal curve of Finke–Watzky kinetics.

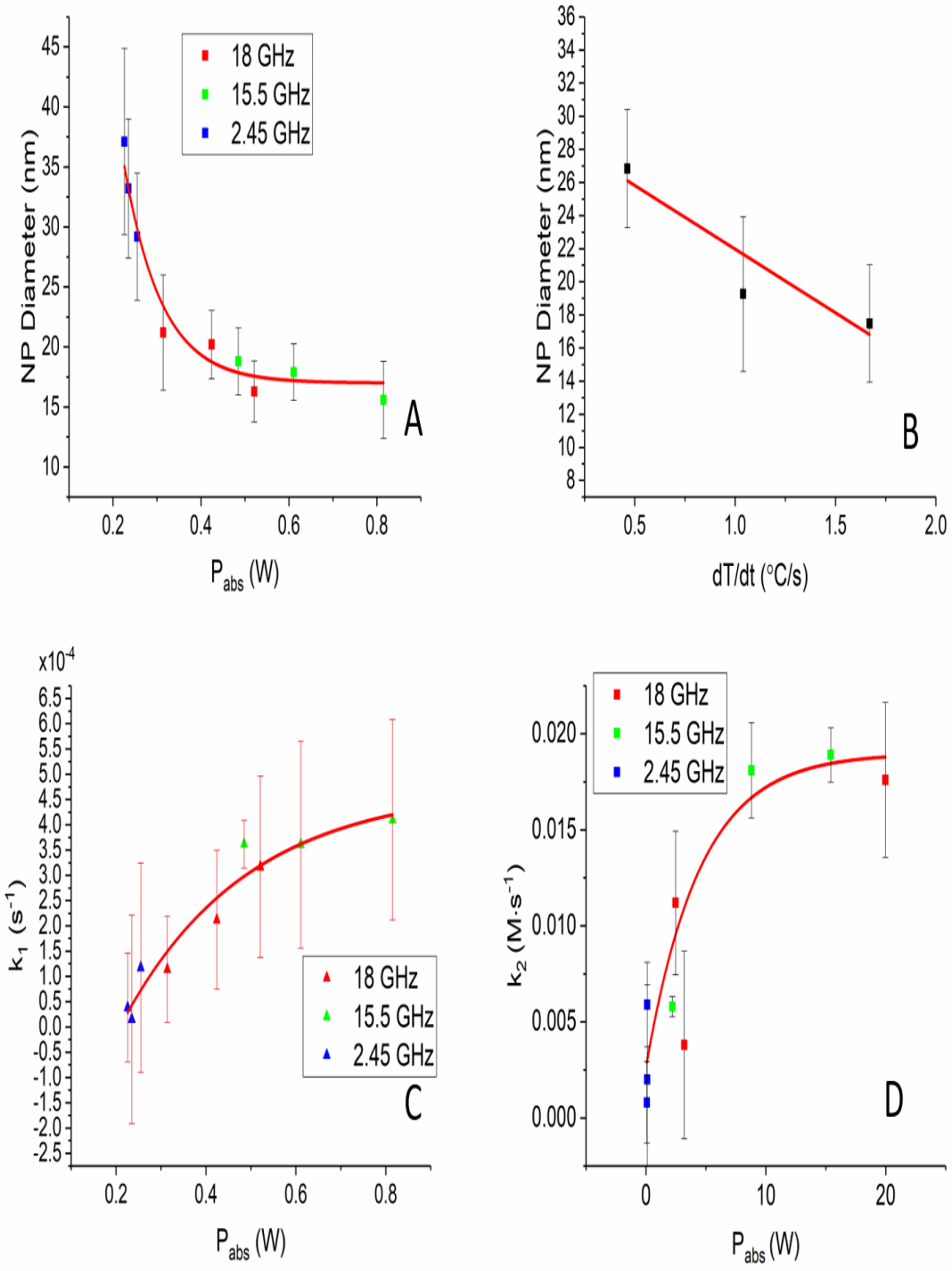

Figure 4.7: A) Plot of Ni NP size vs absorbed power calculated using Eqn. 4. B) Plot of control Ni NP made in Al block vs d*T*/*dt*. C) Plot of k_1 vs P_{abs} by the reaction at the beginning of the reaction and D) k_2 vs. P_{abs} by the reaction when the NP are 4 nm in diameter.

so that the tubes inserted into holes in the block would reach 280 °C in 2.5, 4, and 9 minutes, to achieve the same $\Delta T/dt$'s as the microwave experiments.

In Figure 4.7B the $\Delta T/dt$ vs NP size is plotted for the control experiments at three ramp rates. These ramp rates are identical to the ramp rates employed in the microwave reactor. As expected a linear correlation occurs for the isolated materials from the convective reaction.

The observation of scaling law behavior attributable to microwave absorption, which is both frequency and power applied dependent, suggest that the impact on the values of k_1 and k_2 in the autoctalytic reaction mechanism can be directly analyzed under the various experimental conditions. Previous studies on microwave autocatalytic reactions have suggested microwave absorption is predominately in k_2.[118] In Figure 4.7C and 4.7D, a plot of k_1 and k_2 vs P_{abs} for the various reactions show a clear exponential dependence. Since both reaction rates are expected to follow the Arrhenius equation, we can extract the E_a and Arrhenius pre-factor (A) for both the nucleation event and autocatalytic growth. The Arrhenius law fits yield values for k_1 of $E_a^{(1)}/R$ = 0.869 kJ·W/mol with an $A^{(1)}$ of 16.1 x 10^{-4} s^{-1}, while for k_2 an $E_a^{(2)}/R$ of 0.162 kJ·W/mol and an $A^{(2)}$ of 115.2 x 10^{-4} s^{-1} is measured. The ability to fit the microwave reactions to Arrhenius law conform the reactions follow classical thermodynamic behavior, allowing the microwave effects to be understood in terms of microwave absorption by the reactants, or in other words the microwave flux as defined by applied power / frequency. Since the P_{abs} is dependent on reaction concentrations of precursors, a generalized strategy for reaction design would be to optimize concentration and applied power at a given frequency to achieve the desired particle size and size dispersity.

4.4 Conclusions

Evidence of microwave enhanced reactions, especially evidence of so-called "nonthermal" effects, is difficult to find but often reported in the literature. The increased application of physics to the microwave effect question is demonstrating that the so-called microwave specific effects can be fully understood in terms of the role that microwave cross-section plays on reaction mechanisms. In nanocrystals, it is clear that microwaves do not break bonds, do not change thermodynamic or kinetics; however, microwave enhancement can be observed. In this paper, the effect of the microwave applied power and frequency at constant $\Delta T/dt$ is explored for Ni growth under autocatalytic conditions. The results show a scaling law behavior with size due to the increasing microwave cross section of the growing nanocrystal. The increased P_{abs} that occurs is understood in terms of local energy changes as defined by Richert. The study shows definitively that the reaction rate for nanocrystal growth is a problem of electromagnetic radiation absorption and thus will be dependent on the applied power, frequency, relaxation time, and concentration of the reactants. It is believed this strategy can be applied to organic reactions to explain rate acceleration, although the magnitude of the change in P_{abs} may mask the kinetic effects. It is hoped that continued exploration of microwave enhancement using physical chemistry will allow reactions to be translated efficiently from a convective format to a microwave format with minimal guesswork. This would lead to substantial energy savings[6,7] due to the higher efficiency of a microwave to volumetrically heat when compare to convective reactors.

REFERENCES

1. Johnston-Peck, A. C.; Wang, J.; Tracy, J. B., Synthesis and Structural and Magnetic Characterization of Ni (Core)/NiO (Shell) Nanoparticles. *ACS Nano* **2009,** *3* (5), 1077-1084.

2. Robinson, J.; Kingman, S.; Irvine, D.; Licence, P.; Smith, A.; Dimitrakis, G.; Obermayer, D.; Kappe, C. O., Electromagnetic simulations of microwave heating experiments using reaction vessels made out of silicon carbide. *Physical Chemistry Chemical Physics* **2010,** *12* (36), 10793-10800.

3. Pozar, D. M., *Microwave Engineering*. 3 ed.; John Wiley &Sons, Inc: 2005.

4. Lide, D. R., *CRC handbook of chemistry and physics*. CRC press: 2004; Vol. 85.

5. Hayes, B. L., *Microwave Chemistry: Chemistry at the Speed of Light*. 1 ed.; CEM Corp.: 2002.

6. Leadbeater, N. E., *Microwave Heating as Tool for Sustainable Chemistry*. Taylor and Francis Group: Boca Raton, 2010.

7. Razzaq, T.; Kappe, C. O., On the Energy Efficiency of Microwave-Assisted Organic Reactions. *ChemSusChem* **2008,** *1* (1-2), 123-132.

8. Kappe, C. O., Controlled microwave heating in modern organic synthesis. *Angewandte Chemie International Edition* **2004,** *43* (46), 6250-6284.

9. Barnard, T. M.; Leadbeater, N. E.; Boucher, M. B.; Stencel, L. M.; Wilhite, B. A., Continuous-flow preparation of biodiesel using microwave heating. *Energy & Fuels* **2007,** *21* (3), 1777-1781.

10. Moseley, J. D.; Kappe, C. O., A critical assessment of the greenness and energy efficiency of microwave-assisted organic synthesis. *Green Chemistry* **2011,** *13* (4), 794-806.

11. de la Hoz, A.; Diaz-Ortiz, A.; Moreno, A., Review of Non-Thermal Effects of Microwave Irradiation in Organic Synthesis. *Journal of Microwave Power and Electricromagnetic Energy* **2007,** *41* (1), 36-57.

12. Hosseini, M.; Stiasni, N.; Barbieri, V.; Kappe, C. O., Microwave-assisted asymmetric organocatalysis. A probe for nonthermal microwave effects and the concept of simultaneous cooling. *The Journal of Organic Chemistry* **2007,** *72* (4), 1417-1424.

13. Rodríguez, A. M.; Prieto, P.; de la Hoz, A.; Díaz-Ortiz, A.; García, J. I., The Issue of 'Molecular Radiators' in Microwave-Assisted Reactions. Computational Calculations on Ring Closing Metathesis (RCM). *Organic & Biomolecular Chemistry* **2014,** *12* (15), 2436-2445.

14. Rodríguez, A. M.; Prieto, P.; de la Hoz, A.; Díaz-Ortiz, Á.; Martín, D. R.; García, J. I., Influence of Polarity and Activation Energy in Microwave–Assisted Organic Synthesis (MAOS). *ChemistryOpen* **2015,** *4* (3), 308-317.

15. Kim, K.-J.; Oleksak, R. P.; Hostetler, E. B.; Peterson, D. A.; Chandran, P.; Schut, D. M.; Paul, B. K.; Herman, G. S.; Chang, C.-H., Continuous Microwave-Assisted Gas–Liquid

Segmented Flow Reactor for Controlled Nucleation and Growth of Nanocrystals. *Crystal Growth & Design* **2014,** *14* (11), 5349-5355.

16. Metaxas, A. C.; Meredith, R. J., *Industrial Microwave Heating*. Institute of Engineering and Technology: United Kingdom, 1983.

17. Steurga, D. A. C.; Gaillard, P., Microwave Athermal Effects in Chemistry: Part 1 Historical Background and Fundamentals of Wave-Matter Interaction. *Journal of Microwave Power and Electromagnetic Energy* **1996,** *31* (2), 14.

18. Sharma, A., Size-dependent energy band gap and dielectric functionconstant within the generalized Penn model applied to a semiconductor nanocrystallite. *Journal of applied physics* **2006,** *100* (8), 084301.

19. Brus, L., Electronic wave functions in semiconductor clusters: experiment and theory. *The Journal of Physical Chemistry* **1986,** *90* (12), 2555-2560.

20. Gor'kov, L. P.; Eliashberg, G., Minute Metallic Particles in an Electromagnetic Field. *Soviet Journal of Experimental and Theoretical Physics* **1965,** *21*, 940.

21. Marquardt, P.; Nimtz, G., Size-Dependent Dielectric functionResponse of Small Metal Particles. *Physical Review B* **1991,** *43* (17), 14245.

22. Gilbert, T. L., A phenomenological theory of damping in ferromagnetic materials. *IEEE Transactions on Magnetics* **2004,** *40* (6), 3443-3449.

23. Bødker, F.; Mørup, S.; Linderoth, S., Surface effects in metallic iron nanoparticles. *Physical Review Letters* **1994,** *72* (2), 282.

24. He, X.; Zhong, W.; Au, C.-T.; Du, Y., Size Dependence of the Magnetic Properties of Ni Nanoparticles Prepared by Thermal Decomposition Method. *Nanoscale Research Letters* **2013,** *8* (1), 446.

25. Fröhlich, H., *Theory of Dielectrics: Dielectric functionConstant and Dielectric functionLoss*. Clarendon Press: 1958.

26. Nix, F. C.; Shockley, W., Order-Disorder Transformations in Alloys. *Reviews of Modern Physics* **1938,** *10* (1), 1.

27. Kumar, R.; Sharma, G.; Kumar, M., Effect of size and shape on the vibrational and thermodynamic properties of nanomaterials. *Journal of Thermodynamics* **2013,** *2013*.

28. Madduri, P. P.; Kaul, S., Core and surface/interface magnetic anisotropies in nanocrystalline nickel. *Journal of Alloys and Compounds* **2016,** *689*, 533-541.

29. Kittel, C., On the theory of ferromagnetic resonance absorption. *Physical Review* **1948,** *73* (2), 155.

30. Zhang, X. F.; Guan, P. F.; Dong, X. L., Transform between the permeability and permittivity in the close-packed Ni nanoparticles. *Appl Phys Lett* **2010,** *97*, 033107.

31. Washington, A. L.; Strouse, G. F., Microwave synthetic route for highly emissive TOP/TOP-S passivated CdS quantum dots. *Chemistry of Materials* **2009,** *21* (15), 3586-3592.

32. Lovingood, D. D.; Strouse, G. F., Microwave induced in-situ active ion etching of growing InP nanocrystals. *Nano letters* **2008,** *8* (10), 3394-3397.

33. Besson, C.; Finney, E. E.; Finke, R. G., A mechanism for transition-metal nanoparticle self-assembly. *Journal of the American Chemical Society* **2005,** *127* (22), 8179-8184.

34. Watzky, M. A.; Finney, E. E.; Finke, R. G., Transition-metal nanocluster size vs formation time and the catalytically effective nucleus number: A mechanism-based treatment. *Journal of the American Chemical Society* **2008,** *130* (36), 11959-11969.

35. Nam, K. M.; Shim, J. H.; Ki, H.; Choi, S. I.; Lee, G.; Jang, J. K.; Jo, Y.; Jung, M. H.; Song, H.; Park, J. T., Single-Crystalline Hollow Face-Centered-Cubic Cobalt Nanoparticles from Solid Face-Centered-Cubic Cobalt Oxide Nanoparticles. *Angewandte Chemie International Edition* **2008,** *47* (49), 9504-9508.

36. Slater, J. C., Microwave electronics. *Reviews of Modern Physics* **1946,** *18* (4), 441.

37. Harrington, R. F., *Introduction to electromagnetic engineering*. Courier Corporation: 2003.

38. Hong, K. H.; Roberts, J. A., Microwave properties of liquids and solids using a resonant microwave cavity as a probe. *Journal of Applied Physics* **1974,** *45* (6), 2452-2456.

39. Huang, C.; Bhalla, A. S.; Lanagan, M. T.; Cross, L. E.; Guo, R., Dielectric functionmeasurement of ferroelectric Sr 0.61 Ba 0.39 Nb 2 O 6 single crystal fiber using cavity perturbation method. *Applied Physics Letters* **2005,** *86* (12), 122903.

40. Radar Circuit Analysis. Force, D. o. t. A., Ed. Air Force: 1951; Vol. Air Force Manual No. 52-8.

41. Baker-Jarvis, J.; Vanzura, E. J.; Kissick, W., Improved technique for determining complex permittivity with the transmission/reflection method. *Microwave Theory and Techniques, IEEE Transactions on* **1990,** *38* (8), 1096-1103.

42. Wei, J.; Liu, J.; Li, S., Electromagnetic and microwave absorption properties of Fe 3 O 4 magnetic films plated on hollow glass spheres. *Journal of Magnetism and Magnetic Materials* **2007,** *312* (2), 414-417.

43. Yang, Y.; Li, Z. W.; Neo, C. P.; Ding, J., Model design on calculations of microwave permeability and permittivity of Fe/SiO 2 particles with core/shell structure. *Journal of Physics and Chemistry of Solids* **2014,** *75* (2), 230-235.

44. Baker-Jarvis, J.; Janezic, M. D.; Grosvenor Jr, J. H.; Geyer, R. G., Transmission/reflection and short-circuit line methods for measuring permittivity and permeability. *NASA STI/Recon Technical Report N* **1992,** *93*, 12084.

45. Adam, S. F., *Microwave Theory and Applications*. 2nd ed.; Prentice Hall: 1969.

46. Knott, E. F.; Schaeffer, J. F.; Tulley, M. T., *Radar Cross Section*. SciTech Publishing: 2004.

47. Cole, H., Bragg's law and energy sensitive detectors. *Journal of Applied Crystallography* **1970,** *3* (5), 405-406.

48. Skoog, D. A.; Holler, F. J.; Crouch, S. R., *Principles of instrumental analysis*. Thomson Brooks/Cole: 2007.

49. Fuwa, K.; Valle, B., The Physical Basis of Analytical Atomic Absorption Spectrometry. The Pertinence of the Beer-Lambert Law. *Analytical Chemistry* **1963,** *35* (8), 942-946.

50. Wu, C.-H.; Chang, H.-W.; Chern, J.-M., Basic dye decomposition kinetics in a photocatalytic slurry reactor. *Journal of hazardous materials* **2006,** *137* (1), 336-343.

51. Link, S.; El-Sayed, M. A., Size and temperature dependence of the plasmon absorption of colloidal gold nanoparticles. *The Journal of Physical Chemistry B* **1999,** *103* (21), 4212-4217.

52. Haiss, W.; Thanh, N. T.; Aveyard, J.; Fernig, D. G., Determination of size and concentration of gold nanoparticles from UV− Vis spectra. *Analytical chemistry* **2007,** *79* (11), 4215-4221.

53. Washington, A. L.; Strouse, G. F., Selective microwave absorption by trioctyl phosphine selenide: does it play a role in producing multiple sized quantum dots in a single reaction? *Chemistry of Materials* **2009,** *21* (13), 2770-2776.

54. Mohamed, M. B.; AbouZeid, K. M.; Abdelsayed, V.; Aljarash, A. A.; El-Shall, M. S., Growth Mechanism of Anisotropic Gold Nanocrystals via Microwave Synthesis: Formation of Dioleamide by Gold Nanocatalysis. *ACS Nano* **2010,** *4* (5), 2766-2772.

55. Atkins, T. M.; Thibert, A.; Larsen, D. S.; Dey, S.; Browning, N. D.; Kauzlarich, S. M., Femtosecond ligand/core dynamics of microwave-assisted synthesized silicon quantum dots in aqueous solution. *Journal of the American Chemical Society* **2011,** *133* (51), 20664-20667.

56. Gerbec, J. A.; Magana, D.; Washington, A.; Strouse, G. F., Microwave-Enhanced Reaction Rates for Nanoparticle Synthesis. *Journal of the American Chemical Society* **2005,** *127* (45), 15791-15800.

57. Lovingood, D. D.; Owens, J. R.; Seeber, M.; Kornev, K. G.; Luzinov, I., Controlled microwave-assisted growth of silica nanoparticles under acid catalysis. *ACS Applied Materials & Interfaces* **2012,** *4* (12), 6875-6883.

58. Hayn, R. A.; Owens, J. R.; Boyer, S. A.; McDonald, R. S.; Lee, H. J., Preparation of highly hydrophobic and oleophobic textile surfaces using microwave-promoted silane coupling. *Journal of Materials Science* **2011,** *46* (8), 2503-2509.

59. Lovingood, D. D.; Oyler, R. E.; Strouse, G. F., Composition Control and Localization of S2− in CdSSe Quantum Dots Grown from Li4 [Cd10Se4 (SPh) 16]. *Journal of the American Chemical Society* **2008,** *130* (50), 17004-17011.

60. Kappe, C. O.; Pieber, B.; Dallinger, D., Microwave effects in organic synthesis: myth or reality? *Angewandte Chemie International Edition* **2013,** *52* (4), 1088-1094.

61. Adnadjević, B.; Jovanović, J.; Potkonjak, B., A novel approach to the explanation the effect of microwave heating on isothermal kinetic of crosslinking polymerization of acrylic acid. *Russian Journal of Physical Chemistry A* **2013,** *87* (13), 2115-2120.

62. Binner, J.; Hassine, N.; Cross, T., The possible role of the pre-exponential factor in explaining the increased reaction rates observed during the microwave synthesis of titanium carbide. *Journal of Materials Science* **1995,** *30* (21), 5389-5393.

63. de la Hoz, A.; Diaz-Ortiz, A.; Moreno, A., Microwaves in organic synthesis. Thermal and non-thermal microwave effects. *Chemical Society Reviews* **2005,** *34* (2), 164-178.

64. Dudley, G. B.; Richert, R.; Stiegman, A. E., On the existence of and mechanism for microwave-specific reaction rate enhancement. *Chemical Science* **2015,** *6* (4), 2144-2152.

65. Rosana, M. R.; Tao, Y.; Stiegman, A. E.; Dudley, G. B., On the rational design of microwave-actuated organic reactions. *Chemical Science* **2012,** *3* (4), 1240-1244.

66. Dudley, G. B.; Stiegman, A. E.; Rosana, M. R., Correspondence on microwave effects in organic synthesis. *Angewandte Chemie International Edition* **2013,** *52* (31), 7918-7923.

67. Hunt, J.; Ferrari, A.; Lita, A.; Crosswhite, M.; Ashley, B.; Stiegman, A., Microwave-specific enhancement of the carbon–carbon dioxide (Boudouard) reaction. *The Journal of Physical Chemistry C* **2013,** *117* (51), 26871-26880.

68. Crosswhite, M.; Hunt, J.; Southworth, T.; Serniak, K.; Ferrari, A.; Stiegman, A., Development of Magnetic Nanoparticles as Microwave-Specific Catalysts for the Rapid, Low-Temperature Synthesis of Formalin Solutions. *ACS Catalysis* **2013,** *3* (6), 1318-1323.

69. Rosana, M. R.; Hunt, J.; Ferrari, A.; Southworth, T. A.; Tao, Y.; Stiegman, A. E.; Dudley, G. B., Microwave-specific acceleration of a Friedel–Crafts reaction: evidence for selective heating in homogeneous solution. *The Journal of organic chemistry* **2014,** *79* (16), 7437-7450.

70. Leadbeater, N. E.; Smith, R. J., In situ Raman spectroscopy as a probe for the effect of power on microwave-promoted Suzuki coupling reactions. *Organic & Biomolecular Chemistry* **2007,** *5* (17), 2770-2774.

71. Gutmann, B.; Obermayer, D.; Reichart, B.; Prekodravac, B.; Irfan, M.; Kremsner, J. M.; Kappe, C. O., Sintered Silicon Carbide: A New Ceramic Vessel Material for Microwave Chemistry in Single-Mode Reactors. *Chemistry–A European Journal* **2010,** *16* (40), 12182-12194.

72. Huang, W.; Richert, R., The physics of heating by time-dependent fields: microwaves and water revisited. *The Journal of Physical Chemistry B* **2008,** *112* (32), 9909-9913.

73. Huang, W.; Richert, R., Dynamics of glass-forming liquids. XIII. Microwave heating in slow motion. *The Journal of Chemical Physics* **2009,** *130* (19), 194509.

74. Benet, W. E.; Lewis, G. S.; Yang, L. Z.; Hughes, P. D., The mechanism of the reaction of the Tollens reagent. *Journal of Chemical Research* **2011,** *35* (12), 675-677.

75. Williams, E. H.; Davydov, A. V.; Motayed, A.; Sundaresan, S. G.; Bocchini, P.; Richter, L. J.; Stan, G.; Steffens, K.; Zangmeister, R.; Schreifels, J. A., Immobilization of streptavidin on 4H–SiC for biosensor development. *Applied surface science* **2012,** *258* (16), 6056-6063.

76. von Hippel, A., *Dielectric functionMaterials and Applications*. Artech House: Boston, 1995.

77. Harvey, A. F., *Microwave Engineering*. Academic Press: New York, 1963.

78. Obermayer, D.; Gutmann, B.; Kappe, C. O., Microwave chemistry in silicon carbide reaction vials: separating thermal from nonthermal effects. *Angewandte Chemie* **2009,** *121* (44), 8471-8474.

79. Mourdikoudis, S.; Liz-Marzán, L. M., Oleylamine in Nanoparticle Synthesis. *Chemistry of Materials* **2013,** *25* (9), 1465-1476.

80. Watzky, M. A.; Finke, R. G., Transition Metal Nanocluster Formation Kinetic and Mechanistic Studies. A New Mechanism when Hydrogen is the Reductant: Slow, Continuous Nucleation and Fast Autocatalytic Surface Growth. *Journal of the American Chemical Society* **1997,** *119* (43), 10382-10400.

81. Jhung, S. H.; Jin, T.; Hwang, Y. K.; Chang, J. S., Microwave Effect in the Fast Synthesis of Microporous Materials: Which Stage Between Nucleation and Crystal Growth is Accelerated by Microwave Irradiation? *Chemistry–A European Journal* **2007,** *13* (16), 4410-4417.

82. Gawande, M. B.; Shelke, S. N.; Zboril, R.; Varma, R. S., Microwave-Assisted Chemistry: Synthetic Applications for Rapid Assembly of Nanomaterials and Organics. *Accounts of Chemical Research* **2014,** *47* (4), 1338-1348.

83. Washington, A. L.; Strouse, G. F., Microwave Synthesis of CdSe and CdTe Nanocrystals in Nonabsorbing Alkanes. *Journal of the American Chemical Society* **2008,** *130* (28), 8916-8922.

84. Zedan, A. F.; Sappal, S.; Moussa, S.; El-Shall, M. S., Ligand-Controlled Microwave Synthesis of Cubic and Hexagonal CdSe Nanocrystals Supported on Graphene. Photoluminescence Quenching by Graphene. *The Journal of Physical Chemistry C* **2010,** *114* (47), 19920-19927.

85. Siramdas, R.; McLaurin, E. J., InP Nanocrystals with Color-Tunable Luminescence by Microwave-Assisted Ionic-Liquid Etching. *Chemistry of Materials* **2017,** *29* (5), 2101-2109.

86. Muthuswamy, E.; Iskandar, A. S.; Amador, M. M.; Kauzlarich, S. M., Facile Synthesis of Germanium Nanoparticles with Size Control: Microwave Versus Conventional Heating. *Chemistry of Materials* **2012,** *25* (8), 1416-1422.

87. Carnevale, D. J.; Shatruk, M.; Strouse, G. F., Ligand Passivated Core–Shell FePt@ Co Nanomagnets Exhibiting Enhanced Energy Product. *Chemistry of Materials* **2016,** *28* (15), 5480-5487.

88. Bilecka, I.; Niederberger, M., Microwave Chemistry for Inorganic Nanomaterials Synthesis. *Nanoscale* **2010,** *2* (8), 1358-1374.

89. Lu, G.; Li, X.; Jiang, H., Electrical and Shielding Properties of ABS Resin Filled with Nickel-Coated Carbon Fibers. *Composites Science and Technology* **1996,** *56* (2), 193-200.

90. LaGrow, A. P.; Ingham, B.; Toney, M. F.; Tilley, R. D., Effect of Surfactant Concentration and Aggregation on the Growth Kinetics of Nickel Nanoparticles. *The Journal of Physical Chemistry C* **2013,** *117* (32), 16709-16718.

91. Finney, E. E.; Finke, R. G., Nanocluster nucleation and growth kinetic and mechanistic studies: A review emphasizing transition-metal nanoclusters. *Journal of Colloid and Interface Science* **2008,** *317* (2), 351-374.

92. Turkevich, J.; Stevenson, P. C.; Hillier, J., A study of the nucleation and growth processes in the synthesis of colloidal gold. *Discussions of the Faraday Society* **1951,** *11*, 55-75.

93. Polte, J. r.; Ahner, T. T.; Delissen, F.; Sokolov, S.; Emmerling, F.; Thünemann, A. F.; Kraehnert, R., Mechanism of gold nanoparticle formation in the classical citrate synthesis method derived from coupled in situ XANES and SAXS evaluation. *Journal of the American Chemical Society* **2010,** *132* (4), 1296-1301.

94. Perala, S. R. K.; Kumar, S., On the two-step mechanism for synthesis of transition-metal nanoparticles. *Langmuir* **2014,** *30* (42), 12703-12711.

95. Mondloch, J. E.; Yan, X.; Finke, R. G., Monitoring Supported-Nanocluster Heterogeneous Catalyst Formation: Product and Kinetic Evidence for a 2-Step, Nucleation and Autocatalytic Growth Mechanism of Pt (0) n Formation from H_2PtCl_6 on Al_2O_3 or TiO_2. *Journal of the American Chemical Society* **2009,** *131* (18), 6389-6396.

96. Bentea, L.; Watzky, M. A.; Finke, R. G., Sigmoidal Nucleation and Growth Curves Across Nature Fit by the Finke–Watzky Model of Slow Continuous Nucleation and Autocatalytic Growth: Explicit Formulas for the Lag and Growth Times Plus Other Key Insights. *The Journal of Physical Chemistry C* **2017,** *121* (9), 5302-5312.

97. Kimling, J.; Maier, M.; Okenve, B.; Kotaidis, V.; Ballot, H.; Plech, A., Turkevich method for gold nanoparticle synthesis revisited. *The Journal of Physical Chemistry B* **2006,** *110* (32), 15700-15707.

98. Chen, Y.; Peng, D.-L.; Lin, D.; Luo, X., Preparation and magnetic properties of nickel nanoparticles via the thermal decomposition of nickel organometallic precursor in alkylamines. *Nanotechnology* **2007,** *18* (50), 505703.

99. Chung, D., Electromagnetic Interference Shielding Effectiveness of Carbon Materials. *Carbon* **2001,** *39* (2), 279-285.

100. Garnett, J. M., Colours in Metal Glasses, in Metallic Films, and in Metallic Solutions. II. *Philosophical Transactions of the Royal Society of London. Series A, Containing Papers of a Mathematical or Physical Character* **1906**, 237-288.

101. Mantese, J. V.; Micheli, A. L.; Dungan, D. F.; Geyer, R. G.; Baker-Jarvis, J.; Grosvenor, J., Applicability of Effective Medium Theory to Ferroelectric/Ferrimagnetic Composites with Composition and Frequency-Dependent Complex Permittivities and Permeabilities. *Journal of Applied Physics* **1996,** *79* (3), 1655-1660.

102. Jonscher, A. K., Dielectric functionRelaxation in Solids. *Journal of Physics D: Applied Physics* **1999,** *32* (14), R57.

103. Henglein, A., Physicochemical Properties of Small Metal Particles in Solution: Microelectrode Reactions, Chemisorption, Composite Metal Particles, and the Atom-to-Metal Transition. *Journal of Physical Chemistry* **1993,** *97* (21), 5457-5471.

104. Zhang, Z.; Patel, R. C.; Kothari, R.; Johnson, C. P.; Friberg, S. E.; Aikens, P. A., Stable Silver Clusters and Nanoparticles Prepared in Polyacrylate and Inverse Micellar Solutions. *The Journal of Physical Chemistry B* **2000,** *104* (6), 1176-1182.

105. Irzhak, V., The mechanisms of the formation of metal-containing nanoparticles. *Review Journal of Chemistry* **2016,** *6* (4), 370-404.

106. Thanh, N. T.; Maclean, N.; Mahiddine, S., Mechanisms of nucleation and growth of nanoparticles in solution. *Chemical reviews* **2014,** *114* (15), 7610-7630.

107. Mata-Perez, F.; Perez-Benito, J. F., The Kinetic Rate Law for Autocatalytic Reactions. *Journal of Chemical Education* **1987,** *64* (11), 925.

108. Breshike, C. J.; Riskowski, R. A.; Strouse, G. F., Leaving Förster resonance energy transfer behind: Nanometal Surface Energy Transfer predicts the size-enhanced energy coupling between a metal nanoparticle and an emitting dipole. *The Journal of Physical Chemistry C* **2013,** *117* (45), 23942-23949.

109. Eustis, S.; El-Sayed, M. A., Why Gold Nanoparticles are More Precious than Pretty Gold: Noble Metal Surface Plasmon Resonance and its Enhancement of the Radiative and Nonradiative Properties of Nanocrystals of Different Shapes. *Chemical Society Reviews* **2006,** *35* (3), 209-217.

110. Liu, X.; Atwater, M.; Wang, J.; Dai, Q.; Zou, J.; Brennan, J. P.; Huo, Q., A study on gold nanoparticle synthesis using oleylamine as both reducing agent and protecting ligand. *Journal of nanoscience and nanotechnology* **2007,** *7* (9), 3126-3133.

111. Railsback, J. G.; Johnston-Peck, A. C.; Wang, J.; Tracy, J. B., Size-Dependent Nanoscale Kirkendall Effect During the Oxidation of Nickel Nanoparticles. *ACS Nano* **2010,** *4* (4), 1913-1920.

112. Herrero, M. A.; Kremsner, J. M.; Kappe, C. O., Nonthermal microwave effects revisited: on the importance of internal temperature monitoring and agitation in microwave chemistry. *The Journal of Organic Chemistry* **2008,** *73* (1), 36-47.

113. Griffiths, D. J., Introduction to Electrodynamics. AAPT: 2005.

114. Abeledo, C. R.; Selwood, P., Temperature Dependence of Spontaneous Magnetization in Superparamagnetic Nickel. *Journal of Applied Physics* **1961,** *32* (3), S229-S230.

115. Du, Y. W.; Xu, M. X.; Wu, J.; Shi, Y. B.; Lu, H. X.; Xue, R. H., Magnetic Properties of Ultrafine Nickel Particles. *Journal of Applied Physics* **1991,** *70* (10), 5903-5905.

116. Gilbert, T.; Ekstein, H., Basis of the Domain Structure Variational Principle. *Bulletin of the American Physical Society* **1956,** *1*, 25.

117. Landau, L.; Lifshitz, E., On the Theory of the Dispersion of Magnetic Permeability in Ferromagnetic Bodies. *Physikalische Zeitschrift der Sowjetunion* **1935,** *8* (153), 101-114.

118. Liu, Q.; Gao, M.-R.; Liu, Y.; Okasinski, J. S.; Ren, Y.; Sun, Y., Quantifying the Nucleation and Growth Kinetics of Microwave Nanochemistry Enabled by in Situ High-Energy X-Ray Scattering. *Nano Letters* **2016,** *16* (1), 715-720.

119. Wu, Y.; Gagnier, J.; Dudley, G. B.; Stiegman, A., The "chaperone" effect in microwave-driven reactions. *Chemical Communications* **2016,** *52* (75), 11281-11283.

120. Gutmann, B.; Schwan, A. M.; Reichart, B.; Gspan, C.; Hofer, F.; Kappe, C. O., Activation and deactivation of a chemical transformation by an electromagnetic field: evidence for specific microwave effects in the formation of Grignard reagents. *Angewandte Chemie* **2011,** *123* (33), 7778-7782.

121. Vazquez, A.; Gomez, I.; Garib, J. A.; Kharisov, B. I., Influence of precursor and power irradiation on the microwave-assisted synthesis of ZnS nanoparticles. *Synthesis and Reactivity in Inorganic, Metal-Organic, and Nano-Metal Chemistry* **2009,** *39* (2), 109-115.

122. Troitskiy, V. N.; Domashnev, I. A.; Kurkin, E. N.; Grebtsova, O. M.; Berestenko, V. I.; Balikhin, I. L.; Gurov, S. V., Synthesis and characteristics of ultra-fine superconducting powders in the Nb–N, Nb–N–C, Nb–Ti–N–C systems. *Journal of Nanoparticle Research* **2003,** *5* (5-6), 521-528.

123. Horikoshi, S.; Abe, H.; Sumi, T.; Torigoe, K.; Sakai, H.; Serpone, N.; Abe, M., Microwave frequency effect in the formation of Au nanocolloids in polar and non-polar solvents. *Nanoscale* **2011,** *3* (4), 1697-1702.

124. Caponetti, E.; Pedone, L.; Massa, R., Microwave radiation effect on the synthesis of cadmium sulphide nanoparticles in water in oil microemulsion: A preliminary study at different frequencies. *Materials Research Innovations* **2004,** *8* (1), 44-47.

125. Nyutu, E. K.; Chen, C.-H.; Dutta, P. K.; Suib, S. L., Effect of microwave frequency on hydrothermal synthesis of nanocrystalline tetragonal barium titanate. *The Journal of Physical Chemistry C* **2008,** *112* (26), 9659-9667.

126. Luty-Błocho, M.; Wojnicki, M.; Fitzner, K., Gold Nanoparticles Formation via Au(III) Complex Ions Reduction with l-Ascorbic Acid. *International Journal of Chemical Kinetics* **2017,** *49* (11), 789-797.

127. Akbayrak, S.; Özkar, S., Ruthenium (0) nanoparticles supported on xonotlite nanowire: a long-lived catalyst for hydrolytic dehydrogenation of ammonia-borane. *Dalton Transactions* **2014,** *43* (4), 1797-1805.

128. Ashley, B.; Vakil, P. N.; Lynch, B.; Dyer, C. M.; Tracy, J. B.; Owens, J.; Strouse, G. F., Microwave Enhancement of Autocatalytic Growth of Nanometals. *ACS nano* **2017**.

129. Richards, V. N.; Rath, N. P.; Buhro, W. E., Pathway from a molecular precursor to silver nanoparticles: the prominent role of aggregative growth. *Chemistry of Materials* **2010,** *22* (11), 3556-3567.

130. Harada, M.; Katagiri, E., Mechanism of silver particle formation during photoreduction using in situ time-resolved SAXS analysis. *Langmuir* **2010,** *26* (23), 17896-17905.

BIOGRAPHICAL SKETCH

BRIDGETT ASHLEY

Key Qualifications

- Experienced with 2.45 GHz, 3kW single mode GAE research s
- Experienced with 2.45 GHz, 3kW multimode MR research
- Experienced with using Vector Network Analyzers to tune single mode cavities and measure complex permittivity and complex permeability of substances
- Experienced with power x-ray diffraction
- Familiar with atomic force microscopy
- Familiar with common brands of laboratory reactors
- Familiar with AS Supercritical CO2/ hybrid
- Familiar with Traveling Wave Tube Amplifiers and horn antenna
- Proficient in LabVIEW
- Knowledgeable in MATLAB, C++, Fortran, Python and Visual Basic for Applications

Work Experience

2013- Ph.D. Student Research Fellow, Air Force Civil Engineer Center via ORISE Fellowship, Tyndall AFB, FL

- Conduct ongoing research into optimization of materials synthesis with reactions

- Conduct ongoing research into possible coating additives for directed energy decontamination
- Maintain, calibrate, and repair laboratory equipment
- Write LabVIEW code to automate data collection and facilitate experiments
- Write reports, white papers, and proposals
- Publish research papers

2010 Post Graduate Research Fellow, Air Force Research Laboratories via ORISE Fellowship, Tyndall AFB, FL

- Conduct ongoing research into possible coating additives for directed energy decontamination
- Conduct ongoing research into icephobicity and ice detachment of highly hydrophobic coatings
- Maintain, calibrate, and repair laboratory equipment
- Write LabVIEW code to automate data collection and facilitate experiments
- Write reports, white papers, and proposals

2007 Teaching Fellow, University of North Texas, Denton, TX

- Taught conceptual physics, lectured, and lead classroom discussion
- Assigned homework
- Wrote quizzes and exams
- Supervised grading assistant

2006 Teaching Assistant, University North Texas, Denton, TX

- Lead homework recitation sections for calculus and algebra based physics courses
- Proctored and graded examinations
- Supervised student physics laboratory sessions

2003 LAB ASSISTANT, TUTOR AND PAPER GRADER, SOUTHEAST MISSOURI STATE UNIVERSITY, CAPE GIRARDEAU, MO

- TUTORED ALGEBRA BASED PHYSICS AND ASTRONOMY STUDENTS
- SERVED AS AN ASSISTANT IN BOTH ALGEBRA BASED PHYSICS AND ASTRONOMY LABS
- GRADED HOMEWORK AND LABORATORY REPORTS
- Lead astronomy night laboratory sessions

Education

2012-current Ph. D. Program in Materials Chemistry, Florida State University, incomplete

- Major Professor: Dr. Geoffrey Strouse, Professor, Department of Chemistry and Biochemistry,

  Florida State University
- Grade Point Average 3.8/4.0
- Anticipated completion date Fall 2017

2008 **M.S. – Physics**, University of North Texas

- Final Paper Entitled: "Electromagnetic Properties of Glassy Carbon from 80K to 300K"

  Major Professor: Dr. J.A. Roberts, Professor, Department of Physics, University of North Texas
- Grade Point Average 3.4/4.0

2005 **B.S. – Physics,** Southeast Missouri State University

2005 **B.S. – Engineering Physics** (APE Option, ABET Accredited)

- Minor in Mathematics
- Member of SEMO chapter of Society of Physics Students 2001-2005
- Air Force ROTC special student
- Grade Point Average 3.4/4.0

Additional Education **2010**, Gulf Coast State College

Data Acquisition and Control Systems (Grade 4.0/4.0)

Publications

B. Ashley, P.N. Vakil, D. Tracy, J. Owens, G.F. Strouse. "Physical Considerations in Assisted Synthesis of Magnetic Nanoparticles." In Preparation 2017.

B. Ashley, J. Owens, G. F. Strouse. “Frequency Dependent Effects of Assisted Synthesis of Magnetic Nanoparticles.” In Preparation 2017.

B. Ashley, D.D. Lovingood, Y.C. Chiu, H. Gao, J. Owens, G.F. Strouse. “Specific Effects in Chemistry Explored through Reactor Vessel Design, Theory, and Spectroscopy.” *Physical Chemistry Chemical Physics*. **2015**, *17*, pp 27317-27327. **DOI:** 10.1039/C5CP03961D

B. Ashley, W. Salter, B. Stone, R. Nichols, and J. Owens. *Directed Energy Enhanced Coatings;* U.S. Air Force, Air Force Research Laboratories, Tyndall AFB, FL. AFRL-RX-TY-TR-2013-0025. **2015.**

J. Hunt, A. Ferrari, A. Lita, B. Ashley, and A. Stiegman "-Specific Effects on the Equilibrium Constants and Thermodynamics of the Steam-Carbon and Related Reactions" *J. Phys. Chem. C*, **2014**, *118* (18), pp 9346–9356. **DOI:** 10.1021/jp501206n

J. Hunt, A. Ferrari, A. Lita, M. Crosswhite, B. Ashley, and A. Stiegman. “-Specific Enhancement of the Carbon-Carbon Dioxide (Boudouard) Reaction.” *J. Chem. Phys. C*. **2013**, 117, 26871−26880. Featured in *Chemical and Engineering News* “Science and Technology Concentrates.” December 9, 2013. **DOI:** 10.1021/jp4076965

Presentations

B. Ashley, L. Derek, Y. Chiu, H. Gao, J. Owens, G.F. Strouse. "Specific effects in chemistry explored through reactor vessel design, theory, and spectroscopy." Oral Presentation at Southeast Regional Meeting of the American Chemical Society conference. Columbia, SC. Oct 23-26, 2016.

B. A. Ashley, W. B. Salter, K. M. Simpson, G. Strack, N. Pomerantz, W. Creasy, G.F. Strouse, J.R. Owens. "Mechanistic Study of Novel Schiff Base CWA Decomposition Catalysts." Poster Presentation at the Defense Threat Reduction Agency's Chemical and Biological Defense Science and Technology conference. St. Louis, MO. May 12-14, 2015.

B. A. Ashley, G. Strouse, J. Owens, "s and Materials Synthesis." Poster Presentation at the Materials Science Symposium. Florida State University, Tallahassee, FL. January 12, 2014. Awarded third place in poster competition.

B. A. Ashley, W.B. Salter, R. Nichols, J. Owens, "Development and Evaluation of Enhanced Coatings for Directed-Energy Decontamination." Poster Presentation at the Defense Threat Reduction Agency's Chemical and Biological Defense Science and Technology conference. Las Vegas, NV. November 14-18, 2011.

B. A. Ashley, W.B. Salter, R. Nichols, J. Owens, "Development and Evaluation of Enhanced Coatings for Directed-Energy Decontamination." Poster Presentation at the Defense Threat Reduction Agency's Chemical and Biological Defense Science and Technology conference. Orlando, FL. November 15-19, 2010.

R. Caufield, J. Roberts, J. Dahiya, A. Anand, B. Ashley, "Frequency Dependence of the Dielectric functionResponse of Select Materials at Frequencies." Poster Presentation at the Joint Meeting of the Texas Sections of the APS, AAPT, SPS. College Station, TX. October 18-20, 2007.

B.A. Johnson, I. Jung, H. Krawczynski "Simulation of Cadmium Zinc Telluride Detectors in C++." Presentation at the 14th National Ronald E. McNair Scholars Research Conference Delavan, WI. November 4-6, 2005.

Honors and Awards

- Phi Kappa Phi Member, 2016-present
- Research Fellowship, Oak Ridge Institute for Science and Education at Tyndall AFB, FL, 2010-present
- Teaching Fellowship, University of North Texas, 2007
- Graduate Fellowship for McNair Scholars, University of North Texas, 2006-2007
- Teaching Assistantship, University of North Texas, 2005-2008
- Sigma Pi Sigma Inductee, Southeast Missouri State University, 2005
- McNair Scholar, Southeast Missouri State University, 2004-2005
- American Legion Scholastic Excellence Award, Air Force ROTC Detachment 205, 2004

- American Legion Scholastic Excellence Award, Air Force ROTC Detachment 205, 2003
- President of Local Society of Physics Students Chapter, Southeast Missouri State University, 2002-2005
- Presidential Scholarship, Southeast Missouri State University, 2001-2002
- Bright Flight Scholarship, Southeast Missouri State University, 2001-2005

Professional Memberships

- American Chemical Society
- American Physical Society
- The American Ceramic Society